

Johannes Gutenberg-Universität Mainz

---

**Ophiolites in scope of geodynamic modeling and  
metamorphic processes**

---

Dissertation

zur Erlangung des Grades

**DOKTOR DER NATURWISSENSCHAFTEN**

im Promotionsfach Geologie/Paläonthologie

am Fachbereich Chemie, Pharmazie, Geographie und Geowissenschaften

der Johannes Gutenberg-Universität Mainz

von

**Iskander Ibragimov**

Geboren in Almetyevsk, Russland

JOHANNES GUTENBERG  
UNIVERSITÄT MAINZ



Mainz — 2024

- 
1. Berichtstatter: Prof. Dr. Evangelos Moulas
  2. Berichtstatter: Prof. Dr. Boris J. P. Kaus

Tag der mündlichen Prüfung:



# Abstract

This dissertation delves into the intricate processes surrounding the emplacement of ophiolites, rocks found at tectonic plate boundaries or in orogenic zones worldwide. The ophiolite sequence, composed of diverse lithologies such as sediments, mafic dykes, pillow lavas, crustal cumulates, and peridotites, presents a challenge in understanding the mechanisms of their obduction onto continental regions. The primary focus lies in addressing the complexities associated with obduction mechanics, the petrological and geodynamic processes involved, and unresolved issues like emplacement timescales, rates of obduction, and the structure of metamorphic soles. The dissertation adopts a comprehensive approach, integrating geological, geochemical, geophysical, and geochronological data. The investigation is centered on small oceanic basins, drawing insights from classic Tethyan ophiolite examples. Thermo-mechanical numerical models are employed, considering constraints from previous studies, to elucidate the dynamics of ophiolite emplacement. Chapter 2 explores the ophiolite emplacement process resulting from compressional movement during the closure of the Neotethys ocean. A 2-D numerical thermomechanical model reveals that small oceanic basins must be young and hot to overthrust onto continental margins, highlighting the significance of factors like convergence velocity and the asymmetric structure of the oceanic plate. In Chapter 3, a 1-D thermomechanical model investigates shear heating during ophiolite obduction, explaining the migration of the thermally-softened zone and the incorporation of metamorphosed crustal rocks into the ophiolitic complex. The model considers a strong crustal rheology and accounts for constraints like low convergence velocity, providing insights into the apparent metamorphic gradients observed in Oman ophiolites. Chapter 4 focuses on thermochronological calculations, considering erosion and variable convergence velocity. The results reveal the influence of dissipative heating and the resetting of isotopic clocks in rocks from deeper crustal levels, emphasizing the impact of grain size and rock type on age estimates.

In conclusion, this work successfully validates obduction mechanics, offering a comprehensive vision of the ophiolite emplacement process. The findings, while primarily validated for Tethyan-type ophiolites, contribute valuable insights into the broader understanding of ophiolite evolution, aligning closely with observations in nature.



# Kurzfassung

Diese Dissertation widmet sich den komplexen Prozessen rund um die Ablagerung von Ophioliten, Gesteinen, die weltweit an den Rändern tektonischer Platten oder in orogenen Zonen zu finden sind. Die Ophiolitsequenz, bestehend aus verschiedenen Gesteinstypen wie Sedimenten, mafischen Doleriten, Kissenlaven, krustalen Kumulaten und Peridotiten, stellt eine Herausforderung beim Verständnis der Mechanismen ihrer Übertragung auf kontinentale Regionen dar. Der Schwerpunkt liegt darauf, die mit den Obduktionsmechanismen verbundenen Komplexitäten, die petrologischen und geodynamischen Prozesse sowie ungelöste Fragen wie Ablagerungszeitskalen, Obduktionsraten und die Struktur metamorpher Sohlen zu adressieren. Die Dissertation verfolgt einen umfassenden Ansatz und integriert geologische, geochemische, geophysikalische und geochronologische Daten. Die Untersuchung konzentriert sich auf kleine ozeanische Becken und schöpft Erkenntnisse aus klassischen Beispielen von Tethyan-Ophioliten. Thermo-mechanische numerische Modelle werden unter Berücksichtigung von Einschränkungen aus früheren Studien eingesetzt, um die Dynamik der Ophioliten-Ablagerung zu klären. Kapitel 2 untersucht den Ablagerungsprozess von Ophioliten aufgrund von Kompressionsbewegungen während des Verschlusses des Neotethys-Ozeans. Ein 2-D numerisches Thermomechanikmodell zeigt, dass kleine ozeanische Becken jung und heiß sein müssen, um auf kontinentale Ränder überstülpen zu können, wobei die Bedeutung von Faktoren wie Konvergenzgeschwindigkeit und der asymmetrischen Struktur der ozeanischen Platte betont wird. In Kapitel 3 untersucht ein 1-D thermomechanisches Modell die Scherwärme während der Ophioliten-Obduktion und erklärt die Wanderung der thermisch erweichten Zone und die Einbeziehung metamorpher krustaler Gesteine in das Ophiolit-Komplex. Das Modell berücksichtigt eine starke Krustenrheologie und Einschränkungen wie niedrige Konvergenzgeschwindigkeit und liefert Einblicke in die scheinbaren metamorphen Gradienten, die in den Oman-Ophioliten beobachtet wurden. Kapitel 4 konzentriert sich auf thermochronologische Berechnungen unter Berücksichtigung von Erosion und variabler Konvergenzgeschwindigkeit. Die Ergebnisse zeigen den Einfluss dissipativer Erwärmung und das Zurücksetzen der isotopischen Uhren in Gesteinen aus tieferen krustalen Schichten und betonen die Auswirkungen von Korngröße und Gesteinstyp auf Altersschätzungen.

Abschließend validiert diese Arbeit erfolgreich die Mechanismen der Ophioliten-Ablagerung und bietet eine umfassende Vision des Prozesses. Die Erkenntnisse, obwohl hauptsächlich für Tethyan-Ophioliten validiert, tragen wertvolle Einblicke in das umfassendere

Verständnis der Ophioliten-Evolution bei und stimmen eng mit Beobachtungen in der Natur überein.

---

# Contents

<b>ABSTRACT</b> .....	<b>4</b>
<b>KURZFASSUNG</b> .....	<b>5</b>
<b>CONTENTS</b> .....	<b>7</b>
<b>LIST OF FIGURES</b> .....	<b>9</b>
<b>LIST OF TABLES</b> .....	<b>11</b>
<b>CHAPTER 1: INTRODUCTION</b> .....	<b>12</b>
1.1 SHORT HISTORICAL SUMMARY .....	13
1.2 STRUCTURE OF THE THESIS.....	14
1.3 REFERENCES.....	16
<b>CHAPTER 2: THE ROLE OF CONTINENTAL-MARGIN ARCHITECTURE ON MODELS OF OPHIOLITE EMPLACEMENT</b> .....	<b>19</b>
2.1 INTRODUCTION .....	19
2.2 METHODS .....	25
2.2.1 <i>Model setup</i> .....	25
2.2.2 <i>Systematic investigations</i> .....	32
2.3 RESULTS .....	34
2.3.1 <i>Reference model and influence of convergence velocity</i> .....	35
2.3.2 <i>Influence of initially asymmetric temperature distribution</i> .....	37
2.3.3 <i>Influence of weak-zone orientation and initial asymmetry</i> .....	39
2.3.4 <i>Influence of lower-crustal rheology</i> .....	40
2.3.5 <i>Influence of reducing velocity and erosion</i> .....	41
2.3.6 <i>The pressure and temperature (P-T) evolution of the crustal ophiolite rocks and their accretion to the overriding plate</i> .....	44
2.4 DISCUSSION .....	47
2.5 CONCLUSION .....	50
2.6 ACKNOWLEDGEMENTS .....	50
2.7 SUPPLEMENTARY.....	51
2.8 REFERENCES.....	54
<b>CHAPTER 3: A THERMO-MECHANICAL MODEL OF THE THERMAL EVOLUTION AND INCORPORATION OF THE METAMORPHIC SOLE IN THE OMAN OPHIOLITE</b> .....	<b>60</b>
3.1 INTRODUCTION .....	61
3.2 METHODS .....	63
3.3 RESULTS.....	67
3.3.1 <i>Temperature of the shear zone</i> .....	67

3.3.2	<i>Shear zone migration with time</i> .....	68
3.3.3	<i>Cooling-rate constraints</i> .....	69
3.3.4	<i>Systematic investigations</i> .....	70
3.4	DISCUSSION.....	72
3.5	CONCLUSIONS .....	73
3.6	ACKNOWLEDGEMENTS .....	74
3.7	REFERENCES.....	74
<b>CHAPTER 4: GEOCHRONOLOGICAL CONSTRAINTS FOR OPHIOLITE OBDUCTION .....</b>		<b>79</b>
4.1	INTRODUCTION.....	79
4.2	METHODS .....	81
4.3	RESULTS.....	83
4.4	DISCUSSION.....	88
4.5	ACKNOWLEDGEMENTS .....	90
4.6	REFERENCES.....	90
<b>CHAPTER 5: SUMMARY &amp; CONCLUSION .....</b>		<b>93</b>
5.1	SUMMARY .....	93
5.2	CONCLUSION .....	95
<b>EIDESSTATTLICHE ERKLÄRUNG.....</b>		<b>96</b>

# List of Figures

<b>FIGURE 1.1</b> OPHIOLITE DISTRIBUTION IN WORLD .....	12
<b>FIGURE 1.2</b> COMPARISON OF PSEUDOSTRATIGRAPHY OF A PENROSE-TYPE OPHIOLITE WITH VOURINOS AND PINDOS OPHIOLITES .....	13
<b>FIGURE 2.1</b> DISTRIBUTION OF OPHIOLITES ALONG THE DINARIDES, HELLENIDES AND OPHIOLITES IN ANATOLIDE-TAURIDE BLOCK. ....	24
<b>FIGURE 2.2</b> ISOCHEMICAL, PHASE-DIAGRAM SECTIONS USED FOR THE DENSITY CALCULATION. ....	28
<b>FIGURE 2.3</b> INITIAL MODEL CONFIGURATION OF THE REFERENCE MODEL (ONLY CENTRAL PART OF THE MODEL IS SHOWN). ....	31
<b>FIGURE 2.4</b> MODEL RESULTS SHOWING THE EVOLUTION OF DIFFERENT MODEL CONFIGURATIONS AS A FUNCTION OF CONVERGENCE VELOCITY. ....	35
<b>FIGURE 2.5</b> MODEL RESULTS SHOWING THE EVOLUTION OF DIFFERENT MODEL CONFIGURATIONS AS A FUNCTION OF THE INITIAL ASYMMETRY IN THE THICKNESS OF THE OCEANIC LITHOSPHERE AND AS A FUNCTION OF THE INITIAL LENGTH OF THE OCT. ....	37
<b>FIGURE 2.6</b> MODEL RESULTS SHOWING THE EVOLUTION OF DIFFERENT MODEL CONFIGURATIONS AS A FUNCTION OF THE INITIAL ASYMMETRY IN THE THICKNESS OF THE OCEANIC LITHOSPHERE AND AS A FUNCTION OF THE SHAPE OR PRESENCE OF THE CENTRAL WEAK ZONE .....	39
<b>FIGURE 2.7</b> AS IN FIGURE 2.5 BUT USING A “WET” LOWER-CRUSTAL RHEOLOGY. ....	41
<b>FIGURE 2.8</b> MODEL RESULTS SHOWING THE EFFECT OF SLOWING CONVERGING VELOCITY AND/OR CONSTANT EROSION RATE ON THE REFERENCE MODEL.....	42
<b>FIGURE 2.9</b> MODEL EVOLUTION AND POSITION OF P-T MARKERS AS A FUNCTION OF TIME. ....	44
<b>FIGURE 2.10</b> P-T PATHS OF MARKERS WITH RESPECT TO THE METAMORPHIC-FACIES BOUNDARIES. ....	46
<b>FIGURE S 1</b> REFERENCE MODEL CONFIGURATION AT CA 5MYRS.....	51
<b>FIGURE S 2</b> FIGURE THAT SHOWS THE INFLUENCE OF THE INITIAL OCEANIC-CRUST/CONTINENTAL-CRUST CONTACT ON THE MODEL RESULTS.....	52
<b>FIGURE S 3</b> NON-CONSTANT CONVERGING VELOCITY USED TO CALCULATE FIGURE 2.8 OF THE MAIN TEXT.....	52
<b>FIGURE S 4</b> FIGURE THAT SHOWS THE INFLUENCE OF VARIABLE EROSION RATES IN THE REFERENCE MODEL CONFIGURATION.....	53
<b>FIGURE S 5</b> DISTRIBUTION OF PLASTIC FINITE STRAIN IN THE REFERENCE MODEL.....	54
<b>FIGURE 3.1</b> SIMPLIFIED MAP SHOWING THE DISTRIBUTION OF OPHIOLITES IN THE MEDITERRANEAN REGION. THE OMAN OPHIOLITE IS SHOWN IN THE LOWER, RIGHT PART OF THE MAP.....	61
<b>FIGURE 3.2</b> THERMOMECHANICAL MODEL CONFIGURATION. ....	64
<b>FIGURE 3.3</b> TEMPERATURE EVOLUTION AND STRAIN RATE DISTRIBUTION WITH TIME.....	68
<b>FIGURE 3.4</b> FINITE SHEAR STRAIN EVOLUTION AS A FUNCTION OF TIME AFTER THE SHEARING INITIATION.....	69
<b>FIGURE 3.5</b> DEPTH OF THE ACTIVE SHEAR ZONE WITH TIME.....	70
<b>FIGURE 3.6</b> MAXIMUM TEMPERATURE AT THE VICINITY OF THE LITHOLOGICAL BOUNDARY ( $\pm 10$ M) AS A FUNCTION OF THE AGE OF THE OCEAN (IN MYR) AND OF THE SHEARING VELOCITY (IN CM/YR).....	71
<b>FIGURE 4.1</b> DETAIL OF THE INITIAL CONFIGURATION OF GEODYNAMIC MODEL USED IN THIS STUDY. ....	81
<b>FIGURE 4.2</b> DETAIL OF THE FINAL CONFIGURATION OF GEODYNAMIC MODEL USED IN THIS STUDY. ....	82

<b>FIGURE 4.3</b> PLASTIC DEFORMATION FOR THE REGION SHOWN IN FIGURE 4.2. THE INLET SHOWS THE DISTRIBUTION OF THE APPARENT AGES AT THE SURFACE OF THE MODEL.....	84
<b>FIGURE 4.4</b> APPARENT AGES OF MARKERS THAT REACHED THE SURFACE IN OUR GEODYNAMIC MODEL .....	85
<b>FIGURE 4.5</b> P-T EVOLUTION OF SELECTED MARKERS THAT REACHED THE SURFACE. THE DIFFERENT COLOURS INDICATE THE EXTEND OF THE DIFFERENT METAMORPHIC FACIES .....	86
<b>FIGURE 4.6</b> APPARENT AGE DISTRIBUTION FOR THE SURFACE MARKERS ASSUMING DIFFERENT GRAINSIZES AND DIFFERENT MINERALS.....	87
<b>FIGURE 4.7</b> TRAJECTORIES FOR SELECTED EXHUMED MARKERS.. .....	88

# List of Tables

<b>TABLE 2.1</b> SYMBOLS AND UNITS OF QUANTITIES USED IN THIS STUDY .....	25
<b>TABLE 2.2</b> DESCRIPTION OF MATERIAL PARAMETERS USED IN MODEL CONFIGURATION .....	29
<b>TABLE 2.3</b> DISLOCATION CREEP PARAMETERS USED IN LAMEM.....	32
<b>TABLE 2.4</b> DIFFUSION CREEP PARAMETERS USED IN LAMEM.....	33
<b>TABLE 2.5</b> RANGE OF VALUES USED IN MODEL CONFIGURATION.....	33
<b>TABLE 3.1</b> SYMBOLS AND UNITS OF QUANTITIES USED IN THIS STUDY.. .....	63

# Chapter 1

## Introduction

Ophiolites are the rocks found all over the world in the zones of orogeny or tectonic plate boundaries (Figure 1.1). The ophiolite sequence typically comprises sediments, mafic dykes and pillow lavas, crustal cumulates, and peridotites (Anonymous 1972a) (Figure 1.2). The ophiolite complex is typically underlain by metamorphosed crustal sediments, commonly known as metamorphic soles. With the exception of the metamorphic sole, the various lithologies encountered in ophiolite complexes is similar to rocks currently found in situ within oceanic plates. Thus, it is currently a challenge in geodynamics to understand the mechanism of emplacement or “obduction” (Dewey 1976) of such rocks atop continental regions.

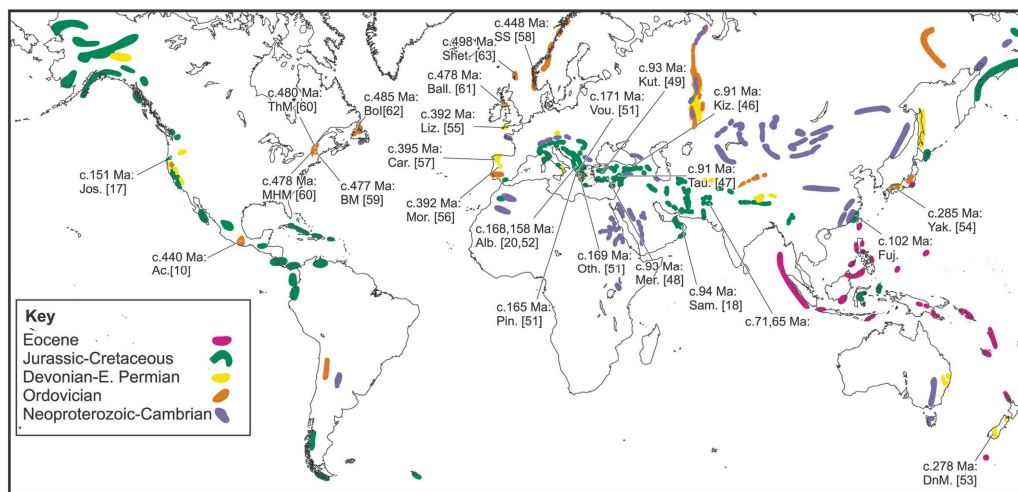


Figure 1.1 Ophiolite distribution in world (from Vaughan and Scarrow 2003)

When oceanic lithosphere converges towards continental regions, it is expected that the dense oceanic plate will subduct (Cloos 1993a) and this will lead to a development of a subduction zone similar to what is observed now in the Andes. It is therefore expected that the oceanic plate sinks down within the mantle and disappears (Dewey 1976). This is the normal life cycle of oceanic plates, so it is impossible to find oceanic crust in place that is older than 200 million years (Abbott and Lyle 1984; Crameri *et al.* 2019). However, in the case of ophiolites, complex geodynamic processes have led to the emplacement of part of the oceanic lithosphere on top of continental regions. Therefore, fragments of an oceanic plate that are over 200 million years old can now be found on mountain chains (Figure 1.1). These rocks have



been studied for over 100 years, yet the processes that lead to their obduction is still not fully understood.

## 1.1 Short historical summary

Ophiolites are geological formations that hold significant importance in the field of Earth sciences. Ophiolites were first recognised more than 200 years ago (Brongniart 1813). However, the systematic study of ophiolites gained momentum only in the middle of 20<sup>th</sup> century. Studies of that time made a significant contribution to the understanding of plate tectonics and the role of ophiolites in the Earth's crust (Benson 1926; Steinmann 1927; Hess 1965; Gass 1968; Coleman 1971; Moores and Vine 1971). The Deep-Sea Drilling project, started in the late 1960's, allowed a direct comparison with oceanic rocks, which validated the interpretations from ophiolite studies (Adamson 1984). The plate tectonics revolution spawned a various suggestion on ophiolite emplacement process (Dewey 1976). Modern technological and scientific advancements, including better analytical and numerical techniques, satellite imagery and more detailed field investigations and laboratory analyses allowed to refine and confirm prior suggestions (Michard *et al.* 1984; Chemenda *et al.* 1996; Hacker *et al.* 1996; Shervais 2001; Pomonis *et al.* 2002a; Wakabayashi and Dilek 2003a; Garfunkel 2006a; Rassios

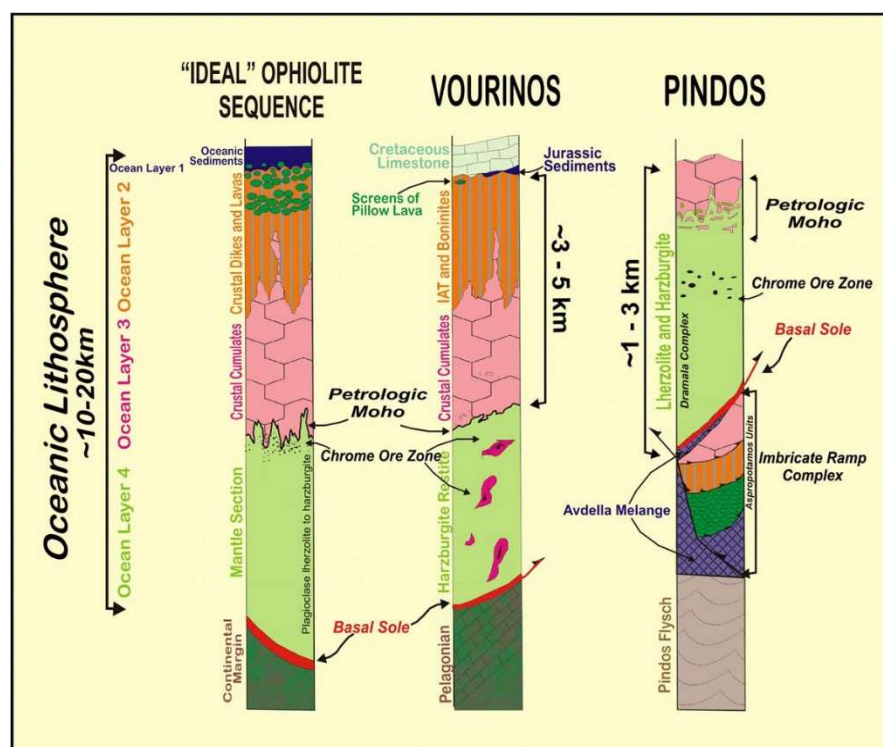


Figure 1.2 Comparison of pseudostratigraphy of a Penrose-type ophiolite with Vourinos and Pindos ophiolites (Rassios and Dilek, 2009)

and Moores 2006; Elitok and Drüppel 2008; Duretz *et al.* 2016a; Parlak *et al.* 2019; Burg and Moulas 2022).

However, ophiolite emplacement process still poses several challenges, many of them related with the obduction mechanics and the petrological/geodynamic processes that are associated with them. Ongoing research still aims to understand all the details and the intricacies of the aforementioned processes. Known remaining issues include the emplacement timescales and the rate of obduction, the mechanism of emplacement onto the continental crust, the structure of metamorphic sole and its geochemical signatures, the cooling rates of the metamorphic sole and the influence of shear heating in the basal high strain zones.

This dissertation is an effort to integrate geological, geochemical, geophysical and geochronological data on the ophiolite obduction process of small basins. The focus on small basins stems from the classic examples from Tethyan ophiolites (Moores 1982) that can be used as case studies of the aforementioned processes. This is done by employing thermo-mechanical numerical models and also conduct systematic investigation on most important parameters on dynamics of ophiolite emplacement. Moreover, the models presented in this thesis take into account constrains that were obtained from available findings of previous studies of ophiolites. As a result, we obtain key features of ophiolite obduction and define the processes that might have participated in forming of Tethyan ophiolites.

## 1.2 Structure of the thesis

The thesis comprises three main chapters that aim to explore the nature of ophiolite emplacement using numerical methods, including modelling and thermal age (thermochronology) calculations. To this end, the 3-D code LaMEM (Kaus *et al.* 2016) , developed by the geophysics group in Mainz, was used. Chapter two shows a systematic study that was performed in order to identify the key geometric (and kinematic) parameters needed for the successful obduction of oceanic crust under continuous compression. Chapter three utilises the 1-D shear heating model, which was developed by the candidate in collaboration with Dr. Daniel Kiss and Prof. Evangelos Moulas. This 1-D model offers a high-resolution investigation of the temperature evolution and the cooling rates experienced by metamorphic-sole rocks. Chapter four uses the previously calculated examples from Chapter two and evaluates the apparent ages of common metamorphic minerals. This was done by linking the results of LaMEM to KADMOS software. KADMOS was developed by Prof. Evangelos Moulas and Prof. Mark Brandon (Moulas and Brandon 2022).

---

**Chapter 2: The role of continental-margin architecture on models of ophiolite emplacement.**

In this chapter we study ophiolite obduction scenarios, which were first described in (Dewey 1976). For that, we used the 3-D thermomechanical code LaMEM and prepared an initial configuration that includes a small ocean basin surrounded by two continents (in 2-D). The spreading process was not included since it was not in scope of this study and also it was extensively explored by recent work of Candiotti *et al.* (2021). We impose the convergence of the two model continents by prescribing inflow from the boundary and try to find the most optimal initial geometrical and thermal structure for successful ophiolite obduction. We performed systematic investigations, consisting of the change of 7 parameters and producing more than 140 models.

**Chapter 3: A thermo-mechanical model of the thermal evolution and incorporation of the metamorphic sole in the Oman ophiolite.**

This chapter examines the thermal evolution of metamorphic soles in ophiolites. The section investigates shear heating as a mechanism that can cause the high temperatures and rapid cooling rates observed in metamorphic soles. Our model considers a 1-D section of a system of two oceanic crusts where the upper plate is thrust over the lower plate. We obtain the thermal evolution of the self-induced and self-sustaining shear zone by imposing a kinematic boundary conditions. After a prescribed time of deformation, the imposed boundary condition is lifted and the thermal history is recorded. The thermal histories obtained were further compared with results obtained from Oman ophiolites. Additionally, our model explains the incorporation of the metamorphic sole rocks from the lower plate as a result of the progressive thermal softening of the lower plate.

**Chapter 4: Geochronological constraints of ophiolites.**

Chapter four utilised data generated by numerical model in chapter two to calculate apparent K-Ar ages of rocks which are found at the surface at the end of the simulation. The findings reveal a pattern where rocks with much younger apparent ages are observed in zones associated with shear zones that can be traced from the numerical model. A systematic investigation was conducted to study the sensitivity of apparent isotopic age calculation, using various grain sizes and different minerals.

## 1.3 References

- Abbott, D. and Lyle, M. 1984. Age of oceanic plates at subduction and volatile recycling. *Geophysical Research Letters*, **11**, 951–954.
- Adamson, A.C. 1984. *Basement Lithostratigraphy, Deep Sea Drilling Project Hole 504B*. 3DSDP Initial Reports.
- Anonymous. 1972. Penrose field conference on ophiolites. *Geotimes*, **17**, 24–25.
- Benson, W. 1926. The tectonic conditions accompanying the intrusion of basic and ultrabasic igneous rocks. *Natl. Acad. Sci. U.S.A.*, 1–90.
- Brongniart, A. 1813. Essai d'une classification minéralogique des roches mélangées.-J. des Mines. **XXXIV**, 199.
- Burg, J.-P. and Moulas, E. 2022. Cooling-rate constraints from metapelites across two inverted metamorphic sequences of the Alpine-Himalayan belt; evidence for viscous heating. *Journal of Structural Geology*, **156**, 104536, <https://doi.org/10.1016/j.jsg.2022.104536>.
- Candioti, L.G., Duretz, T., Moulas, E. and Schmalholz, S.M. 2021. Buoyancy versus shear forces in building orogenic wedges. *Solid Earth*, **12**, 1749–1775, <https://doi.org/10.5194/se-12-1749-2021>.
- Chemenda, A.I., Mattauer, M. and Bokun, A.N. 1996. Continental subduction and a mechanism for exhumation of high-pressure metamorphic rocks: new modelling and field data from Oman. *Earth and Planetary Science Letters*, **143**, 173–182, [https://doi.org/10.1016/0012-821X\(96\)00123-9](https://doi.org/10.1016/0012-821X(96)00123-9).
- Cloos, M. 1993. *Lithospheric Buoyancy and Collisional Orogenesis: Subduction of Oceanic Plateaus, Continental Margins, Island Arcs, Spreading Ridges, and Seamounts*.
- Coleman, R.G. 1971. Plate tectonic emplacement of upper mantle peridotites along continental edges. *Journal of Geophysical Research*, **76**, 1212–1222, <https://doi.org/10.1029/JB076i005p01212>.
- Crameri, F., Conrad, C.P., Montési, L. and Lithgow-Bertelloni, C.R. 2019. The dynamic life of an oceanic plate. *Tectonophysics*, **760**, 107–135, <https://doi.org/10.1016/j.tecto.2018.03.016>.
- Dewey, J.F. 1976. Ophiolite obduction. *Tectonophysics*, **31**, 93–120, [https://doi.org/10.1016/0040-1951\(76\)90169-4](https://doi.org/10.1016/0040-1951(76)90169-4).
- Duretz, T., Agard, P., Yamato, P., Ducassou, C., Burov, E.B. and Gerya, T.V. 2016. Thermo-mechanical modeling of the obduction process based on the Oman Ophiolite case. *Gondwana Research*, **32**, 1–10, <https://doi.org/10.1016/j.gr.2015.02.002>.
- Elitok, Ö. and Drüppel, K. 2008. Geochemistry and tectonic significance of metamorphic sole rocks beneath the Beyşehir–Hoyran ophiolite (SW-Turkey). *Lithos*, **100**, 322–353, <https://doi.org/10.1016/j.lithos.2007.06.022>.
- Garfunkel, Z. 2006. Neotethyan ophiolites: Formation and obduction within the life cycle of the host basins. *Geological Society Special Publication*, **260**, 301–326, <https://doi.org/10.1144/GSL.SP.2006.260.01.13>.

- Gass, I.G. 1968. Is the Troodos Massif of Cyprus a Fragment of Mesozoic Ocean Floor? *Nature*, **220**, 39–42, <https://doi.org/10.1038/220039a0>.
- Hacker, B.R., Mosenfelder, J.L. and Gnos, E. 1996. Rapid emplacement of the Oman ophiolite: Thermal and geochronologic constraints. *Tectonics*, **15**, 1230–1247, <https://doi.org/10.1029/96TC01973>.
- Hess, H. H. 1965. Mid-oceanic ridges and tectonics of the sea floor, in *Submarine Geology and Geophysics. Proceedings of the Seventeenth Symposium of the Colston Research Society*, 317–334.
- Kaus, B.J.P., Popov, A.A., Baumann, T.S., Pusok, A.E., Bauville, A., Fernandez, N. and Collignon, M. 2016. Forward and Inverse Modelling of Lithospheric Deformation on Geological Timescales. *NIC Series*, **48**, 978–3.
- Michard, A., Bouchez, J.L. and Ouazzani-Touhami, M. 1984. Obduction-related planar and linear fabrics in Oman. *Journal of Structural Geology*, **6**, 39–49, [https://doi.org/10.1016/0191-8141\(84\)90082-8](https://doi.org/10.1016/0191-8141(84)90082-8).
- Moores, E.M. 1982. Origin and emplacement of ophiolites. *Reviews of Geophysics*, **20**, 735–760, <https://doi.org/10.1029/RG020i004p00735>.
- Moores, E.M. and Vine, F.J. 1971. The Troodos Massif, Cyprus and other ophiolites as oceanic crust: evaluation and implications. *Philosophical Transactions of the Royal Society of London. Series A, Mathematical and Physical Sciences*, **268**, 443–467, <https://doi.org/10.1098/rsta.1971.0006>.
- Moulas, E. and Brandon, M.T. 2022. KADMOS: a Finite Element code for the calculation of apparent K-Ar ages in minerals.
- Parlak, O., Dunkl, I., et al. 2019. Rapid cooling history of a Neotethyan ophiolite: Evidence for contemporaneous subduction initiation and metamorphic sole formation. *GSA Bulletin*, **131**, 2011–2038, <https://doi.org/10.1130/B35040.1>.
- Pomonis, P., Tsikouras, B. and Hatzipanagiotou, K. 2002. Origin, evolution and radiometric dating of subophiolitic metamorphic rocks from the Koziakas ophiolite (W. Thessaly, Greece). *Neues Jahrbuch für Mineralogie - Abhandlungen*, **177**, 255–276, <https://doi.org/10.1127/0077-7757/2002/0177-0255>.
- Rassios, A.H.E. and Moores, E.M. 2006. Heterogeneous mantle complex, crustal processes, and obduction kinematics in a unified Pindos-Vourinos ophiolitic slab (northern Greece). *Geological Society, London, Special Publications*, **260**, 237–266, <https://doi.org/10.1144/GSL.SP.2006.260.01.11>.
- Shervais, J.W. 2001. Birth, death, and resurrection: The life cycle of suprasubduction zone ophiolites: SUPRASUBDUCTION ZONE OPHIOLITES. *Geochemistry, Geophysics, Geosystems*, **2**, n/a-n/a, <https://doi.org/10.1029/2000GC000080>.
- Steinmann, G. 1927. Die ophiolitischen Zonen in der mediterranean Kettingebirgen. *Int. Geol. Congr. 14th*, 638–667.
- Wakabayashi, J. and Dilek, Y. 2003. What constitutes ‘emplacement’ of an ophiolite?: Mechanisms and relationship to subduction initiation and formation of metamorphic soles.

*Geological Society, London, Special Publications*, **218**, 427–447,  
<https://doi.org/10.1144/GSL.SP.2003.218.01.22>.

---

## Chapter 2

# The role of continental-margin architecture on models of ophiolite emplacement

**This chapter has been published in:**

Ibragimov, Iskander; Moulas, Evangelos (2024). The role of continental-margin architecture on models of ophiolite emplacement. Geological Society of London. Collection. <https://doi.org/10.1144/jgs2023-063>

## **Abstract**

Ophiolite obduction, the process by which part of the oceanic crust overlaps the continental margin, is challenging when it comes to the geodynamic reconstruction of lithospheric processes. This buoyancy difference between dense oceanic crust and the relatively buoyant continental crust makes the obduction of the oceanic crust difficult, if not impossible, when only buoyancy forces are considered. To overcome the difficulties posed by the negative buoyancy, the initial configuration of the oceanic basins must have specific thermal and geometric constraints. Here we present a systematic investigation of the geometrical and the geodynamical parameters which control the ophiolite emplacement process. Our study reveals which parameters are the most important during ophiolite emplacement and which are the most optimal geometries that favour ophiolite emplacement. We focus on “Tethyan” ophiolites which are characterized by relatively small inferred basin size and are commonly found in Mediterranean region. Based on a combination of various parameters, we identified the most susceptible configurations for ophiolite obduction. Our models demonstrate, in agreement to geological data, that the obducted lithosphere must be young and the length of the Ocean-Continent-Transition zone must be relatively sharp in order to achieve ophiolite obduction.

## 2.1 Introduction

Ophiolites are rock suites which are considered to be the remnants of oceanic lithosphere and now are found emplaced atop continental regions (Coleman 1971; Dewey 1976). In spite

of their limited exposure compared to the surrounding continental rocks, ophiolites can provide crucial information on the involvement of oceanic lithosphere during orogeny (Moores 1982). For this reason, ophiolites have been intensively studied for more than a century and the processes leading to their formation and emplacement are often debated (Brongniart 1813; Suess 1909; Gass 1968; Coleman 1971; Moores and Vine 1971; Moores 1982; Garfunkel 2006). The fact that ophiolites are composed of mostly mafic and ultramafic lithologies makes the geodynamic models for their emplacement (or obduction) problematic. This is because mafic and ultramafic rocks are generally too dense and thus, buoyancy forces are not sufficient to explain their emplacement on the continental crust. Over the years, various researchers referred to obduction as either the process of subduction initiation beneath an ophiolite, or as the subaerial exposure of the ophiolite (see Wakabayashi and Dilek 2003; for discussion). In their work, the latter authors have emphasized that previous emplacement definitions have been developed mainly for the Tethyan ophiolites. In this work, we will refer to obduction or emplacement as the process(es) leading to the thrusting of ophiolitic rocks atop continental margins following the original definition of Dewey (1976).

The problem of ophiolite emplacement has been previously considered in various studies. The earliest studies focus on geological observations and kinematic descriptions of the rock masses involved (Dewey 1976; Moores 1982). The focus on kinematic aspects of ophiolite emplacement led authors to suggest geodynamic models that were not always in agreement with each other. In the words of Moores, (1982): “However unchanged the geology of various occurrences has remained, the geologists' observations and interpretations have varied over the years according to the current paradigm”. At this point we would like to note that in some cases, the ophiolite suites are not fully exposed and their structure at depth can only be assessed only by using geophysical methods (e.g. Rassios and Dilek 2009). Thus, the discrepancies of the available geodynamic interpretations are not likely to originate from the variability of geologic data, but it seems to be a consequence of the lack of geodynamic constraints on the thermo-mechanical processes involved. Thus, geodynamic constraints are needed to solve the remaining issues related to the problems of ophiolite obduction. To this aim, more recent studies have utilized mechanical and thermo-mechanical models of lithosphere deformation and have successfully presented cases where the oceanic rocks can be emplaced on the continental margins (Chemenda et al. 1996; Edwards et al. 2015; Duretz et al. 2016; Hässig et al. 2016a; Porkoláb et al. 2020).

In the early models of Chemenda et al. (1996) the authors presented analogue, mechanical model results that showed that the uplift of previously-subducted continental rocks can separate



the overlying oceanic lithosphere. This process leads to a geodynamic scenario where only a part of the oceanic lithosphere is finally found to be obducted on the continental interior. More recently, Edwards et al. (2015) have demonstrated the feasibility of continental-crust subduction, that eventually leads to the emplacement of dense, oceanic lithosphere on the continental margin. All previous models are in essence three-dimensional (3D; not considering time evolution) but they simulate plane-strain conditions. Despite the first-order agreement with the natural analogues (e.g. Oman ophiolite), the previous models do not consider the effects of a temperature-dependent, visco-elasto-plastic rheology, heat diffusion and the associated density changes. Therefore, numerical models are needed to investigate this process further.

The obduction processes has been modelled numerically by various authors. Numerical studies use constitutive equations together with the conservation of mass momentum and energy equations to build a self-consistent system of equations. This system that can be used to solve the geodynamic evolution of various geodynamic scenarios given the appropriate initial and boundary conditions. With respect to the ophiolite obduction problem, up to now, all published studies concern two-dimensional (2D) models with kinematic (velocity) boundary conditions. Being two 2D approximations of reality, such models simulate the evolution of a particular section preferably perpendicular to the subduction/obduction thrust contact (e.g. Duretz et al. 2016; Porkoláb et al. 2021). In such cases, having kinematic boundary conditions allows the consideration of scenarios where the driving forces are not limited to the slab-pull of the 2D-model domain but are related to boundary tractions that originate from the complex, 3D deformation of the lithosphere. In fact, numerical studies considering 2D, plane-strain models have shown that the slab-pull force (in 2D) is not sufficient to create the necessary forces needed for subduction initialization (Bessat et al. 2020). Therefore, the consideration of boundary velocities is needed to further understand the dynamics of obduction in 2D.

Duretz et al., (2016) modeled a two-stage process of the subduction and exhumation of ophiolites having the Oman ophiolite as a case study. They showed that obduction can be achieved during bulk shortening of 350-400 km within 10 myr. As “bulk shortening” we refer to the shortening imposed by far-field converging velocity boundary conditions. Duretz et al., (2016) state that the key ingredients for a stable obduction are the initial lithospheric structure, and the switch from a compressional to an extensional stage. Again, this switch refers to the far-field boundary conditions and not to local extension that may be observed in the obduction zone. The switch from far-field compression to extension is apparently needed to explain the exhumation of the metamorphic-sole rocks as well as the high-pressure lithologies that are found in the continental margin associated with ophiolite obduction (El-Shazly and Coleman

1990). Finally, the previous authors suggested that the presence of a thermal anomaly within the oceanic plate is necessary for the explanation of the high temperature experienced by the metamorphic-sole rocks.

The importance of the anomalous thermal structure was also investigated by (Hässig et al. (2016b) and their study had similar conclusions on its importance for ophiolite obduction. Furthermore, the transition from a far-field compressional to an extensional stage was investigated in detail by Hässig et al. (2016a, b) with a focus on the North-East Anatolia – Lesser Caucasus ophiolites. Their models show the importance of the thickness of oceanic lithosphere and applied boundary velocities. Their results show that, where the continental regions have a deeper (150 km) Lithosphere-Asthenosphere Boundary (LAB) and a relatively sharp Ocean-Continent Transition (OCT), the ophiolite rocks were able to be emplaced on the continental margin even without the use of a previously-defined weak zone (Hässig et al., 2016). Slower velocities (<5 cm/yr) in the extension stage following compression led to the formation of deeper foreland flexural basins and larger amounts of ophiolitic material on top of the continental margin (Hässig et al. 2016a, b).

By building up on previous knowledge on the conditions needed to explain the high-pressure metamorphism at the subducting continental margin, Porkoláb et al. (2020) presented continental subduction models under continuous convergence but with variable convergence velocity. During the convergence stage, the subducted part of the upper continental crust reaches eclogite-facies conditions and starts to decouple from the subducting plate. Their results showed that the decoupled part uplifts due to buoyancy forces, and the overthrust oceanic plate locally extends as a result of the forces that are exerted to it from uplifting crustal part. This extension leads to the separation of a part from oceanic lithosphere from its main body. In the same work, Porkoláb et al., (2020) demonstrated that shear heating, i.e. the work dissipated as heat during irreversible deformation, and the relatively strong lower-crustal lithologies are necessary in order to achieve the extrusion of the upper crust. This extrusion results to the local extension oceanic plate and the final ophiolite emplacement (Porkoláb et al. 2020).

What is clear in all previous modelling studies, is the fact that they have focused in case studies where the exhumation of subducted continental crust (with or without the assistance of far-field extension) is responsible for the final emplacement of the ophiolite rocks on the subducting continental margin. However, given the significant thermal anomalies (e.g. Duretz et al. 2016; Hässig et al. 2016b) and the associated density changes that are required to explain continental subduction, a systematic investigation of the initial thermal structure of the subducting continental margin is needed to gain further insights in the thermo-mechanical

processes involved. The investigation of the thermal structure is crucial also for another reason, that is, the accurate calculation of buoyancy forces. What is clear in lithospheric dynamics studies is that the densification from metamorphic reactions and pressure-temperature (P-T) changes need to be considered in order to have realistic buoyancy forces (Candioti et al. 2021).

In this work, we investigate the thermo-mechanical conditions and the geodynamic settings of ophiolite emplacement. We focus on the closure of relatively small (<200 km) oceanic basins under continuous compression in agreement with paleogeographic reconstructions used for Neotethyan ophiolites (Figure 2.1; e.g. Stampfli and Borel 2002; Garfunkel 2006; Dilek and Furnes 2011; Robertson 2012). The focus on relatively small oceanic basins is motivated by the fact that the Neo-Tethyan oceanic basins were very small in the western margins of Tethys (c.f. Stampfli and Borel 2002). Given that recent data compilations from geophysical studies show high variability on the structure of the OCT zones (e.g. Biari et al. 2021), we do not employ a particular geometrical configuration with respect to the initial thermal structure of the OCT but we rather calculate different thermo-mechanical models depending on various initial architectures. The initial temperature distribution is important since the lithosphere/asthenosphere boundary is primarily a thermal boundary where the temperature-dependent viscosity changes drastically. The temperature-dependence of viscosity requires that the lithosphere boundaries evolve in a dynamic manner and therefore the obduction problem is inherently of thermo-mechanical nature. Our approach is general and allows the investigation of different initial geometries that can have different initial temperature distributions. This allows us to examine various scenarios that could have been realized in the geological past. We particularly favor this approach since ophiolite obduction appears to be not a common process (compared to oceanic subduction), and has been regarded as an “accident” compared to the well-established subduction process (Agard et al. 2023). This “accidental” occurrence of obducted ophiolites may be the result of rather uncommon initial thermo-mechanical conditions of the converging margins.

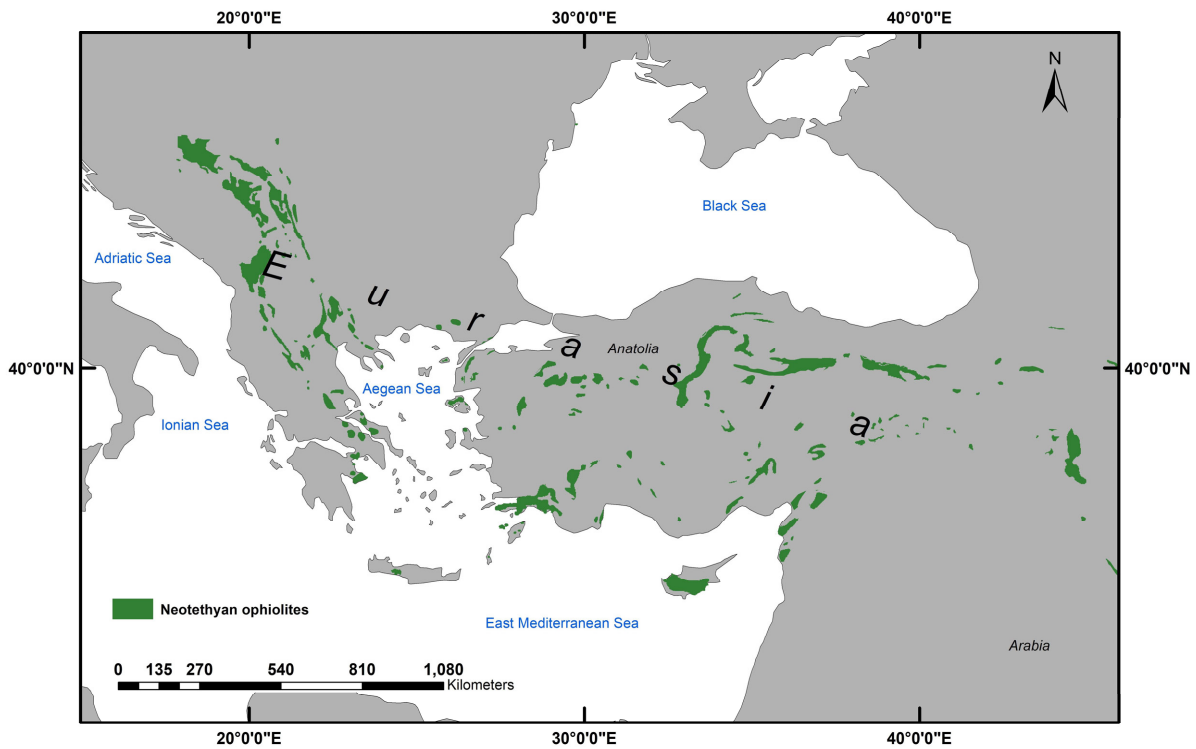


*Figure 2.1 Distribution of ophiolites along the Dinarides, Hellenides and ophiolites in Anatolide-Tauride block. Modified after Maffione and van Hinsbergen (2018; and references therein)*

Our investigation is motivated from the data coming from the ophiolites outcropping in the Balkan peninsula (e.g. Pindos, Mirdita). These ophiolite bodies are thought to be obducted within a couple of million years from their time of formation in Middle-Late Jurassic times (Dilek et al. 2008; Ghikas et al. 2010). Our working hypothesis for continuous compression is also supported by the lack of exhumed high-pressure rocks associated with the ophiolite emplacement of these ophiolites. We investigate the necessary conditions for obduction by using thermo-mechanical models of lithosphere deformation. In addition, we consider phase equilibria for the accurate calculation of densities of the lithologies involved. The accurate calculation of densities allows us to resolve the buoyancy forces in an improved manner compared to analogue models or numerical models that use constant material density. Furthermore, we report the results of systematic investigations on the architecture of the converging continental margins. In some cases, our models predict the obduction of a part of the oceanic lithosphere on the continental margin in agreement with geological interpretations under continuous convergence. Our results are consistent with geologic interpretations which require that the ophiolite obduction occurred just after the initiation of an intra-oceanic subduction (e.g. Wakabayashi and Dilek 2003). In addition, we present the results of the systematic investigation of geometric parameters and highlight the necessary conditions for

ophiolite obduction. Our results show that the obduction of part of the oceanic crust is possible during the formation of a suture zone during continental convergence and early collision.

## 2.2 Methods

### 2.2.1 Model setup

We employ LaMEM (Kaus *et al.* 2016), a finite-difference code that is able to simulate the thermo-mechanical behaviour of rocks with visco-elasto-plastic rheology. LaMEM is used to solve the following coupled system of Partial Differential Equations (PDEs) for momentum, mass and energy conservation. The equations that are solved are:

$$\frac{\partial \tau_{ij}}{\partial x_i} - \frac{\partial P}{\partial x_j} + \rho g_j = 0 \quad (2.1)$$

$$\frac{\partial v_i}{\partial x_i} = 0 \quad (2.2)$$

$$\rho C_p \frac{DT}{Dt} = \frac{\partial}{\partial x_i} \left( \lambda \frac{\partial T}{\partial x_i} \right) + H \quad (2.3)$$

where repeated indices imply summation (Einstein notation), Eq. (2.1) is the conservation of linear momentum in the  $j^{\text{th}}$  direction and at the limit where inertial forces are negligible (Stokes' limit), Eq. (2.2) is the equation for mass conservation (continuity equation) at the incompressible limit, and Eq. (2.3) is the equation for the conservation of energy expressed as a function of temperature (also called “temperature equation”). The temperature equation includes a source term ( $H$ ) that is related to the dissipated heat during irreversible, non-elastic deformation. The effects of adiabatic heating are ignored in the calculation of temperature. More details on the definition of symbols can be found in Table 2.1.

*Table 2.1 Symbols and units of quantities used in this study*

Parameter	Symbol	Units
Temperature	T	°C
Deviator of Cauchy stress tensor	$\tau_{ij}$	Pa
Velocity	v	$\text{m s}^{-1}$
Coordinates	x	m
Pressure (negative mean stress)	P	Pa
Density	$\rho$	$\text{kg m}^{-3}$
Gravity acceleration vector	$g_i$	$\text{m s}^{-2}$
Bulk modulus	K	Pa

<b>Thermal expansion coefficient</b>	$\alpha$	$\text{K}^{-1}$
<b>Specific heat</b>	$C_p$	$\text{J kg}^{-1} \text{K}^{-1}$
<b>Thermal conductivity</b>	$\lambda$	$\text{J m}^{-1} \text{s}^{-1} \text{K}^{-1}$
<b>Volumetric rate of heat production</b>	$H$	$\text{J m}^{-3} \text{s}^{-1}$
<b>Material (Lagrangian) time derivative</b>	$D/Dt$	$\text{s}^{-1}$
<b>Loading geometry coefficient</b>	$F$	–
<b>Material constant (used in viscous flow law)</b>	$A_D$	$\text{Pa}^{-n} \text{m}^{-m} \text{s}^{-1}$
<b>Stress exponent (used in viscous flow law)</b>	$n$	–
<b>Grain size (average diameter)</b>	$h$	$\text{m}$
<b>Grain size exponent (used in viscous flow law)</b>	$m$	–
<b>Square root of the second invariant of the strain rate tensor</b>	$\dot{\epsilon}_{II}$	$\text{s}^{-1}$
<b>Square root of the second invariant of the stress tensor</b>	$\tau_{II}$	$\text{Pa}$
<b>Components of the total strain rate tensor</b>	$\dot{\epsilon}_{ij}$	$\text{s}^{-1}$
<b>Components of the total stress tensor</b>	$\tau_{ij}$	$\text{Pa}$
<b>Effective viscosity</b>	$\eta_{\text{eff}}$	$\text{Pa s}$
<b>Activation energy (used in viscous flow law)</b>	$E_a$	$\text{J mol}^{-1}$
<b>Activation volume (used in viscous flow law)</b>	$V_a$	$\text{J Pa}^{-1}$
<b>H<sub>2</sub>O fugacity (used in viscous flow law)</b>	$f_{\text{H}_2\text{O}}$	$\text{Pa}$
<b>H<sub>2</sub>O fugacity exponent (used in viscous flow law)</b>	$r$	–
<b>Absolute Temperature (used in viscous flow law)</b>	$T_K$	$\text{K}$
<b>Cohesion</b>	$c$	$\text{Pa}$
<b>Friction angle</b>	$\phi$	–
<b>Temperature at the surface</b>	$T_{\text{surf}}$	$^{\circ}\text{C}$
<b>Surface heat flux</b>	$Q_s$	$\text{J m}^{-2} \text{s}^{-1}$
<b>Depth</b>	$z$	$\text{m}$
<b>Gas constant</b>	$R$	$\text{J mol}^{-1} \text{K}^{-1}$
<b>Volumetric rate of radiogenic heat production</b>	$\rho_H$	$\text{J m}^{-3} \text{s}^{-1}$
<b>Thermal diffusivity</b>	$\kappa$	$\text{m}^2 \text{s}^{-1}$

The visco-elasto-plastic rheology is described by a model that defines strain rate as a sum of elastic, viscous and plastic strain rates assuming Maxwell rheology:

$$\dot{\epsilon}_{ij} = \dot{\epsilon}_{ij}^{\text{el}} + \dot{\epsilon}_{ij}^{\text{vs}} + \dot{\epsilon}_{ij}^{\text{pl}} \quad (2.4)$$

where  $\dot{\epsilon}_{ij}$  are the components of the total strain rate tensor. The components of the elastic, viscous and plastic strain rate tensors are indicated by  $\dot{\epsilon}_{ij}^{\text{el}}$ ,  $\dot{\epsilon}_{ij}^{\text{vs}}$  and  $\dot{\epsilon}_{ij}^{\text{pl}}$ . The viscous strain rate is calculated by considering the creep behaviour of rocks at high temperatures (e.g. Karato and Jung 2003). The major creep mechanisms that are considered here are diffusion (for low stress) and dislocation (for high stress) creep. In order to take the solid-state creep into account, the effective viscosity  $\eta_{\text{eff}}$  is given as:

$$\eta_{eff} = F(A_D h^m f_{H_2O}^r \dot{\epsilon}_{II}^{n-1})^{-\frac{1}{n}} \exp\left(\frac{E_a + V_a P}{nRT_K}\right) \quad (2.5)$$

The magnitude of the plastic strain rate ( $\dot{\epsilon}_{ij}^{pl}$ ) is calculated using the Drucker-Prager yield criterion, where the square root of the second invariant of the stress tensor ( $\tau_{II}$ ) is limited by the plastic yield strength  $\tau_{yield}$ .

$$\tau_{II} \leq \tau_{yield} \quad (2.6)$$

$\tau_{yield}$  depends on pressure ( $P$ ) and cohesion ( $c$ ) as shown below while strain softening is not considered.

$$\tau_{yield} = \sin(\phi) P + \cos(\phi) c \quad (2.7)$$

The volumetric heat source  $H$  contains shear heating

$$H = \tau_{ij}(\dot{\epsilon}_{ij} - \dot{\epsilon}_{ij}^{el}) \quad (2.8)$$

For the calculation of buoyancy stress gradients in Eq. 2.1, we consider the density obtained from phase-diagram sections (Figure 2.2). Density  $\rho$  is a function of pressure and temperature ( $P$ - $T$ ):

$$\rho = \rho(P, T) \quad (2.9)$$

We solve the previous relationships in two-dimensions. Our two-dimensional (2D) geometry is a plane-strain approximation and assumes that all the gradients in the off-plane direction are negligible. Since we consider a single-phase approximation with respect to the deformation problem, we have assigned different “phase” properties for the asthenosphere, the mantle lithosphere, the lower and upper continental crust and for the oceanic crust. In some of the models a “weak” zone is considered in the upper oceanic crust in order to facilitate the localization of deformation at that particular point. This “weak” zone has the rheology of serpentinite and is restricted in the shallow part of the oceanic crust. Extensions of serpentine zones at larger depths are not justified since, at larger temperatures, serpentinite may not be even stable. The utility of the “weak” zone is common in analogue and numerical models of rock deformation (e.g. Chemenda *et al.* 1996; Hässig *et al.* 2016b). In this work, we do not investigate further the initial origin of this weak zone since it could be related to an initial damaged zone as suggested by Garfunkel (2006; his Fig. 4).

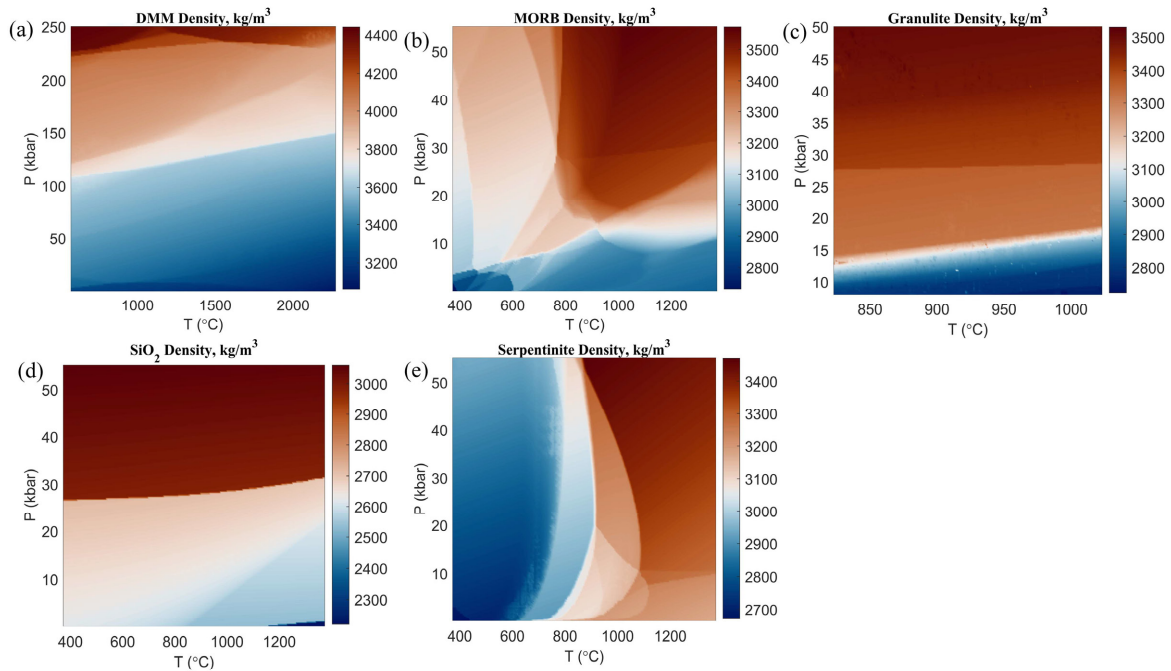


Figure 2.2 Isochemical, phase-diagram sections used for the density calculation of (a) lithospheric mantle and asthenosphere (DMM: Depleted MORB Mantle); (b) oceanic crust (MORB: Mid-Ocean Ridge Basalt); (c) lower continental crust (Granulite); (d) upper continental crust (pure quartzite composition); (e) weak zone (Serpentine).

The densities of the different “phases” were computed using isochemical, phase-diagram sections as a function of  $P$ - $T$  for several representative lithologies (Figure 2.2). We considered a Depleted-MORB-Mantle (DMM), a MORB, a granulite, a quartzite (pure  $\text{SiO}_2$ ), and a serpentinite as representative lithologies (see Table 2.2 for details). The phase-diagram sections were pre-calculated separately for each “phase” using Gibbs free-energy minimization (Connolly 2005, 2009).



Table 2.2 Description of material parameters used in model configuration

	Asthenosphere – DMM	Lithospheric mantle – DMM	Oceanic crust – MORB	Lower continental crust – Granulite	Upper continental crust – quartz	Weak zone – serpentine
<b>Density</b>	Phase diagram section (DMM)	Phase diagram section (DMM)	Phase diagram section (MORB)	Phase diagram section (dry granulite)	Phase diagram section (SiO <sub>2</sub> )	Phase diagram section (hydrated peridotite)
<b>Dislocation creep rheology</b>	Dry olivine power-law after (Faul <i>et al.</i> , 2011)	Dry olivine power-law after (Faul <i>et al.</i> , 2011)	Dry diabase after (Mackwell, Zimmerman and Kohlstedt, 1998)	Plagioclase after (Rybacki and Dresen, 2000)	Wet Quartzite after (Ranalli, 1995)	Tumut Pond Serpentine after (Raleigh and Paterson, 1965)
<b>Diffusion creep rheology</b>	Dry olivine power-law after (Faul and Jackson, 2007)	Dry olivine power-law after (Faul and Jackson, 2007)	-	-	-	-
<b>Conductivity (W m<sup>-1</sup> K<sup>-1</sup>)</b>	69.63	3	3	3	3	3
<b>Heat capacity (J kg<sup>-1</sup> K<sup>-1</sup>)</b>	1050	1050	1050	1050	1050	1050
<b>Thermal expansion (K<sup>-1</sup>)</b>	3·10 <sup>-5</sup>	3·10 <sup>-5</sup>	3·10 <sup>-5</sup>	3·10 <sup>-5</sup>	3·10 <sup>-5</sup>	3·10 <sup>-5</sup>
<b>Shear modulus (Pa)</b>	5·10 <sup>10</sup>	5·10 <sup>10</sup>	5·10 <sup>10</sup>	5·10 <sup>10</sup>	5·10 <sup>10</sup>	5·10 <sup>10</sup>
<b>Cohesion (Pa)</b>	10·10 <sup>6</sup>	10·10 <sup>6</sup>	10·10 <sup>6</sup>	10·10 <sup>6</sup>	10·10 <sup>6</sup>	10·10 <sup>6</sup>
<b>Friction angle</b>	30	30	30	30	30	30

We consider a model domain (in 2 dimensions) for a region of 1000 km by 700 km. More details on the particular geometry that was employed can be found on Figure 2.3. To simulate the convergence boundary conditions we consider an inflow of material from the upper-left part of the model domain. The lower-left part of the model domain has outflow boundary conditions consistent with the overall mass conservation in the model domain (the bottom and right boundaries have free-slip boundary conditions). The employed inflow-outflow conditions are necessary for problems where kinematic boundary conditions are needed and conservation of mass is respected in an Eulerian frame (c.f. Porkoláb *et al.* 2020). In order to simulate a free top surface, we consider a 30 km-thick, low-viscosity layer (sticky air) and an open, stress-free top boundary. Regarding the bottom boundary our bottom boundary condition is set at 670km depth. However, given the large distance from the region of interest (yellow frame in Figure 2.3), changing the bottom boundary conditions to “no-slip”, or moving the bottom boundary at 400 km depth makes no difference to the main results (Figure S 1; supplementary material).

Figure 2.3 (b) shows in detail the initial geometrical configuration considered. Clearly, there is not a unique way to constrain all the different lithological contacts. For example, we have chosen that the oceanic crust is initially below the rocks of the continental margin (Figure 2.3 (b)). This choice is not unique and one could also choose the opposite (e.g. Figure S 2 (e); Supplementary material). The latter approach, however, makes it difficult to distinguish if the oceanic crust on top of a continental margin is the result of obduction or if it is the result of the initial condition. For this reason, we will not consider this initial configuration further and will focus on the geometry shown in Figure 2.3.

The initial thermal structure of the continental and the oceanic domains has been

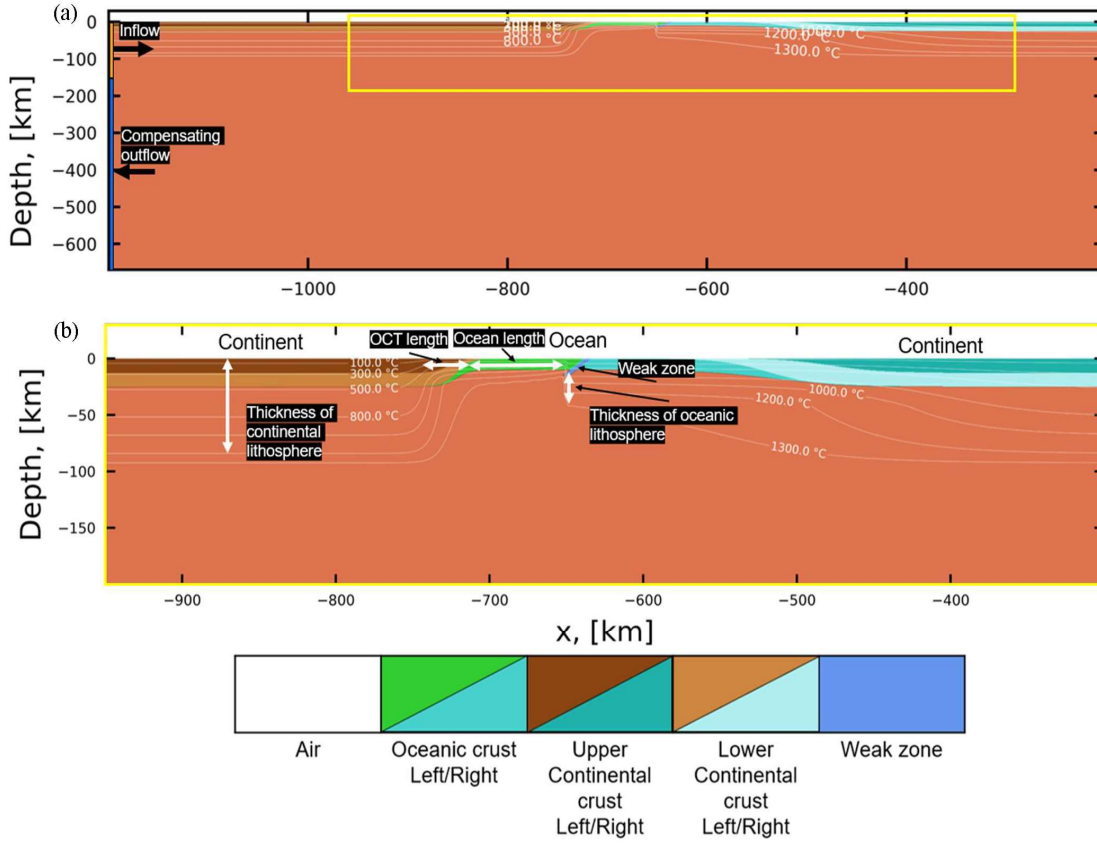


Figure 2.3 Initial model configuration of the reference model (only central part of the model is shown). The converging flow assumes a material inflow from the left boundary and an associated compensating outflow at depth (black arrows in (a)). The boundary conditions on the right and at the bottom of the extended model domain assume free slip. The top of the model (0-30 km) is composed of “sticky air” to account for a (stress) free surface. The geometrical features of the model that are used in the systematic investigation are labels using the boxes in black (b). The initial isotherms are shown in thin white lines. (a) Full model. (b) Detail of model (yellow box).

calculated using simple analytical approximations. The temperature profile under continent is built using three different analytical solutions. At the top (from surface to Moho) we consider the steady-state temperature distribution having a constant radiogenic heat production for the whole crust, that is:

$$T = T_{surf} + \frac{Q_s}{\lambda} z - 0.5 \frac{\rho_H}{\lambda} z^2, \quad (2.10)$$

where  $T_{surf}$  is temperature at surface,  $Q_s$  is a surface heat flux,  $\lambda$  is a thermal conductivity,  $z$  is depth,  $\rho_H$  is the volumetric rate of radiogenic heat production. Due to the minor radiogenic heat production in the mantle, we utilize a linear temperature gradient that extends from the Moho depth until the LAB that is set at 1200 °C. The final (deeper) part of the temperature distribution in continental regions is a linear gradient from LAB to the bottom of the model domain where the temperature is set to be 1612 °C (at 670 km). In order to ensure a continuous heat flux

across the last two zones, we have modified the effective heat-conductivity coefficient. This approach leads to significantly larger heat conductivities for the asthenosphere but accounts for the adiabatic temperature gradient in the mantle (Currie *et al.* 2008). The temperature profile under the oceanic crust is calculated using a half-space cooling model (Turcotte and Oxburgh 1967):

$$T = (T_{\text{surf}} - T_{\text{LAB}}) \operatorname{erf}\left(\frac{z}{2\sqrt{\kappa t_0}}\right) \quad (2.11)$$

where  $T_{\text{LAB}}$  is a temperature at lithosphere-asthenosphere boundary,  $\operatorname{erf}(x)$  is the error function,  $\kappa$  is the thermal diffusivity,  $t_0$  is the age of the oceanic lithosphere at the centre of the oceanic region. The temperature structure in the OCT zone is a weighted average of the two end-members, using the distance from the ocean and the continent as weighting factors. The respective material parameters are given in Table 2.2.

### 2.2.2 Systematic investigations

In this work we have focused on the geometrical and rheological parameters that can potentially affect the evolution of our simulation and lead to the emplacement of the oceanic crust onto the continental margin. The role of the magnitude of convergence velocity and the rheology of the lower-continental crust were also explored (Table 2.3 and Table 2.4). The geometrical parameters that we explored are (Figure 2.3): a) the size (length in 2D) of the oceanic basin, b) the length of the OCT, c) the initial age of the oceanic lithosphere at the centre of the ocean, and d) the presence and orientation of a weak zone at the centre of the oceanic domain. Our varied parameters are shown in Table 2.5. Several models were calculated using minimal, average, and maximal values of the respective parameters. The average values were chosen as reference values (Table 2.5).

*Table 2.3 Dislocation creep parameters used in LaMEM*

Dislocation creep profile	Dry olivine	Dry diabase	Plagioclase	Plagioclase (wet)	Wet Quartzite	Tumut Pond Serpentine	Units	
$Bn$	0.3	8	$5.01 \cdot 10^1$	1.6	$3.2 \cdot 10^{-4}$	$6.3 \cdot 10^{-7}$	$\text{Pa}^{-n} \text{ s}^{-1}$	Pre-factor
$n$	8.2	4.7	3	3	2.3	2.8	-	Power-law exponent
$Ea$	$6.82 \cdot 10^5$	$4.85 \cdot 10^5$	$6.74 \cdot 10^5$	$3.45 \cdot 10^5$	$1.54 \cdot 10^5$	$6.6 \cdot 10^4$	$\text{J MPa}^{-1} \text{ mol}^{-1}$	Activation Energy
$Va$	0	0	$2.4 \cdot 10^{-5}$	$3.8 \cdot 10^{-5}$	0	0	$\text{m}^3 \text{ mol}^{-1}$	Activation volume
Type				Uniaxial			-	Test type
$f_{\text{H}_2\text{O}}$	1	1	1	158.5	1	1	$Pa$	Water fugacity

Table 2.4 Diffusion creep parameters used in LaMEM

Diffusion creep profile	Dry olivine	Units	
$Bd$	$2 \cdot 10^{10}$	$Pa^{-n} s^{-1}$	Pre-factor
$Ea$	$4.84 \cdot 10^5$	$J MPa^{-1} mol^{-1}$	Activation Energy
$Va$	$1.5 \cdot 10^{-5}$	$m^3 mol^{-1}$	Activation volume
Type	Uniaxial	–	Test type
$d_0$	$1 \cdot 10^{-3}$	$m$	Grain size
$p$	3	–	Exponent of a grain size
$f_{H_2O}$	1	$Pa$	Fugacity of $H_2O$
$r$	0	–	Power-law exponent in $f_{H_2O}$

Table 2.5 Range of values used in model configuration

Parameter	Range (minimum – reference – maximum)	Units
Ocean length	40 – 60 – 90	km
$\Delta t_o$	0 – -2 – 2	Myrs
OCT length	30 – 50 – 250	km
Convergence Velocity	3 – 5 – 10	cm/year

Clearly our choice of parameters is not unique and more complex scenarios can be investigated. For example, we have assumed for our main systematics results is that velocity is taken as constant during convergence. This is likely not the case in nature and, in fact, it is expected that velocities are reduced during the collision stage. Apart from the models shown in the main systematics study, we have calculated models (Figure 2.8 (a-d) and Figure 2.8 (i-l)) that show the effect of reduced converging velocity with time (from 5cm/yr to 1cm/yr between 5 and 10 myr). The exact converging velocity that was used in our models is given in Figure S 3 (supplementary material). As a final simplification we would like to mention that in all the models presented in the systematics study we have ignored the effects of erosion. Models with constant erosion rates are shown in Figure 2.8 and in Figure S 4 of the supplementary material.

## 2.3 Results

More than 200 numerical simulations were calculated using the model configuration shown in Figure 2.3. Due to the large number of computed results, we chose the results of a particular model as a reference and we have systematically varied the different parameters. The reference model has a convergence rate of 5 cm/year from the left boundary (Figure 2.4 (a-d)). The initial thickness of the lithospheric mantle, in the middle of the oceanic region, is slightly different depending on the position with respect to the centre of oceanic domain (left or right). This difference in thickness is calculated based on the depth where the temperature becomes larger than 1,200 °C when using Eq. (2.11). Thus, this age difference is a function of  $t_o$  in Eq. (2.11). By choosing different  $t_o$  for the right- or left-side of the central region ( $t_o^{left} - t_o^{right} = \Delta t_o$ ), we can generate an initially symmetric ( $\Delta t_o = 0$ ) or asymmetric temperature distribution ( $\Delta t_o \neq 0$ ). This asymmetry can cause asymmetric subduction upon convergence and can be expected to occur across transform faults near the Mid-Ocean-Ridge (see Fig. 4 of Garfunkel 2006 for details). For the reference model  $t_o^{left}$  is 0 and  $t_o^{right}$  is 2 myr, thus  $\Delta t_o = -2$  myr. The length of the OCT in the reference model is 50 km and length of the ocean on the left side of the reference model is 60 km. In addition to the previous configuration, we have considered a weak zone (i.e., serpentine material) in the middle of the oceanic domain to facilitate the localization of deformation (see section METHODS for details).

### 2.3.1 Reference model and influence of convergence velocity

After approximately 2 million years of convergence in the reference model, we observe the beginning of the development of an intra-oceanic subduction zone from the right part of the oceanic plate towards the left part of the model domain (Figure 2.4 (b)). As convergence progresses, there is a switch in the polarity of the subduction zone to the left side of the oceanic domain (at ca 5 Ma; Figure 2.4 (c)). The switch in the subduction polarity is responsible for the emplacement of a part of the oceanic plate onto the continental margin that was initially positioned on the right of the oceanic domain (Figure 2.4 (c-d)). This final geometry is in essence a suture zone. This is because it is composed of deformed rocks and, within this deformed zone, rocks of oceanic affinity crop out at the overriding plate (for more details see

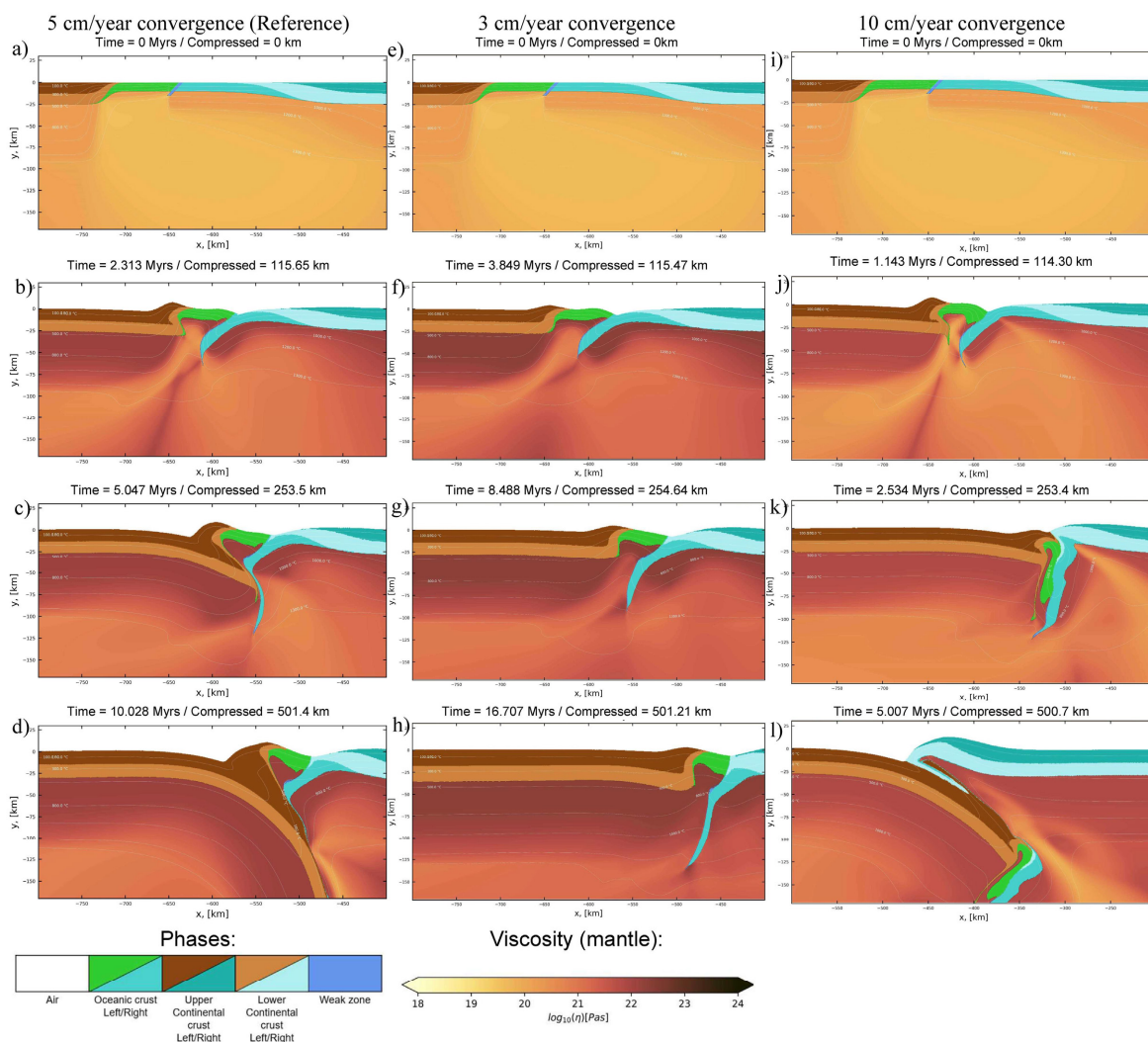


Figure 2.4 Model results showing the evolution of different model configurations as a function of convergence velocity: (a-d) convergence velocity of 5 cm/year (reference model); (e-h) 3 cm/year; (i-l) 10 cm/year. Note that in these model results, high ( $>5$ cm/year) convergence velocities do not lead to the obduction of the oceanic crust but they rather lead to the continental subduction of the left continental margin.

Figure 2.8 and DISCUSSION). In the model results shown in Figure 2.4 (e-h), we have kept the same initial configuration but we used a convergence velocity of 3 cm/yr. This change leads initially to qualitatively similar results although the absolute amount of displacement is smaller (Figure 2.4 (e-h)). However, even after a period of 8 myr, the convergence is not sufficient and the buoyancy structure is such (Figure 2.4 (e-g)) that it is not possible to develop a polarity flip zone as shown previously (Figure 2.4 (g-h)). Thus, velocities in the order of 3cm/yr and slower are not sufficient to create an apparent obduction and a subduction-polarity flip. Keeping the same parameters, and using larger convergence velocity (10 cm/yr; Figure 2.4 (i-l)) leads to a similar initial development of an intra-oceanic subduction zone as well (Figure 2.4 (j)). A change in the subduction polarity occurs soon after this period (Figure 2.4 (k)) and the continuation of convergence leads finally to the subduction of the continental lithosphere (Figure 2.4 (l)). In the models with larger convergence velocity (10 cm/yr), the emplacement of the oceanic crust on the right continental margin was not achieved. To summarize the effect of velocity on the obduction process we see that, using our initial configuration, it is possible to obtain an apparent obduction and a subduction-polarity flip only if the convergence velocity is moderately high (5cm/yr). Larger velocities lead to the complete subduction of the ocean and smaller velocities do not result in continuing subduction.



### 2.3.2 Influence of initially asymmetric temperature distribution

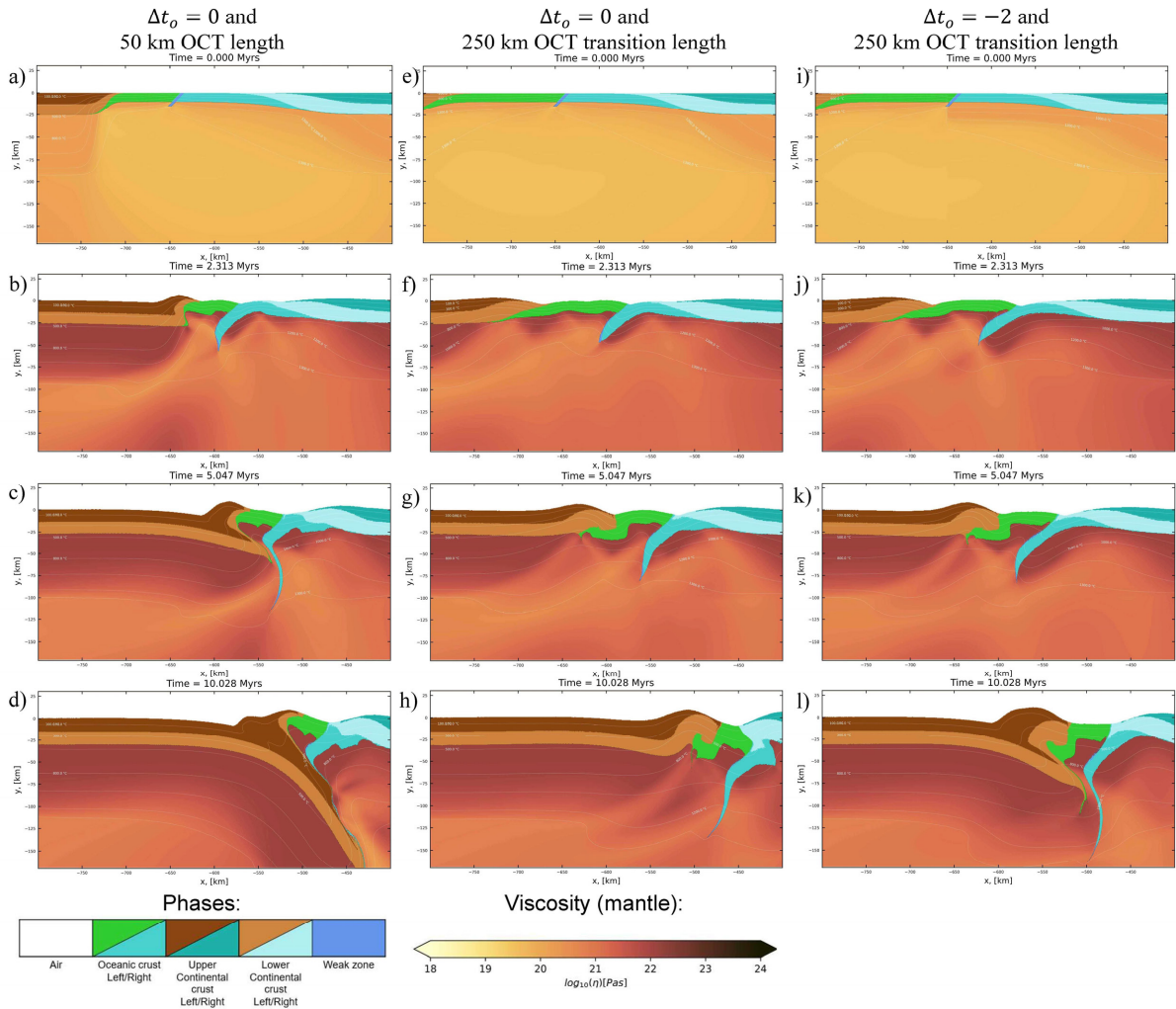


Figure 2.5 Model results showing the evolution of different model configurations as a function of the initial asymmetry in the thickness of the oceanic lithosphere and as a function of the initial length of the OCT. The oceanic lithosphere across the weak zone may have a slight asymmetric age distribution in order to consider an initially asymmetric model configuration: (a-d) with  $\Delta t_o = 0$  and OCT length as in reference model; (e-h) with a larger ocean-continent transition zone (250 km) and  $\Delta t_o = -2$ ; (i-l) combined features from first and second series.

The initial model configuration shown in Figure 2.5 (a-d) considers a slightly more symmetric temperature distribution of the oceanic domain (Figure 2.5 (a);  $\Delta t_o = 0$  myr). However, the initial temperature distribution is not perfectly symmetric due to the difference in length of the OCT zones. The rest of the model parameters are as they are given for the reference model. The model results shown in Figure 2.5 (a-d) are, in general, very similar to the reference model results. A major difference in these results is that the intra-oceanic subduction angle in Figure 2.5 (b) is steeper compared to the reference model at approximately the same time (Figure 2.4 (b,c)). Another difference in these results is that the oceanic crust in the more symmetric case appears to be slightly folded (or buckled) compared to the reference case (e.g.

compare Figure 2.4 (b-c) and Figure 2.5 (b-c)). At about 10 myr (Figure 2.5 (d)), we observe the subduction-polarity flip that leads to the complete closure of the ocean and the formation of a suture zone at the surface in a way similar to the model results shown in Figure 2.4 (d).

Figure 2.5 (e-h) shows a model similar to the one described previously (Figure 2.5 (a-d)). The main difference this time is the consideration of a larger OCT zone (250km) and a larger length for the left side of the ocean compared to the model shown in Figure 2.5 (a-d). This model shows an initial development of an intra-oceanic subduction in agreement with all previous models (Figure 2.5 (f)). However, the large length of the oceanic region makes it easier to localize the deformation at the left OCT than to continue with the development of the intra-oceanic subduction (Figure 2.5 (g)). Buckling of the oceanic crust is also observed at the initial stages of convergence (Figure 2.5 f). Nevertheless, in contrast to the reference model, the continuous convergence for 10 myr (Figure 2.5 (h)) does not lead to a subduction-polarity flip despite the fact that the right OCT is now deformed (Figure 2.5 (h)). Figure 2.5 (i-l) shows the model results for a very similar setup but considering an initially asymmetric temperature structure ( $\Delta t_o = -2$ ). In other words, Figure 2.5 (i-l) show the combined effects of initial asymmetry and of the OCT length. In this case, the initial intra-oceanic subduction is developing only for a few million years ( $<5$ ) where the oceanic crust appears to be initially buckled. A polarity switch in the subduction zone is observed after 5 myr (Figure 2.5 (j-l)). The continuous convergence leads to the formation of a suture zone and of accretionary wedge atop the subducting lithosphere (Figure 2.5 (l)). At this point it is worth mentioning that all three-model configurations of Figure 2.5, have a stage (at ca 5 myr) where the oceanic crust is thrust upon the right continental margin (Figure 2.5 (c,g,k)). This thrusting however is not maintained with continuing compression for all cases. In fact, Figure 2.5 (h) shows that the main thrust of Figure 2.5 (g) has been rotated and the contact of the oceanic crust with the right continental margin dips to the right side of the model domain. In the other two cases (Figure 2.5 (d) and (l)), the initial thrusting contact dips to the left of the model domain and could be interpreted as a thrust contact where the oceanic crust is thrust upon the continental margin.

### 2.3.3 Influence of weak-zone orientation and initial asymmetry

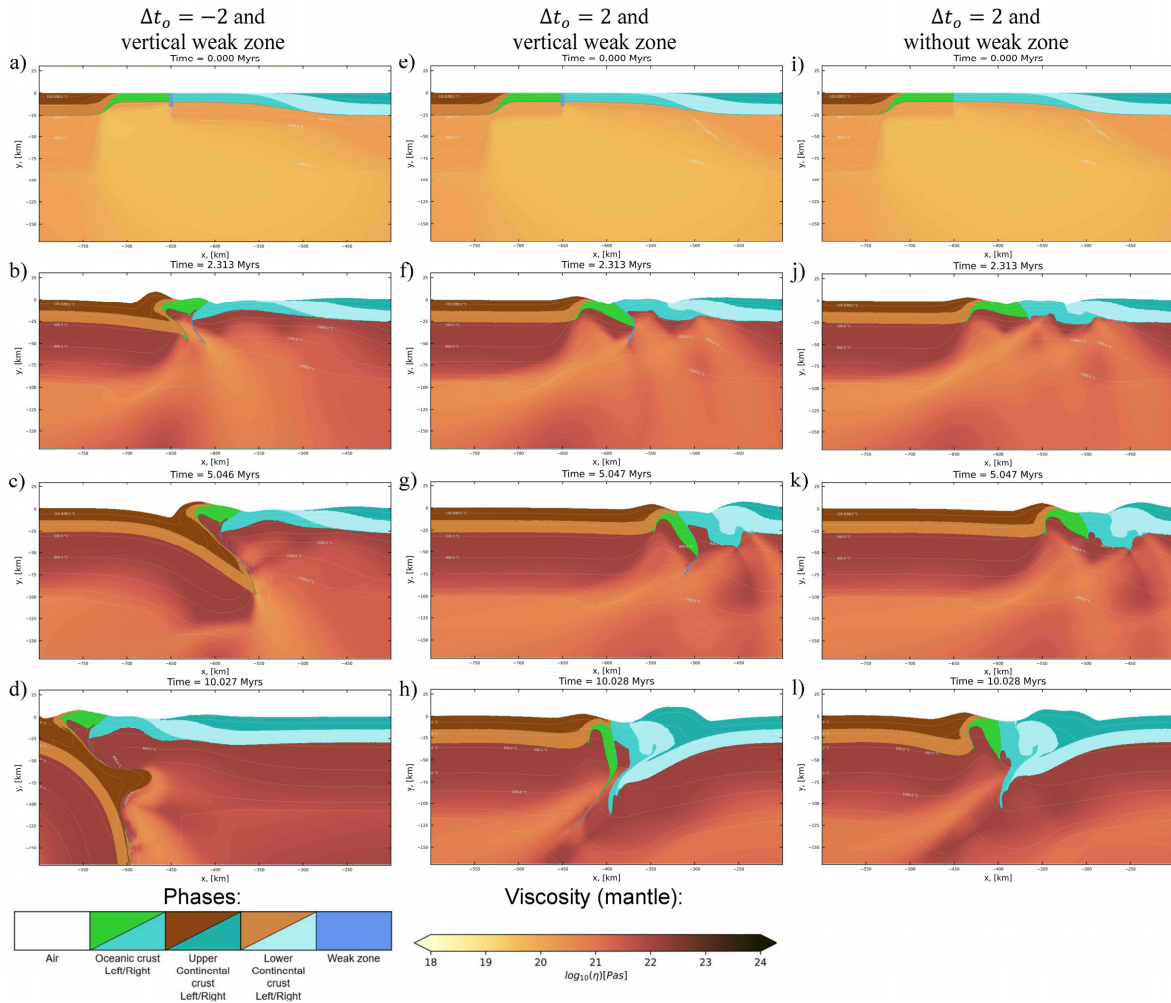


Figure 2.6 Model results showing the evolution of different model configurations as a function of the initial asymmetry in the thickness of the oceanic lithosphere and as a function of the shape or presence of the central weak zone: (a-d) with  $\Delta t_0 = -2$  as in reference model but with a vertical weak zone; (e-h) with  $\Delta t_0 = 2$  and with vertical weak zone; (i-l) with  $\Delta t_0 = 2$  as in (e-h), but without weak zone.

Figure 2.6 shows the effect that a vertically-oriented central weak zone and the initial temperature asymmetry have on the final modelled geometry. All the other parameters are as in the reference model (Figure 2.4 (a)). Figure 2.6 (a-d) show the model results for the case where  $\Delta t_0 = -2$  myr (as in the reference model), but with a vertical weak zone at the centre of the oceanic region. The presence of the vertical weak zone in Figure 2.6 (a) is not sufficient to facilitate the formation of an intra-oceanic subduction zone (e.g. Figure 2.6 (b)) and, in fact, a significant amount pure-shear thickening was observed for the oceanic region (Figure 2.6 (b)). Despite the fact that the intra-oceanic subduction was not developed, we observe the development of a subduction zone that is dipping to the right side of the model domain (Figure 2.6 (c)). Continuing convergence after  $\sim 10$  million years leads to the formation of an

accretionary wedge while a large part of the oceanic lithosphere remained at the surface of the model domain (Figure 2.6 (d)).

Keeping the weak zone vertical and switching the asymmetry of the initial temperature distribution ( $\Delta t_o = +2$  myr) leads to results that show evidence for significant intra-oceanic deformation but without the development of a subduction zone during the first 5 myr (Figure 2.6 (e-g)). The continuation of converge leads to the development of an accretionary wedge and a subduction zone from the right-side of the model domain (Figure 2.6 (h)). Keeping the same parameters as in Figure 2.6 (e-h) and removing the initial weak zone leads to model results that do not predict the subduction initiation until 10 myr (Figure 2.6 (i-l)). These results resemble a “Zwischengebirge” (Kober 1952) in the sense that the uppermost part of the lithosphere forms a doubly-verging thrust wedge without the subduction of the underlying lithosphere. In all of the presented models of Figure 2.6, the thrusting of the oceanic rocks on the continental margins was not observed.

#### 2.3.4 Influence of lower-crustal rheology

Figure 2.7 shows model results following the same systematic change as in Figure 2.5. The main difference in the models shown in Figure 2.7 is that the lower-crustal rheology for the continental region is weaker (i.e. a “wet plagioclase” flow law was used). To a first approximation the results shown in Figure 2.7 (a-d) are similar to the ones shown in Figure 2.7 (a-d). The main difference is that the models with a “weaker” lower-crustal rheology show a more pronounced deformation in the lower crust in both sides of the model domain (Figure 2.7 (c)). As a result, at ca 5 Ma we observe the beginning of the formation of two converging

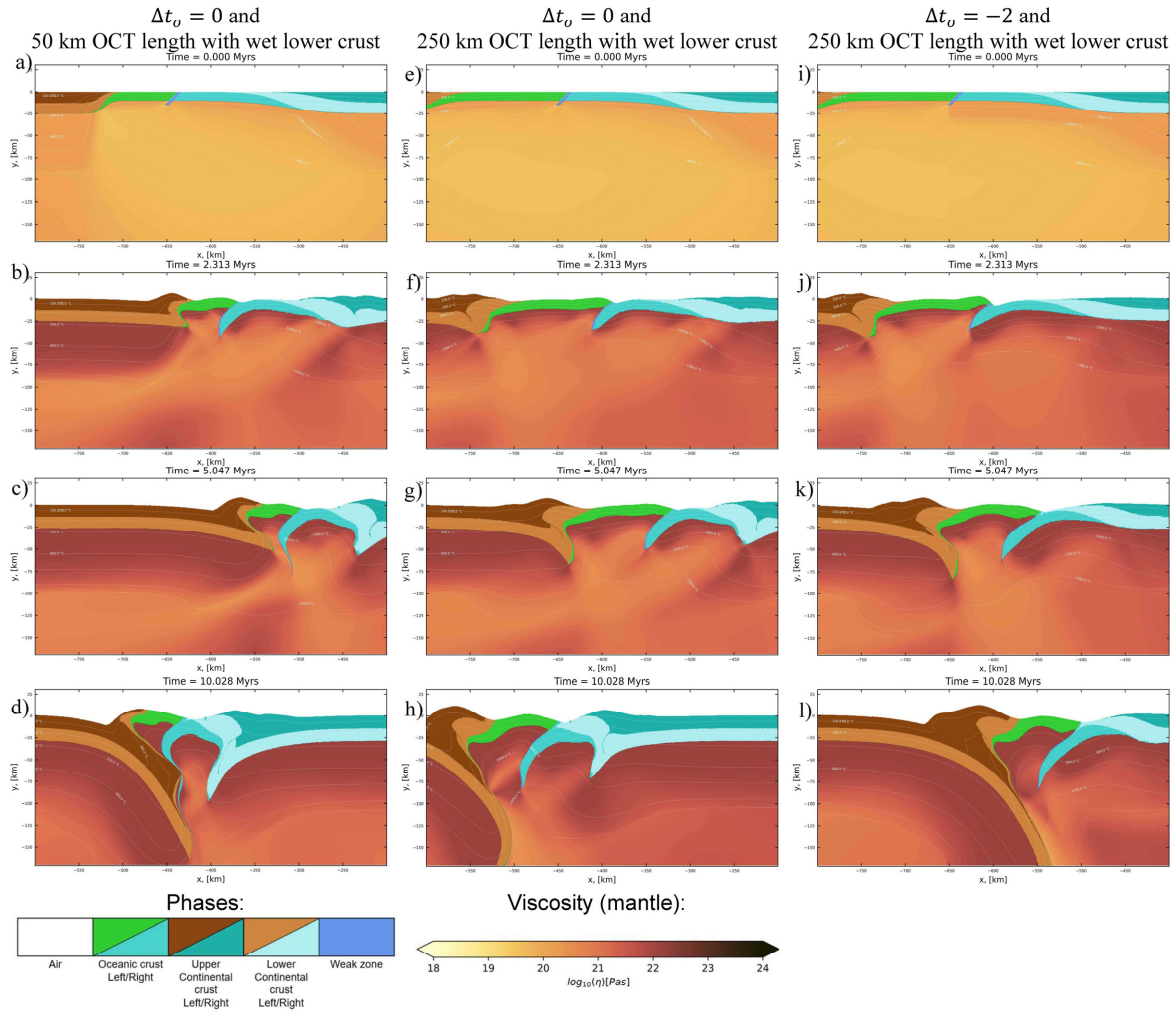


Figure 2.7 As in Figure 2.5 but using a “wet” lower-crustal rheology.

subduction zones (Figure 2.7 (c-d)). However, the subduction zone at the left side of the model domain is more pronounced (Figure 2.7 (d)).

Keeping the same parameters in the model configuration as before, and changing the length of the left OCT region leads to the development of a subduction zone mainly from the left side of the model domain (Figure 2.7 (e-h)). To a first order, the same results are observed even if the initial temperature distribution was more asymmetric ( $\Delta t_0 = -2$ , Figure 2.7 (i-l)). All models shown in Figure 2.7 show the thrusting of the oceanic crust on the continental parts on the right side of the model domain at ca 10myr (Figure 2.7 (d,h,l)). In summary, making the lower continental crust weaker leads to more pronounced deformation of the lower-crustal layers that can act as nucleation points for the localization of deformation (e.g. Figure 2.7 (b,c)).

### 2.3.5 Influence of reducing velocity and erosion

To summarize our systematic investigation, we have shown that it is feasible to create the conditions necessary for ophiolite obduction (Figures 2.4-2.7). The thrusting of the oceanic



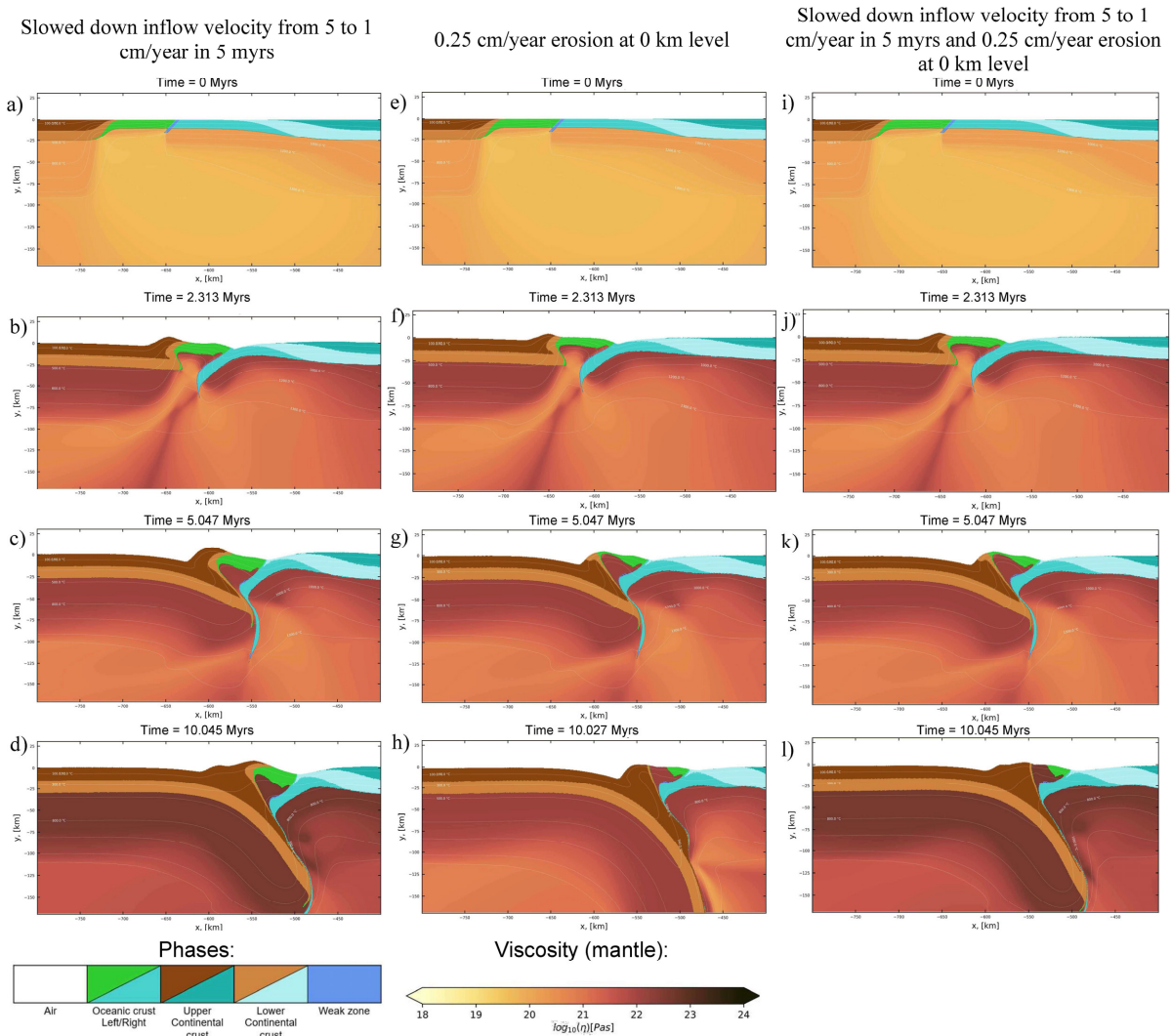


*Figure 2.8 Model results showing the effect of slowing converging velocity and/or constant erosion rate on the reference model (Figure 2.4). Initial model configuration as in the model shown in Figure 2.4. (a-d) Reference model with slowing converging velocity from 5cm/yr to 1cm/yr (see Figure S 3 in supplementary material for details). (e-h) Reference model with a constant erosion rate of 0.25cm/yr imposed at ( $y > 0$ ). (i-l) Combined effects of erosion and decreasing convergence velocity.*

crust on the right side of the model domain is not much but it can also be distinguished from the increased plastic strain in the oceanic/continental contact (Figure S 5; supplementary material). The results from the systematic investigation were calculated assuming no erosion and constant convergence velocity for simplicity. Thus, in some cases, our produced results have unrealistically large topography. In nature, erosion and reduced convergence rates can act to moderate topography. Adding two additional variations in the model parameters increases the investigated parameter space and requires more systematic investigations. The influence of erosion rates and variable boundary velocity goes beyond the scope of the present study and will not be considered in detail. However, we have included the effects of constant erosion in the reference model shown in Figure S 4 (supplementary material). In general, erosion

moderates the high topography and contributes to the exhumation of the ophiolite. The results show that with erosion rates (assumed constant) in the order of 0.25 cm/yr, it is possible to exhume also part of the mantle lithosphere that was originally below the oceanic crust (Figure S 4 (e-h)). Larger erosion values lead to the disappearance of the ophiolite crustal sequence (Figure S 4 (a-d)) whereas smaller erosion rates do not lead to the exposure of the mantle rocks at ca 10 myr after the onset of convergence (Figure S 4 (i-l)). Regarding the effects of decelerating convergence rate, we have calculated two models that consider the reduction of the convergence velocity to 1cm/yr at 10myr (Figure S 3; supplementary material). The results show that the model with reduced velocities has similar qualitative characteristics with the reference model (Figure 2.8 (a-d)). These characteristics include the initial intra-oceanic subduction towards the left side of the model domain (Figure 2.8 (b)) and the thrusting of the oceanic crustal rocks atop the continental margin of the right side of the model domain (Figure 2.8 (c-d)). However, Figure 2.8 (d) has a more moderate topography compared to the reference model of Figure 2.4 (d).

Figure 2.8 (e-h) shows that erosion with a constant rate of 0.25 cm/yr is also capable of reducing the topographic variations as shown also in Figure S 4 (supplementary material). However, the combined effects of erosion and reducing convergence velocities (Figure 2.8 (i-l)) have a more realistic topographic variation and show the exposure of an “ophiolite sequence” (including the mantle section) on the surface of the formed orogenic wedge (Figure 2.8 (l)). What is clear in all models where the over thrusting of the oceanic-crustal rocks was achieved on the right side of the model domain, is that the conditions that favour obduction require a relatively small oceanic basin (ca 200 km) and relatively fast initial convergence rates. The slowing down of the convergence from 5 to 1 cm/yr (from 5 myr to 10 myr) does not significantly affect this main result (Figure 2.8 (a-d)).

### 2.3.6 The pressure and temperature (P-T) evolution of the crustal ophiolite rocks and their accretion to the overriding plate

By investigating the reference model further, we can look into the pressure and temperature ( $P$ - $T$ ) evolution of selected material points (markers). We have selected 6 points from the left oceanic region of the reference model (Figure 2.9). Half of the markers (bluish colours) originate from the left part of the OCT zone at the left side of the model domain (Figure 2.9 (a)). The other half of the markers originate from the right part of the OCT region close to

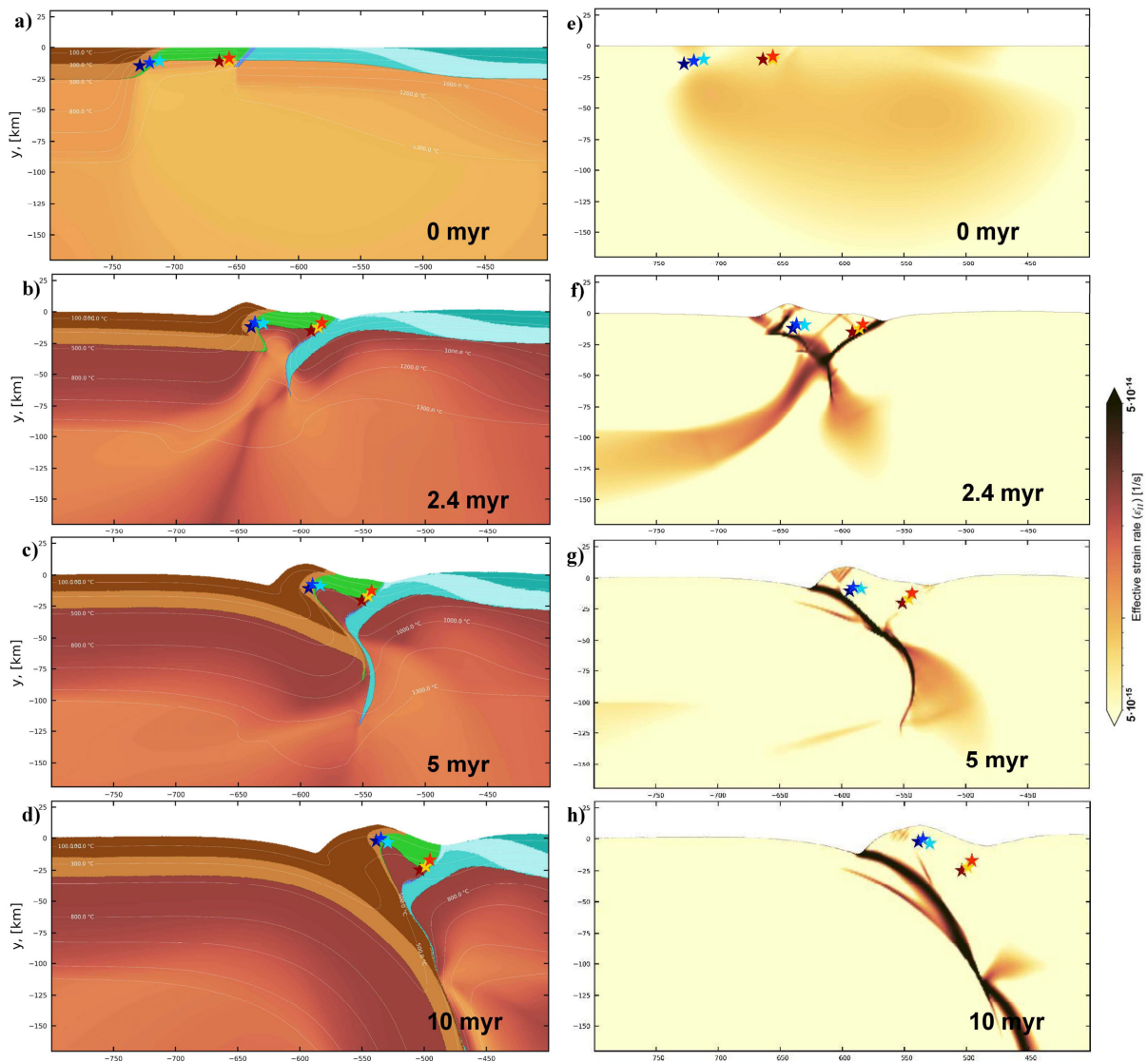


*Figure 2.9 Model evolution and position of P-T markers as a function of time. (a-d) Evolution of the reference model (Figure 2.4(a-d)) with respective location of the markers (colored stars); (e-h) show the effective strain rate for the same region that is shown in (a-d). The effective strain rate is the square root of the second invariant of the strain rate tensor. Dark colors indicate domains of relatively fast deformation.*

the centre of the ocean (Figure 2.9 (a)). At the end of the simulation, these markers are found



to be parts of the oceanic part that was incorporated in the orogenic wedge (Figure 2.9 (a-d)). Figure 2.9 also shows the evolution of the effective strain rate of the reference model (Figure 2.9 (e-h)). Values of large effective strain rate show the intensity of the deformation at a given time. The effective strain rate distribution shows the evolution of a left-dipping intra-oceanic subduction zone into a doubly-vergent orogenic wedge at ca. 2.4 Ma (Figure 2.9 (f)). At 5 myr, deformation is localized left of the suture zone and the ophiolite has already been accreted in the overriding plate (Figure 2.9 (g-h)). The significance of the effective strain rate becomes apparent if one considers that this is the zone of fastest deformation rates and it is, in fact, a new plate boundary (Figure 2.9 (e-h)). This means that the actual plate boundary has migrated from 5 to 10 myr towards the left side of the model. This migration marks the time when the rocks of oceanic affinity are incorporated in the overriding plate of the subduction system. As it was already mentioned, the increased finite deformation in the orogenic wedge, and the location of rocks with oceanic affinities “outcropping” at the surface of the overriding plate (Figure 2.9 (h)) can be used to characterize this high-deformation zone as a suture zone (see also plastic strain distribution; Figure S 5, supplementary material).

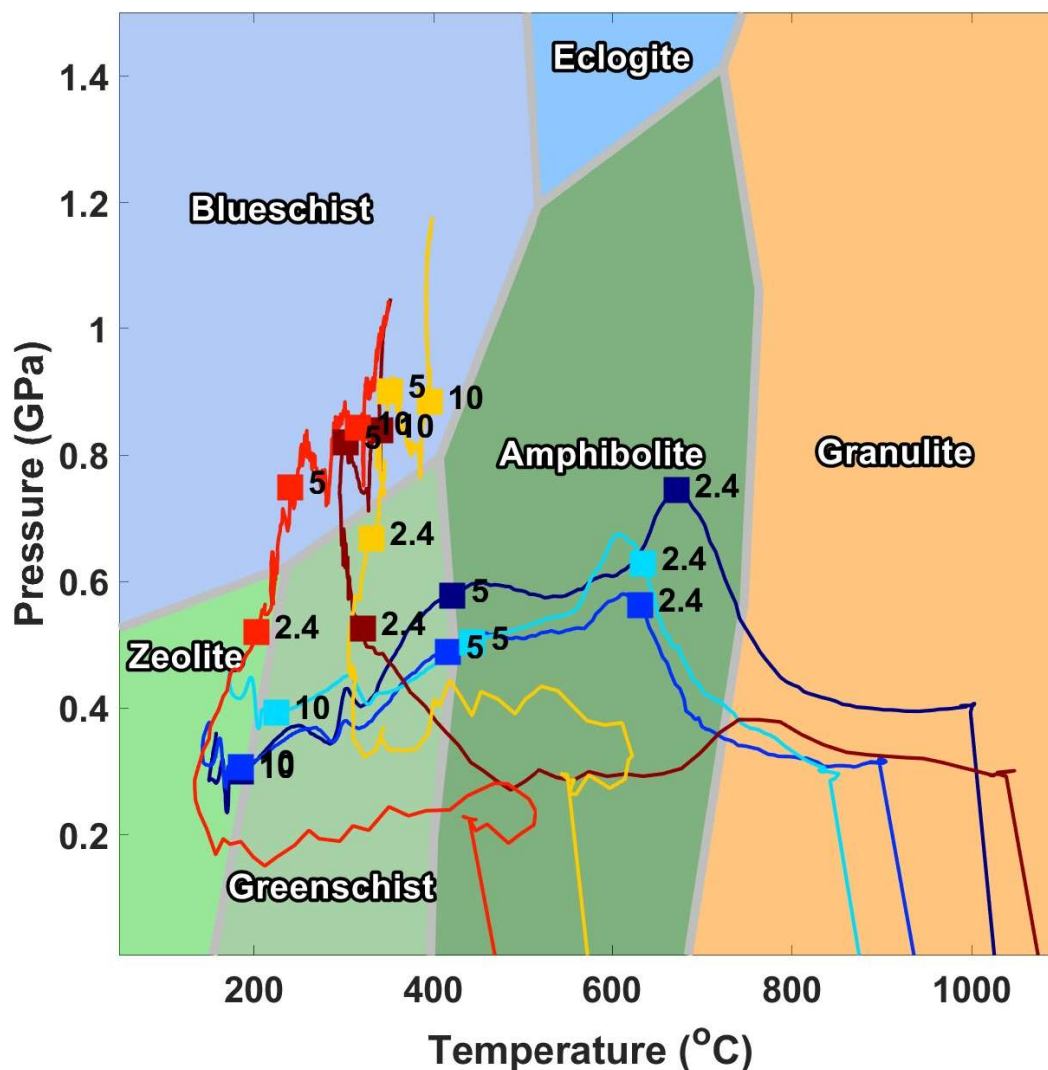


Figure 2.10  $P$ - $T$  paths of markers with respect to the metamorphic-facies boundaries (after Stüwe 2007). The black numbers correspond to the time in millions of years.

The  $P$ - $T$  evolution of the markers of the reference model is shown in Figure 2.10. This figure shows the  $P$ - $T$  extent of the classic metamorphic facies. The lines in this figure show the  $P$ - $T$  evolution of selected material points (markers) shown in Figure 2.9. The numbers on the coloured curves correspond to the time (in myr) after convergence initiation. Figure 2.10 shows that the initial cooling of the oceanic rocks is followed by an increase in pressure that is associated with the final stages of the closure of the ocean at approximately 2.5 myr. At this stage, the markers originating from the left side of the OCT experience pressures of 0.5-0.7 GPa for a temperature range between 550 and 700°C (amphibolite-facies conditions; see Figure 2.10). These conditions could lead to the crystallization of amphibolites that are located above a subducting continental margin as shown in Figure 2.9 (b). The positioning of these rocks atop a subducting and dehydrating continental margin is crucial in order to explain the formation of hydrous lithologies in relatively young oceanic crust. At the same time, the markers originating

from the right side (middle of oceanic region) experience greenschist-facies conditions (Figure 2.10). It is interesting to note that all markers are located next to zones of active deformation (Figure 2.9 (b,f)). These zones of active deformation are similar to the pro- and retro-shear zones that develop in models of doubly-vergent orogenic wedges (e.g. Beaumont and Quinlan 1994). By 5 myr, the markers originating from the left side cool down to greenschist-facies conditions while, at the same time, the markers originating from the centre of the ocean have already cooled down and they experience blueschist-facies metamorphism at the back-thrust region (Figure 2.9 (g), 2.10).

## 2.4 Discussion

Our simulations demonstrate that it is possible to achieve ophiolite obduction under continuous regional compression and without applying far field-extension. As obduction we refer to the thrusting of the oceanic rocks upon the continental margin in the right side of the model domain. However, the subduction of continental material below the oceanic rocks (from the left side) supports the interpretation of a structural uplift in exhumed ophiolites. The obduction was possible when the convergence velocity was around 5 cm/yr (Figure 2.4). These numbers, although on the high side, are realistic and well within the velocities inferred for the initial stages of continental collision (Molnar and Stock 2009). We note also that such high convergence velocities do not need to be maintained for large periods of time as it was shown in the model with slowing convergence (Figure 2.8; Figure S 3 in the Supplementary material). Furthermore, our models revealed that it is necessary to have certain geometrical features and have an initial asymmetry in the structure of the ocean and the continental margin. One of the most important features, that is essential in leading to ophiolite obduction, is the initial asymmetry in the thickness of the oceanic lithosphere. This asymmetry may be the result of the: a) asymmetric spreading velocity, b) the asymmetric form of the OCT zones and on c) the different age of the walls across a transform zone (Garfunkel 2006a). The asymmetry in the thermal structure of the oceanic lithosphere leads to an asymmetric density distribution that can facilitate the initial subduction process (Cloos 1993a). This asymmetry was also an essential part of previous geodynamic obduction models (c.f. Duretz *et al.* 2016; Hässig *et al.* 2016a).

At this point we note that the thicker, and colder, lithospheric mantle is also mechanically stronger. At a first glance this increase in strength can prevent the rupture of the oceanic lithosphere (Stüwe 2007b), and therefore, a balance must be found between the strength and the buoyancy of the subducting oceanic plate. Finally, with respect to the properties of the

continental region, we note that the models with relatively weak lower crust did not lead to the complete closure of the ocean and did not form a “suture” zone (Figure 2.7). Thus, we found that for the generation of a suture zone that preserves significant parts of the subducting oceanic crust, the lower crust must be relatively strong.

In relation to previous mechanical models, our results are different in the sense that we do not enforce far-field extension after the initial stages of subduction (Duretz *et al.* 2016a; Hässig *et al.* 2016b, a). This allows us to investigate the possibility of ophiolite obduction under continuous convergence according to geological models (e.g. Dilek *et al.* (2007); Ghikas *et al.* (2010)). In contrast, the models of Porkoláb *et al.* (2020) are more similar to ours in the sense that the authors impose continuous convergence initially. However, in the later stages of subduction, the previous authors require that the convergence velocity of the subducting continental crust drops from 3cm/yr to near zero (Porkoláb *et al.* 2020 , p.3). With this configuration, the previous authors managed to show the relation between the exhuming subducted crust and the ophiolite emplacement. To a first order, this relation was also observed by Chemenda *et al.* (1996). However, these studies used a constant-density approximation, and therefore, the buoyancy of the subducting crust may be overestimated. To avoid this limitation, we have used density values according to the equilibrium phase diagram sections (Figure 2.2). This approach has been shown to result to more realistic buoyancy forces and topography during continental collision (Candioti *et al.* 2021).

If we now consider the relative size of the oceanic basins, our results show that small oceans are more likely to lead to the emplacement of oceanic crust. This result is in perfect agreement with geological models for Tethyan ophiolites from the Balkans that suggest that the ophiolite emplacement occurred just after the formation of the ophiolites (e.g. Garfunkel 2006). In particular, there is ample geochronological data which support that the ophiolite formation is almost contemporaneous to the crystallization of metamorphic minerals in metamorphic soles (e.g. Dimo-Lahitte *et al.* 2001; Pomonis *et al.* 2002; Liati *et al.* 2004). The very narrow age difference requires that the amount of subducted ocean was not very large, otherwise its subduction would require unrealistically high velocities. In any case, the requirement for the small relative size of the oceanic basin is also required by geologic reconstructions that consider the Tethyan ophiolites (Robertson *et al.* 1991; Robertson 2012).

Having a small oceanic basin and an initially asymmetric geometrical configuration lead to the subduction-polarity switch in our models. During the initial stages of our models, a left-dipping intra-oceanic subduction zone forms and it quickly evolves into a doubly-vergent wedge (Figure 2.4 (b-c)). During the collision stage, the left-dipping zone of high-deformation

is abandoned and most of the deformation localized at its conjugate, right-dipping shear zone. Perhaps this switch is best observed in the evolution of the effective strain rate that shows the transition from a doubly-vergent wedge to a right-dipping zone of intense deformation (Figure 2.9 (e-h)). Such a polarity switch is envisioned by several researchers who worked in the Tethyan ophiolites although the details are not always the same (Jones and Robertson 1991; Robertson *et al.* 1991; Ghikas *et al.* 2010).

The relatively fast closure of our ocean does not leave very long time for the oceanic lithosphere to cool. Thus, the ophiolite rocks experience increased pressure during the collision stage while the ocean is still relatively hot (Figure 2.10). These conditions are typically amphibolite-facies conditions (ca 530-650 °C and 5-7 kbar) and have been documented for several Tethyan ophiolites (Dilek and Whitney 1997; Pomonis *et al.* 2002a; Elitok and Drüppel 2008). An interesting result in our model is that upon cooling, some of the ophiolitic rocks experience prograde, blueschist-facies conditions with continuing convergence (Figure 2.10). It is noted however that these conditions occur at the retro-shear zone of the doubly-vergent wedge (Figure 2.9 (f); red-coloured markers). This, doubly-vergent, zone is also responsible for the accretionary uplift of the ophiolite rocks in our models in agreement to geological models proposed by Shervais (2001). This uplift is crucial for the explanation of the exhumation of the metamorphic sole rocks.

Our modelled  $P$ - $T$  paths for the markers show that it is possible to obtain conditions similar to those observed in natural ophiolites (e.g. Dilek and Whitney 1997; Pomonis *et al.* 2002; Elitok and Drüppel 2008). However, metamorphic-sole rocks (amphibolites) associated with ophiolite rocks from Oman seem to yield considerably larger metamorphic-pressure estimates (e.g. Cowan *et al.* 2014). Although our investigated model scenario is different than that for Oman, thermo-mechanical models that reproduce the observed conditions as in Oman ophiolite have shown that high (>1GPa) metamorphic pressures are possible if the metamorphic pressure is twice the lithostatic (Duretz *et al.* 2016, their Fig.1). From a mechanical point of view this is possible if a significant tectonic overpressure occurs at the early stage of the obduction/subduction process (e.g. Moulas *et al.* 2019; 2021). However, our study shows that, in our modelled scenarios, the amount of tectonic overpressure is not significant. Further investigations considering in detail the effects of rheology and the full 3D geometry may show a greater variability on the conditions experienced by the metamorphic rocks adjacent to ophiolites. In any case, our numerical model shows the mechanically feasible conditions and the associated values of pressure and temperature in the vicinity of ophiolite rocks. Our model

cannot predict whether a metamorphic sole will actually form since the effects of metamorphic-reaction kinetics are not considered.

## 2.5 Conclusion

We presented a number of models for ophiolite emplacement. As a reference, we considered the case of the convergence of two continental regions separated by a relatively small oceanic basin, as it is commonly envisioned for the small basins in the Tethyan region. Our models considered a realistic buoyancy force since the density used was obtained by equilibrium phase diagram sections. Model results revealed that the initial asymmetric configuration and the small size of the oceanic basin are critical factors for the successful ophiolite emplacement. In particular, the small size of the ocean explains the small age difference reported from geochronology studies for the Tethyan region. Furthermore, our models required the consideration of relatively strong lower continental crust under moderate to high convergence velocities for successful ophiolite obduction. Given the aforementioned considerations, our reference model was able to produce commonly-observed amphibolite-facies conditions in the rocks constituting the metamorphic sole. Finally, it is noted that, with the help of accretionary uplift, the ophiolite and the rocks from the metamorphic sole are finally emplaced in the upper crust of the overriding plate.

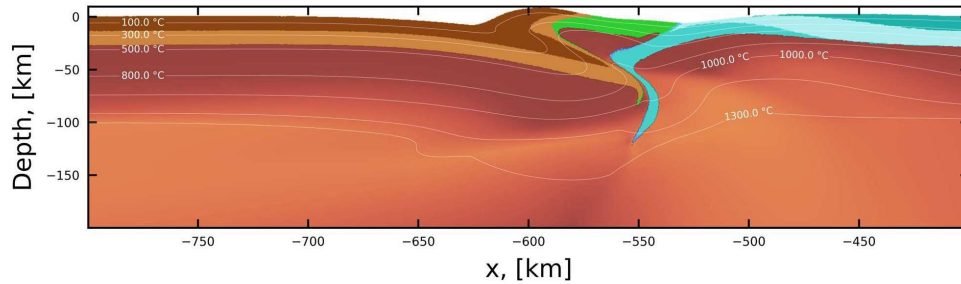
## 2.6 Acknowledgements

I.I. and E.M. would like to acknowledge the Johannes-Gutenberg University of Mainz for financial support. Boris Kaus is acknowledged for providing access to MOGON-II, without which our study would have not been possible. Authors thank LaMEM development team (B. Kaus, A. Popov, A. Spang and others) for software usage advices. Authors are grateful to L. Le Pourhiet, D. Kostopoulos, P. Pomonis and T. Reischmann for insightful discussions. Many thanks to A. Piccolo for providing visualisation script. We acknowledge two anonymous reviewers for their constructive comments and the editor, Prof. Yildirim Dilek for handling our manuscript.

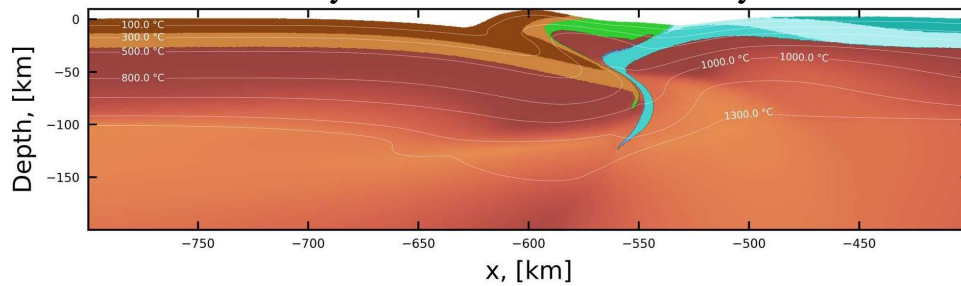
## 2.7 Supplementary

In this file we present 5 supplementary figures (Figs. S1-S5) that are mentioned in the main text.

Reference model. Bottom boundary: 670 km. Time = 5.047 Myrs



Model with no-slip condition at the bottom of the model. Bottom boundary: 670 km. Time = 5.047 Myrs



Model with cropped bottom boundary. Bottom boundary: 400 km. Time = 5.047 Myrs

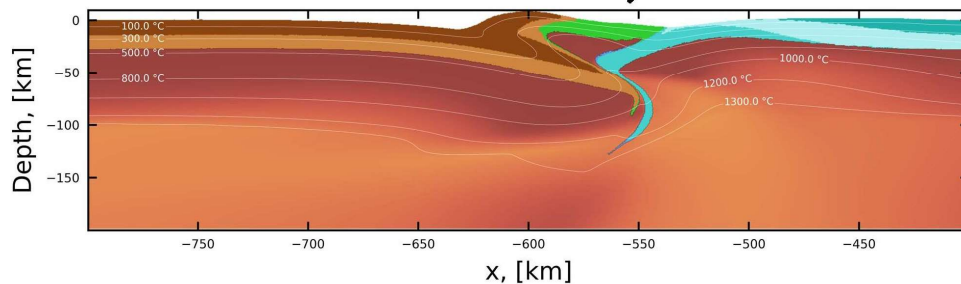


*Figure S 1 Reference model configuration at ca 5Myrs. The three model results have been calculated using different bottom boundary conditions. The top panel shows the reference model (using free-slip bottom boundary conditions). The bottom boundary is set at 670km. The middle panel shows the same model configuration but with no slip at the bottom boundary (at 670km). The lower panel shows the same model configuration but with the bottom boundary placed 400km depth (using free-slip boundary conditions).*

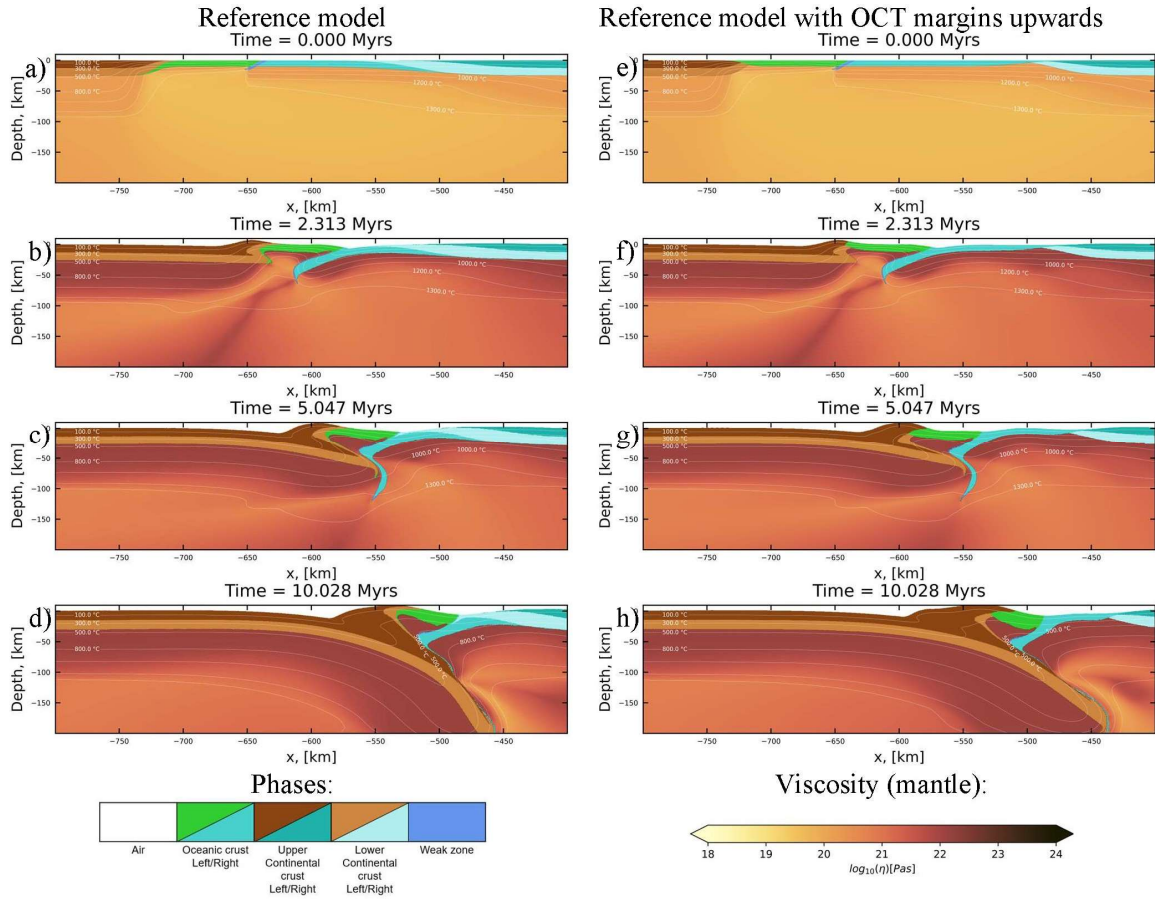


Figure S 2 Figure that shows the influence of the initial oceanic-crust/continental-crust contact on the model results. (a-d) Reference model Figure 2.4(e-h) Same conditions as in reference model but with the oceanic crust emplaced initially on top of the continental margin.

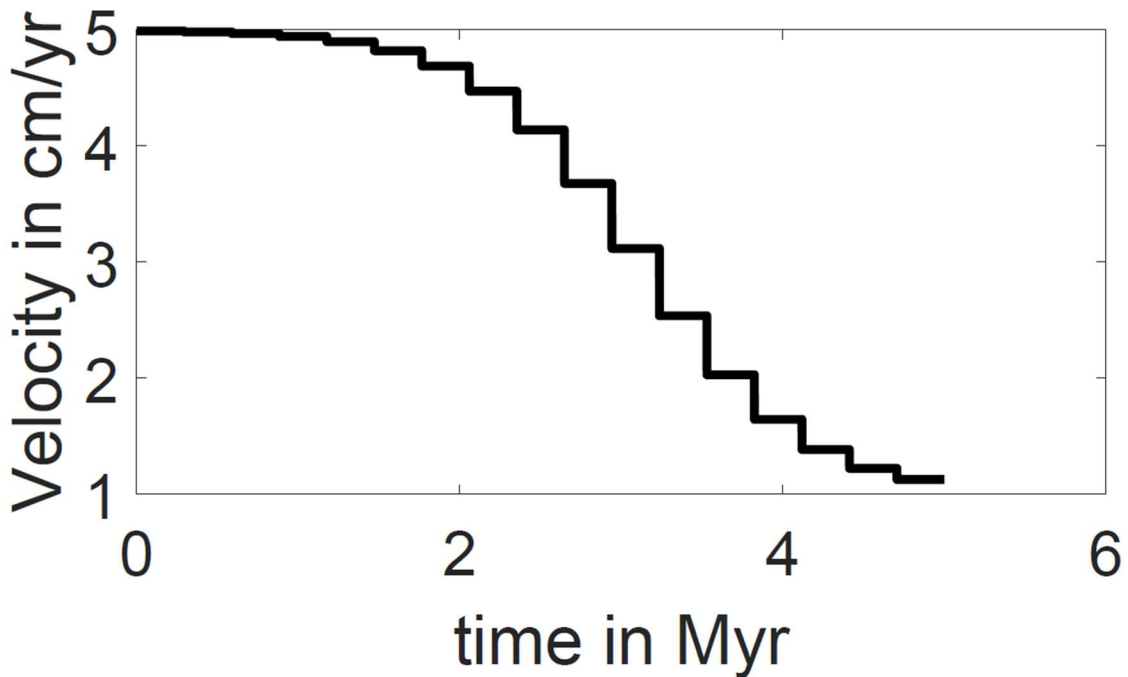


Figure S 3 Non-constant converging velocity used to calculate Figure 2.8 of the main text.



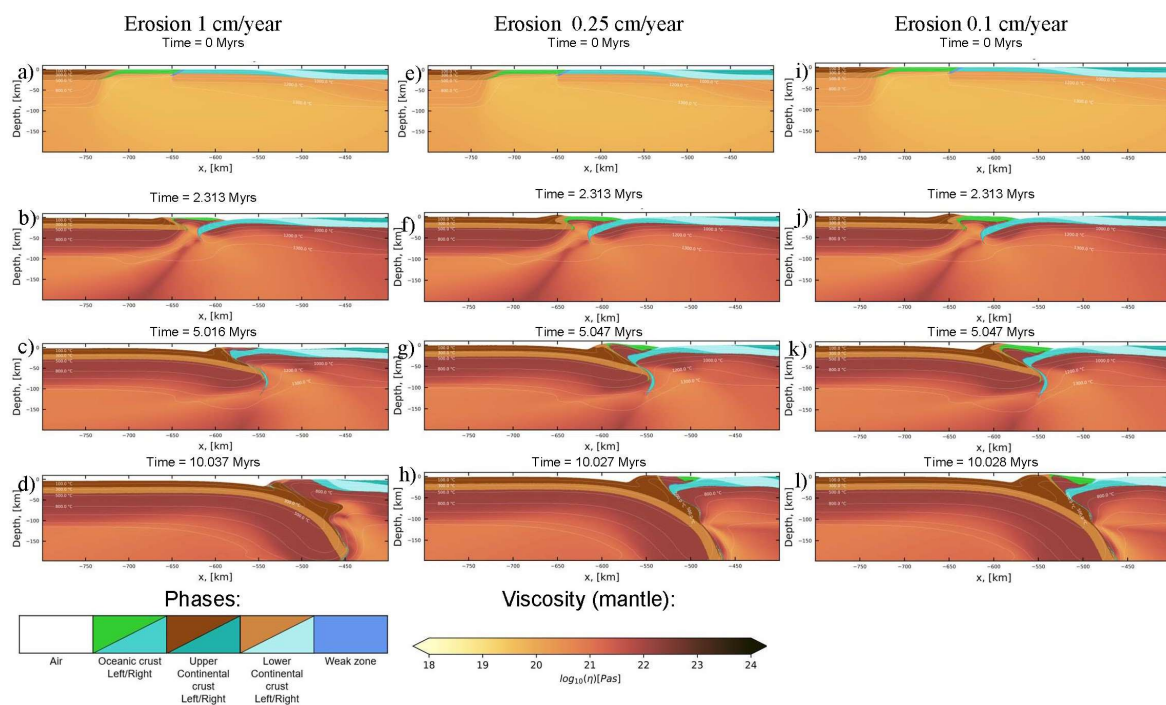


Figure S 4 Figure that shows the influence of variable erosion rates in the reference model configuration. The converging velocity is assumed to be constant and every parameter is as in the reference model. (a-d) With constant erosion of 1cm/yr, (e-h) with constant erosion of 0.25 cm/yr, (i-l) with constant erosion of 0.1 cm/yr.

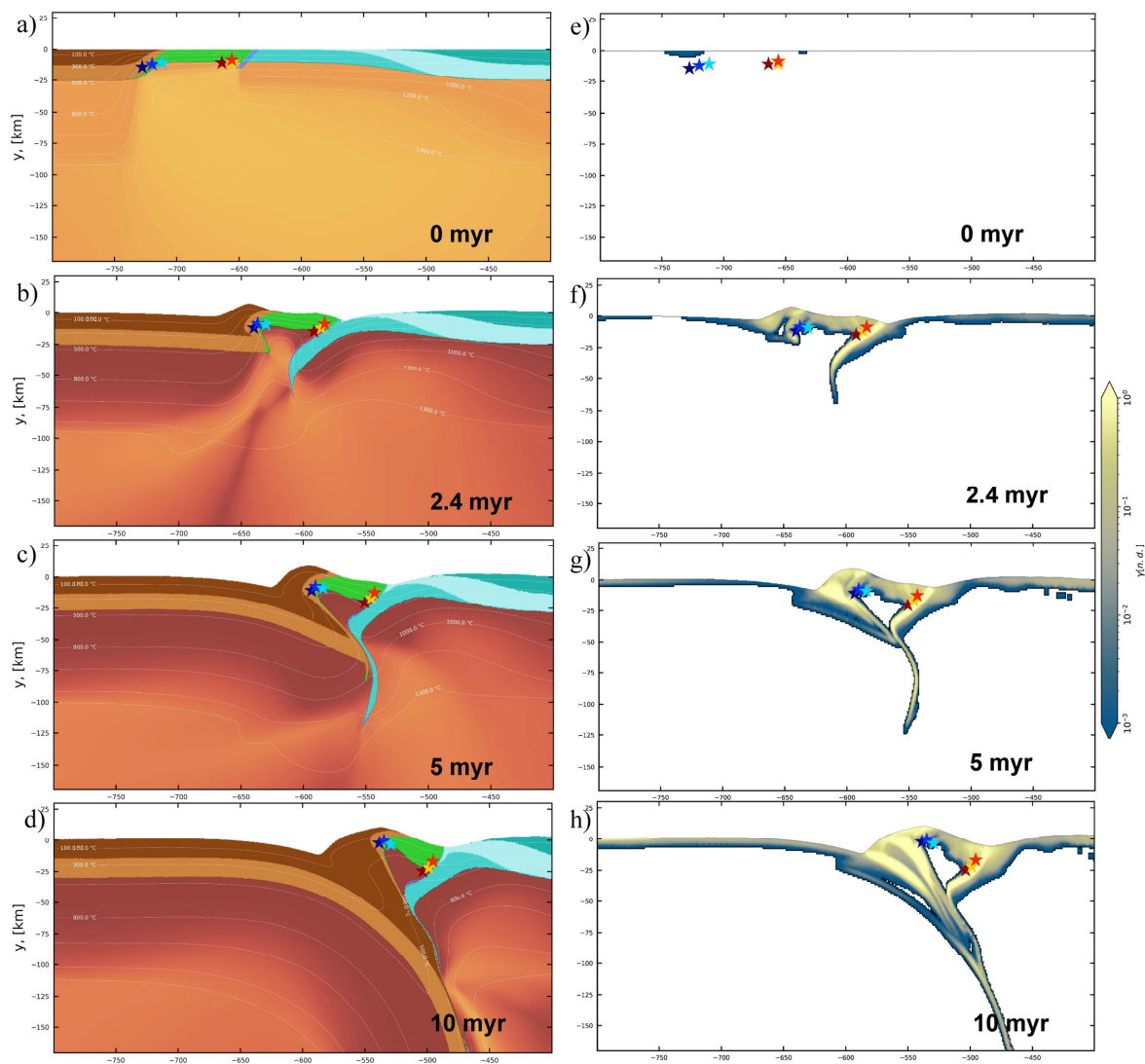


Figure S 5 Distribution of plastic finite strain in the reference model. (a-d) As in Figure 2.9 (e-h) Plastic strain field of the same model. Note that values of plastic strain larger than 1 (100%) are not distinguished (i.e. the colorscale is saturated).

## 2.8 References

Agard, P., Soret, M., Bonnet, G., Ninkabou, D., Plunder, A., Prigent, C. and Yamato, P. 2023. Subduction and Obduction Processes: The Fate of Oceanic Lithosphere Revealed by Blueschists, Eclogites, and Ophiolites. *In*: Catlos, E. J. and Çemen, İ. (eds) *Geophysical Monograph Series*. 21–45., <https://doi.org/10.1002/9781119773856.ch2>.

Beaumont, C. and Quinlan, G. 1994. A geodynamic framework for interpreting crustal-scale seismic-reflectivity patterns in compressional orogens. *Geophysical Journal International*, **116**, 754–783, <https://doi.org/10.1111/j.1365-246X.1994.tb03295.x>.

Bessat, A., Duretz, T., Hetényi, G., Pilet, S. and Schmalholz, S.M. 2020. Stress and deformation mechanisms at a subduction zone: insights from 2-D thermomechanical numerical modelling. *Geophysical Journal International*, **221**, 1605–1625, <https://doi.org/10.1093/gji/ggaa092>.

Biari, Y., Klingelhoefer, F., et al. 2021. Structure and evolution of the Atlantic passive margins: A review of existing rifting models from wide-angle seismic data and kinematic reconstruction. *Marine and Petroleum Geology*, **126**, 104898, <https://doi.org/10.1016/j.marpetgeo.2021.104898>.

Brongniart, A. 1813. Essai d'une classification minéralogique des roches mélangées.-J. des Mines.

Candioti, L.G., Duretz, T., Moulas, E. and Schmalholz, S.M. 2021. Buoyancy versus shear forces in building orogenic wedges. *Solid Earth*, **12**, 1749–1775, <https://doi.org/10.5194/se-12-1749-2021>.

Chemenda, A.I., Mattauer, M. and Bokun, A.N. 1996. Continental subduction and a mechanism for exhumation of high-pressure metamorphic rocks: new modelling and field data from Oman. *Earth and Planetary Science Letters*, **143**, 173–182, [https://doi.org/10.1016/0012-821X\(96\)00123-9](https://doi.org/10.1016/0012-821X(96)00123-9).

Cloos, M. 1993. *Lithospheric Buoyancy and Collisional Orogenesis: Subduction of Oceanic Plateaus, Continental Margins, Island Arcs, Spreading Ridges, and Seamounts*.

Coleman, R.G. 1971. Plate tectonic emplacement of upper mantle peridotites along continental edges. *Journal of Geophysical Research*, **76**, 1212–1222, <https://doi.org/10.1029/JB076i005p01212>.

Connolly, J.A.D. 2005. Computation of phase equilibria by linear programming: A tool for geodynamic modeling and its application to subduction zone decarbonation. *Earth and Planetary Science Letters*, **236**, 524–541, <https://doi.org/10.1016/j.epsl.2005.04.033>.

Connolly, J.A.D. 2009. The geodynamic equation of state: What and how: GEODYNAMIC EQUATION OF STATE-WHAT AND HOW. *Geochemistry, Geophysics, Geosystems*, **10**, n/a-n/a, <https://doi.org/10.1029/2009GC002540>.

Cowan, R.J., Searle, M.P. and Waters, D.J. 2014. Structure of the metamorphic sole to the Oman Ophiolite, Sumeini Window and Wadi Tayyin: implications for ophiolite obduction processes. *Geological Society, London, Special Publications*, **392**, 155–175, <https://doi.org/10.1144/SP392.8>.

Currie, C.A., Huismans, R.S. and Beaumont, C. 2008. Thinning of continental backarc lithosphere by flow-induced gravitational instability. *Earth and Planetary Science Letters*, **269**, 436–447, <https://doi.org/10.1016/j.epsl.2008.02.037>.

Dewey, J.F. 1976. Ophiolite obduction. *Tectonophysics*, **31**, 93–120, [https://doi.org/10.1016/0040-1951\(76\)90169-4](https://doi.org/10.1016/0040-1951(76)90169-4).

- Dilek, Y. and Furnes, H. 2011. Ophiolite genesis and global tectonics: Geochemical and tectonic fingerprinting of ancient oceanic lithosphere. *Bulletin of the Geological Society of America*, **123**, 387–411, <https://doi.org/10.1130/B30446.1>.
- Dilek, Y. and Whitney, D.L. 1997. Counterclockwise P-T-t trajectory from the metamorphic sole of a Neo-Tethyan ophiolite (Turkey). *Tectonophysics*, **280**, 295–310, [https://doi.org/10.1016/S0040-1951\(97\)00038-3](https://doi.org/10.1016/S0040-1951(97)00038-3).
- Dilek, Y., Furnes, H. and Shallo, M. 2007. Suprasubduction zone ophiolite formation along the periphery of Mesozoic Gondwana. *Gondwana Research*, **11**, 453–475, <https://doi.org/10.1016/j.gr.2007.01.005>.
- Dilek, Y., Furnes, H. and Shallo, M. 2008. Geochemistry of the Jurassic Mirdita Ophiolite (Albania) and the MORB to SSZ evolution of a marginal basin oceanic crust. *Lithos*, **100**, 174–209, <https://doi.org/10.1016/j.lithos.2007.06.026>.
- Dimo-Lahitte, A., Monié, P. and Vergély, P. 2001. Metamorphic soles from the Albanian ophiolites: Petrology,  $^{40}\text{Ar}/^{39}\text{Ar}$  geochronology, and geodynamic evolution. *Tectonics*, **20**, 78–96, <https://doi.org/10.1029/2000TC900024>.
- Duretz, T., Agard, P., Yamato, P., Ducassou, C., Burov, E.B. and Gerya, T.V. 2016. Thermo-mechanical modeling of the obduction process based on the Oman Ophiolite case. *Gondwana Research*, **32**, 1–10, <https://doi.org/10.1016/j.gr.2015.02.002>.
- Edwards, S.J., Schellart, W.P. and Duarte, J.C. 2015. Geodynamic models of continental subduction and obduction of overriding plate forearc oceanic lithosphere on top of continental crust. *Tectonics*, **34**, 1494–1515, <https://doi.org/10.1002/2015TC003884>.
- Elitok, Ö. and Drüppel, K. 2008. Geochemistry and tectonic significance of metamorphic sole rocks beneath the Beyşehir–Hoyran ophiolite (SW-Turkey). *Lithos*, **100**, 322–353, <https://doi.org/10.1016/j.lithos.2007.06.022>.
- El-Shazly, A.K. and Coleman, R.G. 1990. Metamorphism in the Oman Mountains in relation to the Semail ophiolite emplacement. *Geological Society, London, Special Publications*, **49**, 473–493, <https://doi.org/10.1144/GSL.SP.1992.049.01.30>.
- Faul, U.H. and Jackson, I. 2007. Diffusion creep of dry, melt-free olivine. *Journal of Geophysical Research: Solid Earth*, **112**, <https://doi.org/10.1029/2006JB004586>.
- Faul, U.H., Fitz Gerald, J.D., Farla, R.J.M., Ahlefeldt, R. and Jackson, I. 2011. Dislocation creep of fine-grained olivine. *Journal of Geophysical Research: Solid Earth*, **116**, <https://doi.org/10.1029/2009JB007174>.
- Garfunkel, Z. 2006. Neotethyan ophiolites: Formation and obduction within the life cycle of the host basins. *Geological Society Special Publication*, **260**, 301–326, <https://doi.org/10.1144/GSL.SP.2006.260.01.13>.
- Gass, I.G. 1968. Is the Troodos Massif of Cyprus a Fragment of Mesozoic Ocean Floor? *Nature*, **220**, 39–42, <https://doi.org/10.1038/220039a0>.
- Ghikas, C., Dilek, Y. and Rassios, A.E. 2010. Structure and tectonics of subophiolitic mélanges in the western Hellenides (Greece): implications for ophiolite emplacement tectonics. *International Geology Review*, **52**, 423–453, <https://doi.org/10.1080/00206810902951106>.

Hässig, M., Duretz, T., Rolland, Y. and Sosson, M. 2016a. Obduction of old oceanic lithosphere due to reheating and plate reorganization : Insights from numerical modelling and the NE Anatolia – Lesser Caucasus case example. *Journal of Geodynamics*, **96**, 35–49, <https://doi.org/10.1016/j.jog.2016.02.007>.

Hässig, M., Rolland, Y., Duretz, T. and Sosson, M. 2016b. Obduction triggered by regional heating during plate reorganization. *Terra Nova*, **28**, 76–82, <https://doi.org/10.1111/ter.12193>.

Jones, G. and Robertson, A.H.F. 1991. Tectono-stratigraphy and evolution of the Mesozoic Pindos ophiolite and related units, northwestern Greece. *Journal of the Geological Society*, **148**, 267–288, <https://doi.org/10.1144/gsjgs.148.2.0267>.

Karato, S. and Jung, H. 2003. Effects of pressure on high-temperature dislocation creep in olivine. 401–414, <https://doi.org/10.1080/0141861021000025829>.

Kaus, B.J.P., Popov, A.A., Baumann, T.S., Pusok, A.E., Bauville, A., Fernandez, N. and Collignon, M. 2016. Forward and Inverse Modelling of Lithospheric Deformation on Geological Timescales. *NIC Series*, **48**, 978–3.

Kober, L. 1952. *Leitlinien Der Tektonik Jugoslawiens*.

Liati, A., Gebauer, D. and Fanning, C.M. 2004. The age of ophiolitic rocks of the Hellenides (Vourinos, Pindos, Crete): first U–Pb ion microprobe (SHRIMP) zircon ages. *Chemical Geology*, **207**, 171–188, <https://doi.org/10.1016/j.chemgeo.2004.02.010>.

Mackwell, S.J., Zimmerman, M.E. and Kohlstedt, D.L. 1998. High-temperature deformation of dry diabase with application to tectonics on Venus. *Journal of Geophysical Research: Solid Earth*, **103**, 975–984, <https://doi.org/10.1029/97JB02671>.

Maffione, M. and van Hinsbergen, D.J.J. 2018. Reconstructing Plate Boundaries in the Jurassic Neo-Tethys From the East and West Vardar Ophiolites (Greece and Serbia). *Tectonics*, **37**, 858–887, <https://doi.org/10.1002/2017TC004790>.

Molnar, P. and Stock, J.M. 2009. Slowing of India’s convergence with Eurasia since 20 Ma and its implications for Tibetan mantle dynamics: INDIA-EURASIA CONVERGENCE RATE CHANGE. *Tectonics*, **28**, n/a-n/a, <https://doi.org/10.1029/2008TC002271>.

Moores, E.M. 1982. origin and emplacement of ophiolites. *Reviews of Geophysics*, **20**, 735, <https://doi.org/10.1029/RG020i004p00735>.

Moores, E.M. and Vine, F.J. 1971. The Troodos Massif, Cyprus and other ophiolites as oceanic crust: evaluation and implications. *Philosophical Transactions of the Royal Society of London. Series A, Mathematical and Physical Sciences*, **268**, 443–467, <https://doi.org/10.1098/rsta.1971.0006>.

Moulas, E., Schmalholz, S.M., Podladchikov, Y., Tajčmanová, L., Kostopoulos, D. and Baumgartner, L. 2019. Relation between mean stress, thermodynamic, and lithostatic pressure. *Journal of Metamorphic Geology*, **37**, 1–14, <https://doi.org/10.1111/jmg.12446>.

Moulas, E., Brandon, M.T., Vaughan Hammon, J.D. and Schmalholz, S.M. 2021. On backflow associated with oceanic and continental subduction. *Geophysical Journal International*, **227**, 576–590, <https://doi.org/10.1093/gji/ggab246>.

- Mueller, S. and Phillips, R.J. 1991. On The initiation of subduction. *Journal of Geophysical Research*, **96**, 651, <https://doi.org/10.1029/90JB02237>.
- Pomonis, P., Tsikouras, B. and Hatzipanagiotou, K. 2002. Origin, evolution and radiometric dating of subophiolitic metamorphic rocks from the Koziakas ophiolite (W. Thessaly, Greece). *Neues Jahrbuch für Mineralogie - Abhandlungen*, **177**, 255–276, <https://doi.org/10.1127/0077-7757/2002/0177-0255>.
- Porkoláb, K., Yamato, P. and Auzemery, A. 2020. Extrusion of subducted crust explains the emplacement of far-travelled ophiolites. 1–20.
- Porkoláb, K., Duretz, T., Yamato, P., Auzemery, A. and Willingshofer, E. 2021. Extrusion of subducted crust explains the emplacement of far-travelled ophiolites. *Nature Communications*, **12**, 1499, <https://doi.org/10.1038/s41467-021-21866-1>.
- Raleigh, C.B. and Paterson, M.S. 1965. Experimental deformation of serpentinite and its tectonic implications. *Journal of Geophysical Research (1896-1977)*, **70**, 3965–3985, <https://doi.org/10.1029/JZ070i016p03965>.
- Ranalli, G. 1995. *Rheology of the Earth / Giorgio Ranalli.*, 2nd ed.
- Rassios, A.E. and Dilek, Y. 2009. Rotational deformation in the Jurassic Mesohellenic ophiolites, Greece, and its tectonic significance. *Lithos*, **108**, 207–223, <https://doi.org/10.1016/j.lithos.2008.09.005>.
- Robertson, A.H.F. 2012. Late Palaeozoic–Cenozoic tectonic development of Greece and Albania in the context of alternative reconstructions of Tethys in the Eastern Mediterranean region. *International Geology Review*, **54**, 373–454, <https://doi.org/10.1080/00206814.2010.543791>.
- Robertson, A.H.F., Clift, P.D., Degnan, P.J. and Jones, G. 1991. Palaeogeographic and palaeotectonic evolution of the Eastern Mediterranean Neotethys. *Palaeogeography, Palaeoclimatology, Palaeoecology*, **87**, 289–343, [https://doi.org/10.1016/0031-0182\(91\)90140-M](https://doi.org/10.1016/0031-0182(91)90140-M).
- Rybacki, E. and Dresen, G. 2000. Dislocation and diffusion creep of synthetic anorthite aggregates. *Journal of Geophysical Research: Solid Earth*, **105**, 26017–26036, <https://doi.org/10.1029/2000JB900223>.
- Shervais, J.W. 2001. Birth, death, and resurrection: The life cycle of suprasubduction zone ophiolites: SUPRASUBDUCTION ZONE OPHIOLITES. *Geochemistry, Geophysics, Geosystems*, **2**, n/a-n/a, <https://doi.org/10.1029/2000GC000080>.
- Stampfli, G.M. and Borel, G.D. 2002. A plate tectonic model for the Paleozoic and Mesozoic constrained by dynamic plate boundaries and restored synthetic oceanic isochrons. *Earth and Planetary Science Letters*, **196**, 17–33, [https://doi.org/10.1016/S0012-821X\(01\)00588-X](https://doi.org/10.1016/S0012-821X(01)00588-X).
- Stüwe, K. 2007. *Geodynamics of the Lithosphere: An Introduction*, 2nd ed.
- Suess, E. 1909. *Das Antlitz Der Erde*.
- Turcotte, D.L. and Oxburgh, E.R. 1967. Finite amplitude convective cells and continental drift. *Journal of Fluid Mechanics*, **28**, 29–42, <https://doi.org/10.1017/S0022112067001880>.

---

Wakabayashi, J. and Dilek, Y. 2003. What constitutes 'emplacement' of an ophiolite?: Mechanisms and relationship to subduction initiation and formation of metamorphic soles. *Geological Society, London, Special Publications*, **218**, 427–447, <https://doi.org/10.1144/GSL.SP.2003.218.01.22>.

---

## Chapter 3

# A thermo-mechanical model of the thermal evolution and incorporation of the metamorphic sole in the Oman ophiolite

### **Abstract**

Ophiolites are remnants of oceanic crust and mantle, now typically found within continental mountain ranges. Particularly in areas once part of the Tethys Ocean, ophiolites are often accompanied by narrow strips of metamorphic rocks, commonly referred to as metamorphic soles. These rocks exhibit peak metamorphic conditions characteristic of either granulite or amphibolite facies. Geochronological studies of Tethyan ophiolites indicate that the development of these metamorphic soles occurred almost simultaneously with the crystallization of the ophiolite's crustal sequence. Geological evidence also suggests that the metamorphism of the sole rocks took place concurrently with deformation, likely at the same time as the ophiolite's obduction. In our research, we explore the metamorphic effects of shearing in an ophiolite sequence overlying a crustal sequence. Our findings reveal that a strong crustal lithology can produce additional heat through the dissipation of mechanical energy, which can explain the high temperatures found in metamorphic-sole rocks. In addition, heating of the footwall rocks eventually leads to the migration of the active shear zone from the mantle sequence into the upper crustal domain. This migration is responsible for the metamorphic sole incorporation at the base of the ophiolite. Finally, we demonstrate that stopping the shearing process rapidly cools these rocks, corresponding with the findings from thermochronological studies from Oman ophiolite.



### 3.1 Introduction

Ophiolites are considered to be the remnants of ancient oceanic lithosphere and can now be found on top of continental regions (e.g. Frisch et al., 2011). In particular, the remnants of the Tethys Ocean can now be found all across the Alpine orogen, extending from the Alps to the West and reaching until Iran and Oman to the East (Figure 3.1; Garfunkel, 2006; Dilek et al., 2007). Since the early stages of the development of the theory of plate tectonics, the study of ophiolite belts posed significant challenges regarding the mechanisms and the processes that operate during their emplacement or obduction (Dewey 1976; Moores 1982). This is because the negative buoyancy of oceanic lithosphere is a dominant force in our planet (Forsyth and Uyeda 1975), and it is quite natural that, in active margins, the cold and dense oceanic lithosphere tends to get subducted (Cloos 1993b). The subduction of the oceanic lithosphere is a process that will erase most of the evidence documenting the former presence of the ocean (Dewey 1976). Thus, despite their scarcity, ophiolites can help us unravel the processes related to oceanic subduction and mountain building.

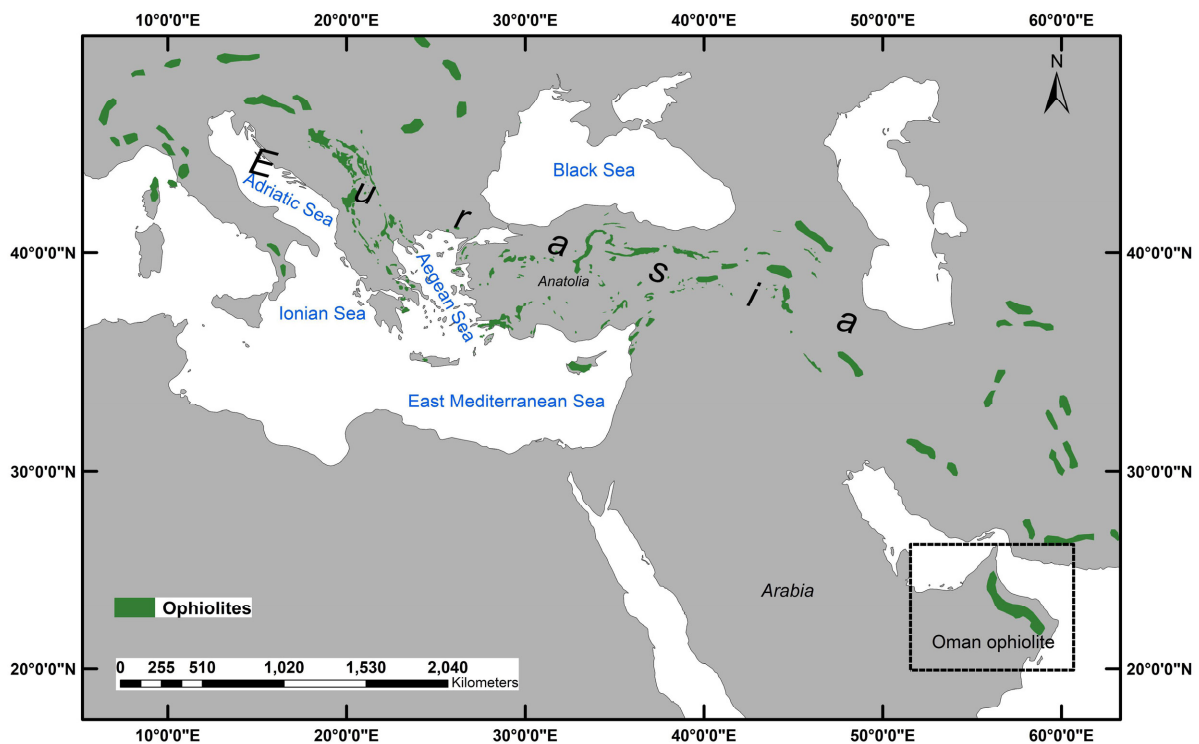


Figure 3.1 Simplified map showing the distribution of ophiolites in the Mediterranean region. The Oman ophiolite is shown in the lower, right part of the map. Data mostly after Dilek et al. (2007; and references therein).

The ideal stratigraphic sequences of ophiolites involve (from top to bottom) oceanic sediments, pillow lavas, sheeted dikes, gabbros and ultramafic rocks (Anonymous 1972b). In many cases, crustal metamorphic rocks of mafic or pelitic composition can also be found below the ophiolite complexes (Williams and Smyth 1973; Whitechurch and Parrot 1974, 1978; Woodcock and Robertson 1977; Malpas 1979; Jamieson 1980). These rocks are commonly known as metamorphic soles or aureoles (Williams and Smyth 1973; Malpas 1979) and are characterized by high-temperature metamorphism in a narrow region (Williams and Smyth 1973; Wakabayashi and Dilek 2003b). The metamorphic conditions that are commonly reported for the soles are amphibolite to granulite facies (e.g. Jamieson, 1980; El-Shazly and Coleman, 1990; Pomonis *et al.*, 2002; Myhill, 2011), and in particular they range between 600-800°C and 0.5-1.0 GPa. The high-grade metamorphic rocks are also thought to have formed inverted metamorphic gradients where the temperature decreases with structural depth (Spray 1984). In addition, the older isotopic ages from the metamorphic sole rocks are almost indistinguishable from the youngest “magmatic” ages of the ophiolite (Spray and Roddick 1980; Hacker *et al.* 1996; Liati *et al.* 2004b; Rioux *et al.* 2016; Guilmette *et al.* 2018; Garber *et al.* 2020). Such observations lead previous authors to conclude that both shear heating and the heat from the young (and hot) mantle lithosphere contributed to the formation of these rocks (Williams and Smyth 1973; Woodcock and Robertson 1977; Malpas 1979).

Extensive thermochronological analysis performed on metamorphic-sole rocks from Oman has revealed that the cooling of hornblende, amphibole and biotite separates from the sole rocks occurred very fast (Hacker *et al.* 1996). These cooling rates are variable and range between 100-400 °C per million years for the temperature range of 500-800 °C (Hacker *et al.* 1996). Such high cooling rates are difficult to be explained using regional exhumation models and suggest the presence of small, local heat sources (Stüwe and Ehlers 1998; Burg and Moulas 2022). Thus, the consideration of heat production during the irreversible deformation of rocks may be the reason for the local heat production adjacent to shear zones.

To test the feasibility of shear heating models, we have built upon previous thermomechanical models that simultaneously solve for the stresses and the temperature in a region deforming by simple shear (Yuen *et al.* 1978; Fleitout and Froidevaux 1980; Kiss *et al.* 2019). Our model considers the initial emplacement of a hot, mantle rock atop a relatively colder oceanic crustal rock (Figure 3.2). More details for the development of the thermomechanical model are given in section 2 (Methods). The initial geothermal gradient used in our model is consistent with the emplacement of a young (and hot) mantle rock on cold crustal lithologies following Hacker *et al.*, (1996). In agreement with previous studies (Hacker

1990), our results show that the shear zone progressively migrates from the lower parts of the mantle region, towards the upper parts of the crustal section. This is particularly of interest since it provides a natural mechanism for the incorporation of the metamorphic sole, even if the initial thrust zone was at the lithological boundary. In addition, our results predict that the peak temperature experienced by the sole rocks is a function of the boundary velocity and it is within the range of the observed values for Oman (El-Shazly and Coleman 1990; Garber *et al.* 2020) assuming realistic shearing velocities (1-10 cm). Considering this velocity range, a simple scaling relationship can be fit based on the systematic results of our study. Last but not least, our model is able to predict a cooling history for the metamorphic-sole rocks that is in excellent agreement with the available thermochronology data from Oman (Hacker *et al.* 1996).

## 3.2 Methods

We begin by considering the deformation along a vertical section following the approach of Yuen *et al.* (1978) that is described in detail in Burg and Moulas (2022; their Appendix 4). We consider that  $x_1$  is the direction parallel to an initially horizontal shearing plane (and the shearing direction) and  $x_3$  is the direction normal to the shear zone (vertical orientation in our case; Figure 3.2). Note that the  $x_3$  direction is pointing upwards whereas depth ( $z$ ) is pointing downwards (Figure 3.2). For this particular orientation of the shear zone and model assumptions, conservation of momentum in the vertical direction reduces to the lithostatic formula (Burg and Moulas 2022). Therefore, we will not consider pressure effects further since the pressure evolution is a function of the shear-zone orientation (Moulas *et al.* 2014, 2022) and its investigation is beyond the scope of this study. Symbols and material constants used in this part are given in Table 3.1.

*Table 3.1 Symbols and units of quantities used in this study. Apart from the values explicitly mentioned in the text, a reference value for heat capacity of  $1050 \text{ J kg}^{-1} \text{ K}^{-1}$  was used for both lithologies. With respect to the density, the values of  $3400$  and  $3000 \text{ kg m}^{-3}$  were used for the upper and the lower plate respectively. Finally, the thermal conductivity of the upper plate was taken as  $3 \text{ W m}^{-1} \text{ K}^{-1}$  whereas the thermal conductivity of the lower plate was  $2.4 \text{ W m}^{-1} \text{ K}^{-1}$ .*

Parameter	Symbol	Units
Temperature	$T$	$^{\circ}\text{C}$ or $\text{K}$
Deviatoric stress tensor	$\tau_{ij}$	$\text{Pa}$
Velocity	$v_i$	$\text{m s}^{-1}$
Density	$\rho$	$\text{kg m}^{-3}$

<b>Spatial coordinate (measured from bottom)</b>	$x_i$	$m$
<b>Depth (measured from top)</b>	$z$	$m$
<b>Total length of model</b>	$L$	$m$
<b>Peierls stress</b>	$\sigma_P$	$Pa$
<b>Specific heat</b>	$C_p$	$J\ kg^{-1}\ K^{-1}$
<b>Thermal conductivity</b>	$\lambda$	$J\ m^{-1}\ s^{-1}\ K^{-1}$
<b>Thermal diffusivity</b>	$\kappa$	$m^2\ s^{-1}$
<b>Material constant (used in viscous flow law)</b>	$A_0$	$Pa^{-n}\ s^{-1}$
<b>Stress exponent (used in viscous flow law)</b>	$n$	–
<b>Activation energy (used in viscous flow law)</b>	$Q$	$J\ mol^{-1}$
<b>Gas constant</b>	$R$	$J\ mol^{-1}\ K^{-1}$

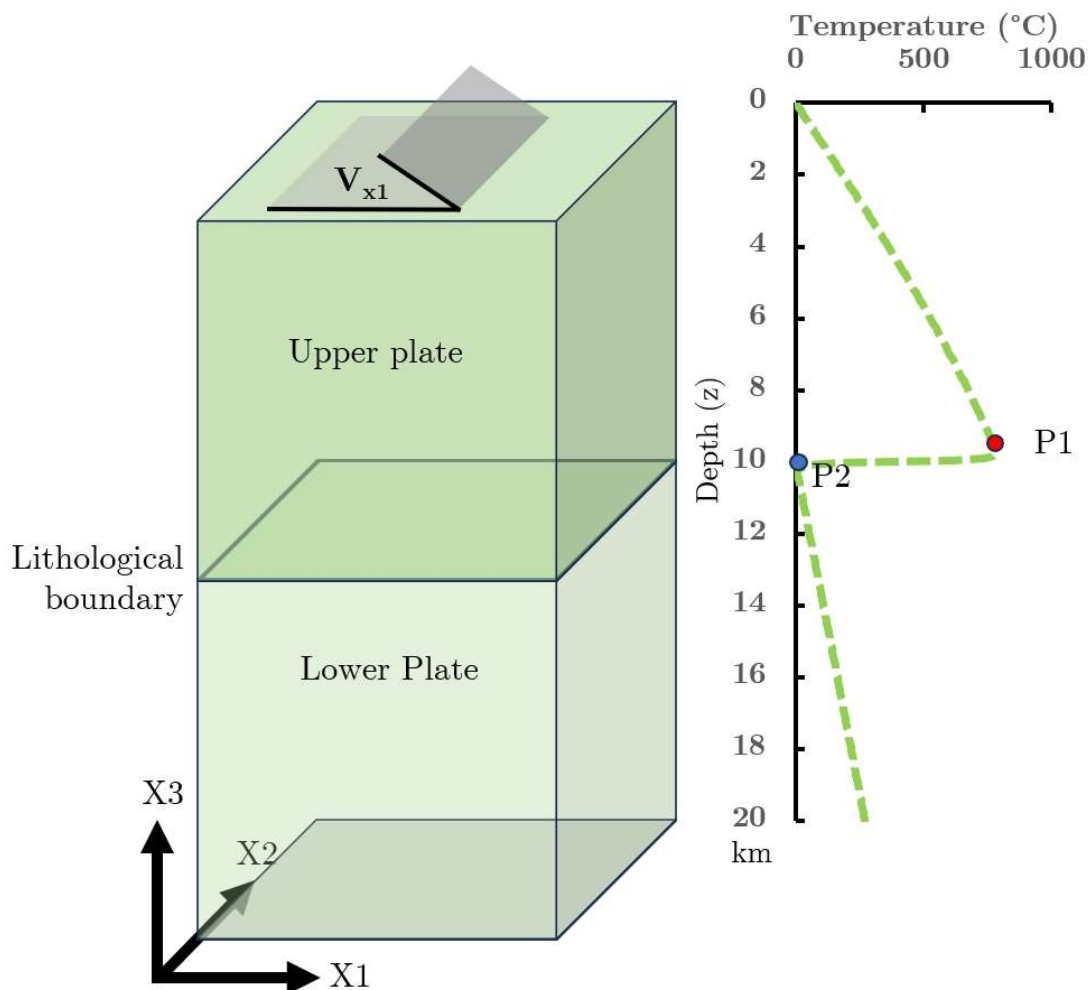


Figure 3.2 Thermomechanical model configuration. A right-hand coordinate system is also shown ( $x_1, x_2, x_3$ ). It is assumed that the upper plate has mantle rheology whereas the lower plate has a strong crustal rheology. The initial temperature distribution is shown on the plot on the right as a function of depth ( $z$ ). Note that the vertical coordinate and the depth are related via  $z = L - x_3$ , where  $L$  is the total length of the model.

Due to problem's symmetry, all derivatives in the  $x_1$  and  $x_2$  direction vanish. We assume that our material is incompressible and, therefore, the continuity equation reduces to the following form:

$$\frac{\partial v_3}{\partial x_3} = 0 \quad (3.12)$$

where  $v_3$  is the velocity in the  $x_3$  (vertical) direction. The flow is assumed to be slow (inertial terms are negligible), this reduces the momentum conservation along  $x_1$  (parallel to the shearing plane) as follows (Fleitout and Froidevaux 1980, p. 160):

$$\frac{\partial \tau_{13}}{\partial x_3} = 0 \quad (3.2)$$

where  $\tau_{13}$ , is the shear stress within the shear zone. Equation (Chapter 3:2) implies that  $\tau_{13}$  remains constant in the shear zone during deformation. Note however that  $\tau_{13}$  is constant in space, but not in time. Under these assumptions, the temperature in the shear zone can be given as follows:

$$\rho C_p \frac{\partial T}{\partial t} = \frac{\partial}{\partial x_3} \left( \lambda \frac{\partial T}{\partial x_3} \right) + 2\tau_{13} \dot{\epsilon}_{13} \quad (\text{Chapter 3:.3})$$

where, in our case,  $\dot{\epsilon}_{13}$  is given by equation (3.4):

$$\dot{\epsilon}_{13} = \frac{1}{2} \left( \frac{\partial v_3}{\partial x_1} + \frac{\partial v_1}{\partial x_3} \right) = \frac{1}{2} \frac{\partial v_1}{\partial x_3} \quad (\text{Chapter 3:.4})$$

At this point, we can integrate the previous form with respect to  $x_3$  to obtain:

$$\int_{x_3=0}^{x_3=L'} \dot{\epsilon}_{13} dx_3 + \int_{x_3=L'}^{x_3=L} \dot{\epsilon}_{13} dx_3 = \int_{x_3=0}^{x_3=L'} \frac{1}{2} \frac{\partial v_1}{\partial x_3} dx_3 + \int_{x_3=L'}^{x_3=L} \frac{1}{2} \frac{\partial v_1}{\partial x_3} dx_3 = \frac{\Delta V}{2} \quad (\text{Chapter 3:.5})$$

where  $L'$  is the coordinate of the lithological boundary and  $L$  is the vertical coordinate of the top surface. The velocity difference between the top surface ( $x_3 = L$ ) and the bottom boundary ( $x_3 = 0$ ) of our model domain is  $\Delta V$ .

Compared to previous work (Yuen *et al.* 1978; Fleitout and Froidevaux 1980; Burg and Moulas 2022), we considered the following approximation for the non-linear, viscous rheology (creep) of rocks (Tsenn and Carter 1987, p. 5; Renshaw and Schulson 2017, p. 15):

$$\dot{\epsilon}_{13} = A_h \sinh(\beta \tau_{13})^n \exp\left(-\frac{Q}{RT}\right) \quad (\text{Chapter 3:.6})$$

where  $A$ ,  $\beta$ ,  $n$  and  $Q$  are material parameters. The previous formula places a limit on the high stress obtained in the case of fast deformation in a way consistent with exponential creep. The advantage of Eq. (Chapter 3:6) is that the transition from low-stress creep to exponential creep occurs gradually in agreement with rheology experiments (Renshaw and Schulson 2017). It can be shown that by choosing  $A_h = A/\beta^n$  and  $\beta = Q/(RT\sigma_p n)$  one recovers the power-law limit

$[\dot{\epsilon}_{13} = A\tau_{13}^n \exp(-Q/(RT))]$  at low stress conditions. Note that  $\sigma_p$  is a material parameter with units of stress for the exponential flow creep (Renshaw and Schulson 2017). In this study, we used 9 GPa as  $\sigma_p$  for both olivine and anorthite since their  $\sigma_p$  parameters are very similar (Evans and Goetze 1979; Azuma *et al.* 2014). Since we consider two different regions (Figure 3.2), we consider two flow laws of the form shown in Eq. (Chapter 3:.6) consistent with olivine rheology (above) and dry anorthite (below). The rheological parameters are taken from Ranalli, (1995; for olivine) and Rybacki and Dresen, (2004; for anorthite).

To solve the system of equations we assume an initial temperature distribution and we substitute Eq. (3.6) in Eq. (3.5). The resulting equation can be used to calculate stress ( $\tau_{13}$ ). To perform this calculation, we utilized Newton iterations. The estimated stress ( $\tau_{13}$ ) is then substituted back into Eq. (3.6) to obtain the strain rate distributions for the two domains. Both stress and strain rate distributions are then substituted into Eq. (3.3) to solve for the next temperature update. The temperature distribution is solved via the forward-Euler method using Dirichlet boundary conditions at the top (fixed temperature at 0 °C) and Neumann boundary conditions (heat flux is prescribed) at the bottom. The bottom heat flux is constrained by our initial temperature distribution that assumes that the temperature distribution in each domain follows a half-space cooling model with different “thermal ages” ( $\vartheta$ ; 2 Myr at the top and 25 Myr at the bottom). The half-space cooling is given by (e.g. Stüwe, 2007):

$$T(^{\circ}C) = 1200 \cdot \operatorname{erf}\left(\frac{z}{2\sqrt{\kappa\vartheta}}\right) \quad (\text{Chapter 3:.7})$$

where  $z$  is the original depth before the duplication and  $\kappa = \lambda/(\rho C_p)$  is the thermal diffusivity. The temperature profile that results after an instantaneous duplication has been criticised as being unphysical (Burg and Moulas 2022, p. 9). This is because it requires initially infinitely fast velocities (to achieve instantaneous duplication) and, at the same time, it neglects shear heating (that is proportional to shearing velocity). For this reason, we calculated the duplicated temperature distribution by assuming an initial temperature diffusion for a period of 1,000 years.

To be able to compare our results with the cooling-rate data, we considered that the shearing operates only for a given amount of time, after which the temperature just diffuses. In our case, we consider that the shearing lasted for 1.4 Myr. Overall, the temperatures calculated by the model were calculated until 4.4 Myr.

## 3.3 Results

We have performed several simulations to see the effects of boundary velocities and boundary conditions. However, we have chosen a specific model as our reference to provide a detailed description. The reference-model results are given in Figures 3.3-3.5.

### 3.3.1 Temperature of the shear zone

Our results show that, with the initiation of shearing, there is a region at about 8 km depth where temperature initially grows with time (Figure 3.3 a). This temperature growth is attributed to the increased dissipative heating within the upper plate. The zone of increased dissipative heating is the zone of fastest deformation (Figure 3.3 d), which generally does not stay fixed in space. As time progresses, the main zone of heat production moves towards the lower plate. This can be deduced by the fact that the temperature and the strain rate peaks are now below the lithological boundary (Figure 3.3 b,e). Since we considered that shearing lasts for only 1.4 Myr, there is no heat production beyond this point. Thus, the temperature distribution relaxes following a purely conductive behaviour (Figure 3.3 c). This is also shown by the fact that the strain rate after 1.4 Myr is zero (Figure 3.3 f). The maximum temperature ( $T_{max}$ ) experienced by the rocks in the whole modelled history is shown with a blue, solid line in Figure 3.3 c. The results show that the rocks in the vicinity of the lithological boundary experienced temperatures in the order of 800°C. More specifically, the maximum temperature in the reference model was about 783°C. We note that the  $T_{max}$  distribution does not correspond to the temperature of a particular time instance.

### 3.3.2 Shear zone migration with time

The migration of the temperature maximum with time shown in Figure 3.3 is attributed

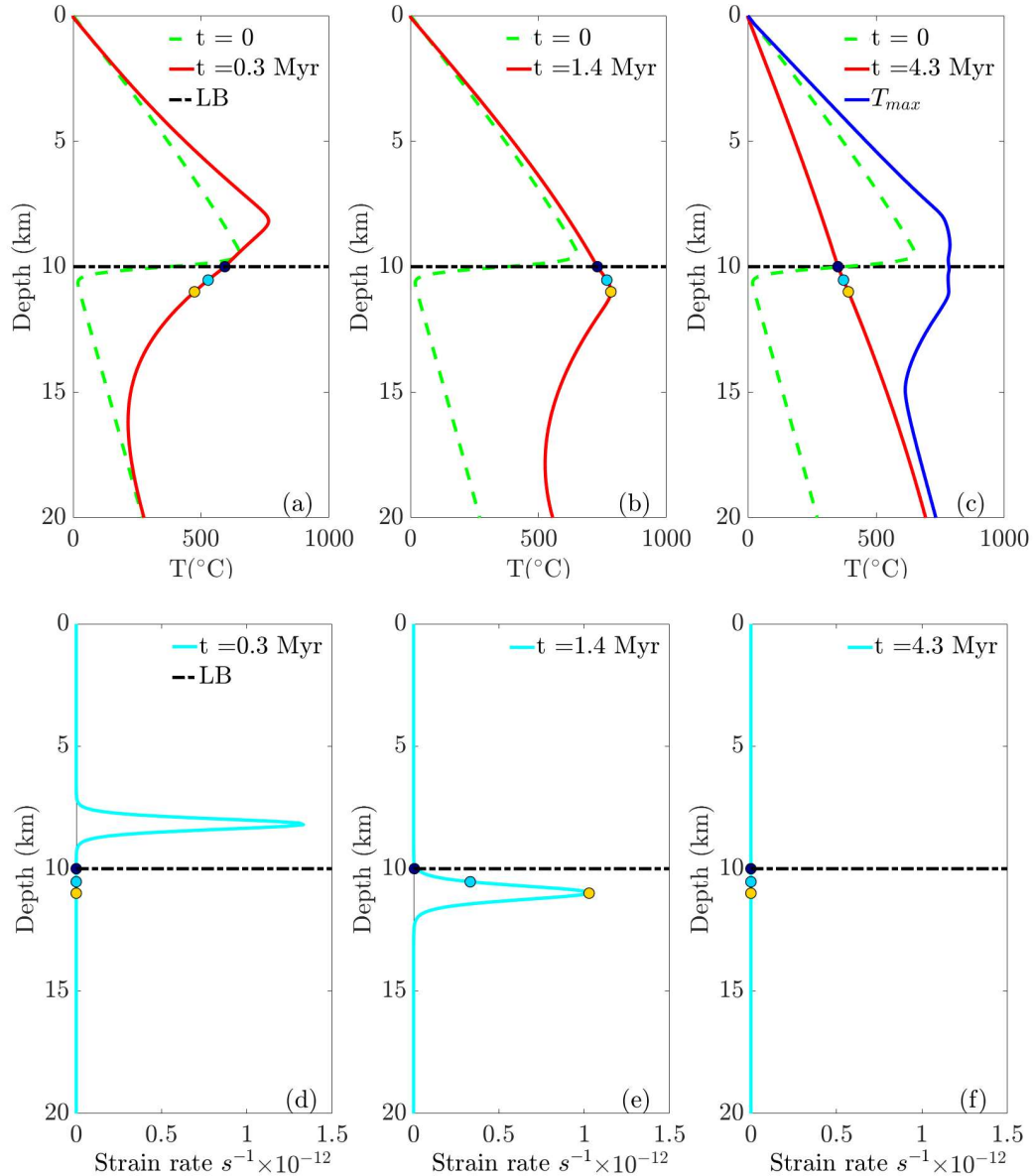


Figure 3.3 Temperature ( $T$ ) evolution (a,b,c) and strain rate ( $\dot{\epsilon}_{13}$ ) distribution (d,e,f) with time. The horizontal, black dashed line indicates the position of the lithological boundary. (a) Temperature distribution 0.3 Myr after the shearing initiation, (b) at the end of shearing (1.4 Myr), (c) at a time of 4.3 Myr. The initial temperature distribution is given with a green dashed line. The maximum temperature ( $T_{max}$ ) recorded by every point of the whole profile is shown using a blue solid line. (d) Strain rate distribution at the onset of shearing (0.3 Myr), (e) at 1.4 Myr, (f) at 4.3 Myr.

to the migration of the main shear zone as time progresses (Figure 3.4). The reason for this migration is the heat conduction from the, initially hotter, upper plate towards the lower plate. To be more specific, as the upper plate cools and the lower plate heats up simultaneously, this



process gradually decreases the lower plate's effective viscosity. This viscosity reduction is responsible for the localization of the shear zone at different depths. The distribution of the finite shear strain after 0.3, 0.7 and 1.4 Myr shows that the shear zone developed first in the upper plate and finally migrated in the lower plate (Figure 3.4). In fact, the migration of the active shear zone occurs in a progressive manner as it is shown in Figure 3.5 a. Such migration of the shear zone would be responsible for the accretion of the upper part of the oceanic upper plate at the base of the former upper plate.

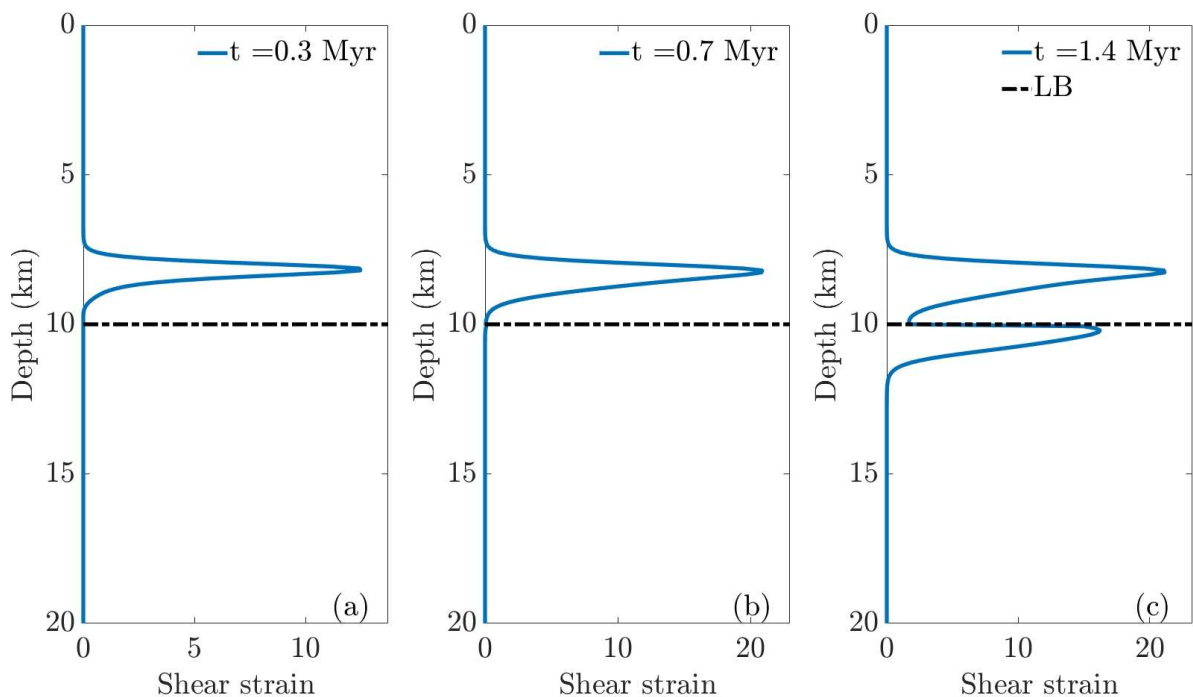


Figure 3.4 Finite shear strain evolution as a function of time after the shearing initiation. Shear strain has been calculated as the time integral of the shear strain rate ( $\int \dot{\epsilon}_{13} dt$ ). The horizontal, black dashed line indicates the position of the lithological boundary. (a) Finite shear strain at 0.3 Myr, (b) at 0.7 Myr, (c) at 1.4 Myr (end of shearing).

### 3.3.3 Cooling-rate constraints

One extraordinary feature from the metamorphic-sole rocks of Oman is the very high cooling rates inferred for the metamorphic minerals (Hacker *et al.* 1996, p. 1242). This shape of cooling path is characteristic for the rapid cooling of shear-zone rocks after a given time (Burg and Moulas 2022, p. 11). For this reason, we have considered that the shearing occurs only for a finite period of time. As it was mentioned earlier, the shearing in the reference model occurred only for a period of 1.4 Myr. The temperature evolution of rocks found in the vicinity of the initial lithological boundary is shown in Figure 3.5 b. Our thermal-history results (solid lines; Figure 3.5 b) show an exceptionally good fit when compared to the thermal histories

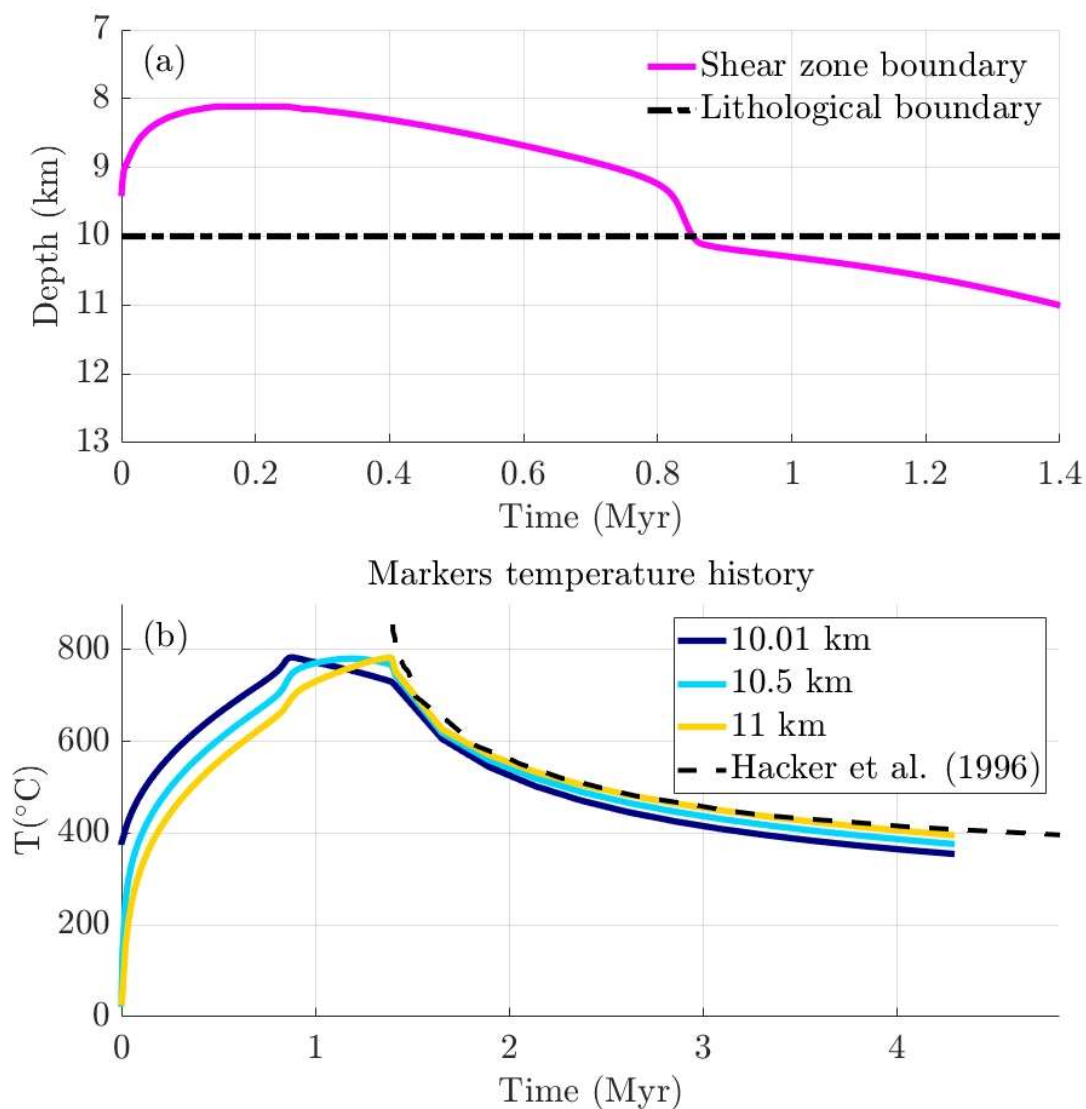


Figure 3.5 (a) Depth of the active shear zone with time. The depth of the shear zone is taken as the maximum of the strain rate ( $\dot{\epsilon}_{13}$ ) distribution at each time. The horizontal, dashed line indicates the position of the lithological boundary. (b) Temperature history of markers in the vicinity of the lithological boundary. The cooling history that has been inferred by Hacker *et al.* (1996) is shown using a dashed black line.

(dashed black line; Figure 3.5 b) inferred using thermochronology data (Hacker *et al.* 1996, p. 1242). These results also show that the highest cooling rates are expected immediately after the cessation of shearing.

### 3.3.4 Systematic investigations

Since the maximum temperature is always found in the region close to the lithological boundary (e.g. Figure 3.3 c), we have performed systematic investigations to get more insights on the thermal evolution of the rocks in that region. In these investigations, the shearing duration is assumed to be fixed at 1.4 Myr and we report the average temperature within 10 m

from the lithological boundary (above and below). Our results show that there is a strong dependence of the maximum temperature on the initial age of the ocean, especially for oceanic lithosphere that is younger than 2 Myr (Figure 3.6 a). This is probably because the ocean is still too hot to localize deformation and most of the heating of the lower plate is done via conduction from the upper domain. Beyond the age of 2 Myr, our results show that the age of the ocean is not an important parameter regarding the maximum temperature of the shear-zone rocks (Figure 3.6 a). In contrast, the shearing velocity plays the most dominant role in the rising of the maximum temperature (Figure 3.6 a). It is noted that only 2.5 cm/yr shearing velocity is sufficient to bring the temperature above 700°C (Figure 3.6 a). For the reference model, the

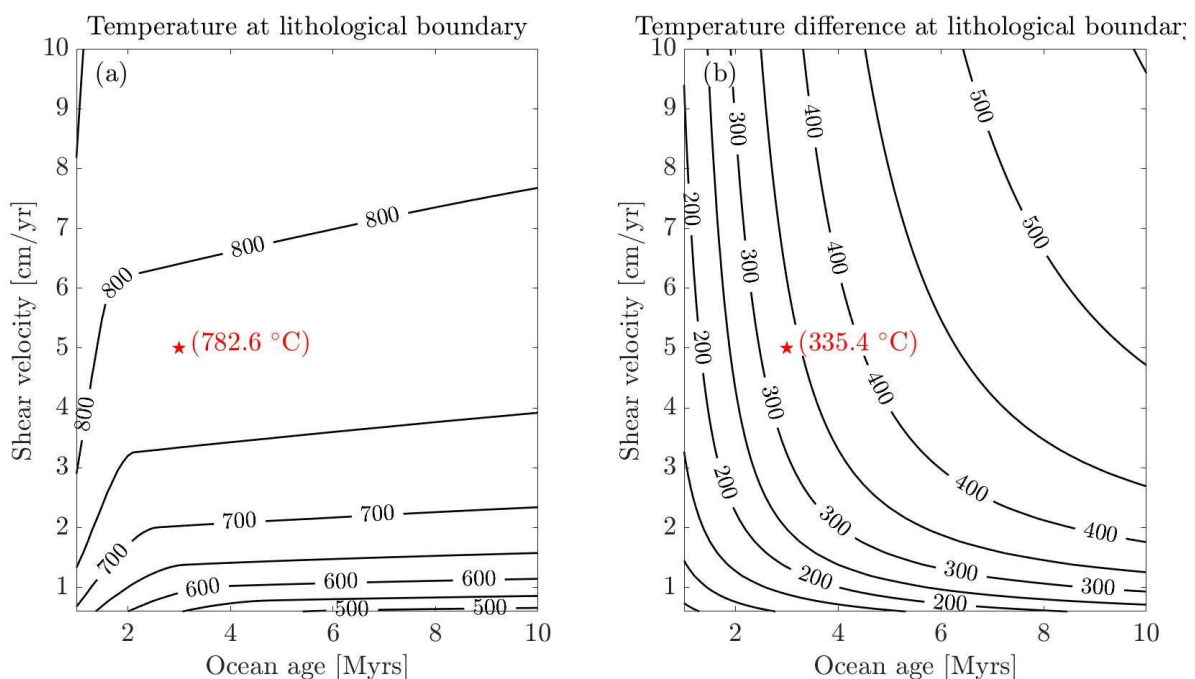


Figure 3.6 (a) Maximum temperature at the vicinity of the lithological boundary ( $\pm 10$  m) as a function of the age of the ocean (in Myr) and of the shearing velocity (in cm/yr). The red star indicates the parameters of the reference model (Figures 3.3-3.5). The value in parentheses indicate the maximum temperature value of the reference run. (b) Temperature difference from a purely thermal model as a function of the same parameters as in (a). The reference run is indicated by a red star and the value in the brackets indicates the temperature difference from the purely thermal model.

maximum temperature is around 783°C (red star; Figure 3.6 a). Increasing the shearing velocity beyond this level does not bring a dramatic increase on the maximum temperature value.

The relatively simple dependence of the maximum temperature on the shearing velocity allows us to deduce a simple relation from our results. By using bilinear-least squares fitting, the maximum temperature ( $T$ ) data shown in Figure 3.5 a can be described by the following simple relation:

$$T[^\circ\text{C}] = -2.0104 \cdot A_o[\text{Myr}] + 189.9315 \cdot \log_{10}(\Delta V[\text{cm} \cdot \text{yr}^{-1}]) + 924.6811 \quad (\text{Chapter 3:8})$$

where  $A_o$  is the age of the ocean in Myr and  $\Delta V$  is the velocity of shearing in cm/yr. This simple formula applies for velocities larger than or equal to 1.5 cm/yr and for ocean ages older than 2 Myr. Equation 3.8 can reproduce the data of Figure 3.6 a within 19 °C (maximum error). The mean absolute error of Eq. (3.8) is only 3.6 °C.

Finally, to see the effect of shear heating on the thermal model, we have also plotted the difference between the maximum temperature obtained using a thermo-mechanical model and the maximum temperature of a pure thermal (i.e. conductive) model (Figure 3.6 b). All other parameters (initial conditions, thermal parameters) remain the same as in the reference model. The results show that for our reference conditions, a purely thermal model predicts about 335 °C lower peak metamorphic temperatures, which is much lower than what is observed in the metamorphic sole of the Oman ophiolite. compared to the pure thermal model with the same parameters (Figure 3.6 b).

## 3.4 Discussion

For many years, researchers have considered shear (viscous or frictional) heating as a mechanism for generating the necessary temperature conditions required for the metamorphism of ophiolite soles (Woodcock and Robertson 1977). One of the challenges for this interpretation, however, is that most of the ophiolite soles are almost contemporaneous with the crustal sequence of the ophiolites above them. This relationship has been interpreted to reflect the fact that the oceanic lithosphere must be young (and hot) to be able to be obducted on the continent (Spray 1984; Wakabayashi and Dilek 2003b; Parlak *et al.* 2019). Recent thermomechanical models support that it is possible to obduct a hot and young oceanic lithosphere on the continental margin (Duretz *et al.* 2016b; Ibragimov and Moulas 2023). Therefore, the heat conducted from the young oceanic plate can be sufficient to explain the high-temperature metamorphic aureole beneath the ophiolite (England and Molnar 1993). One of the problems of the previous interpretation is related to the fact that the obducted oceanic lithosphere must be hot at the time that it is positioned on top of the crustal sequence. This requires that the tectonic movements are fast, and since shear heating scales proportional to the shearing velocity, shear heating cannot be excluded in modelling this process (Duprat-Oualid *et al.* 2015). Thus, models that include shear heating are needed to quantify the heating from

the overriding plate towards the footwall during obduction. Then, for each case, the importance of shear heating would be a model result and not an a-priori assumption.

One of the main assumptions in our work is the incorporation of a strong, crustal rheology (Rybacki and Dresen 2004). We have modified the high-stress limit of this rheology by employing a hyperbolic-sine flow law that approximates exponential creep at high stresses (Tsen and Carter 1987; Renshaw and Schulson 2017). This modification is needed to maintain reasonable levels of stress that would not grow beyond the strength of the material for the given shear velocities. It is possible however that the material of the hanging wall had a relatively softer rheology that would not allow the localization of deformation due to thermal softening. In such a case, the peak temperatures obtained would be significantly lower (Kiss *et al.* 2019).

When using a strong crustal rheology, as in our case, our models (Figure 3.6 a) revealed that velocities larger than 2 cm/yr are sufficient to generate metamorphic conditions that are in agreement with the values and the apparent metamorphic gradients reported in Oman and in other ophiolites in general (e.g. El-Shazly and Coleman, 1990; Jamieson, 1980). In fact, if shear heating was not considered, then the maximum temperature in the same region would be approximately 335 °C lower (Figure 3.6 b), and therefore it would not fit geological data. The fact that both the peak temperatures and the cooling rates are in agreement with the published data (Figure 3.5 b) suggests that our choice of conditions and parameters is realistic for the case of Oman ophiolite.

The fact that shear heating is important in our models, does not exclude the fact that heat is conducted from the hot, overriding plate towards the relatively cold footwall. This is, in fact, the reason for the migration of the active shear zone at depths lower within the footwall (Figure 3.5 a). As a result of the shear zone migration, the hanging wall incorporates parts that were original at the uppermost levels of the initial footwall (crustal domain). Therefore, we suggest that the combination of shear heating and heat conduction of a hot upper plate are responsible for: i) the high-temperature metamorphic conditions, ii) the apparent metamorphic inversion observed along the section, iii) the large cooling rates inferred in those rocks, and iv) the occurrence of the metamorphic sole below the mantle sequence.

## 3.5 Conclusions

In this study, we introduced new thermomechanical models that are pertinent to the study of ophiolite obduction. These models calculate stress, strain rate, and temperature distributions within a rock segment subjected to simple shear, consisting of two distinct lithologies. Our

findings indicate that integrating shear heating in a self-consistent manner yields maximum temperature and cooling-rate predictions that align with natural data. Focusing on Oman as an example, our analysis supports the notion that the high cooling rates deduced from thermochronological data are compatible with the fast cooling following the end of deformation. Additionally, our results demonstrate that thermal softening in the footwall during obduction triggers the shift of the primary shear zone into the footwall material. This shift ultimately leads to the incorporation of the metamorphic-sole rocks at the base of the ophiolite.

### 3.6 Acknowledgements

We would like to thank the Deutsche Forschungsgemeinschaft (DFG) - Project number 512790090 for support related to the development of the methods in this project. Prof. Dr. Kurt Stüwe is acknowledged for encouraging us to submit our results to AJES. D.K. acknowledges the European Research Council (Consolidator Grant 771143 (MAGMA) awarded to Boris J.P. Kaus), and the Research Council of Norway and the industry partners of NCS2030 (RCN project number 331644) for their support.

### 3.7 References

- Anonymous, 1972. Penrose Field Conference on ophiolites. *Geotimes* 17, 24–25.
- Azuma, S., Katayama, I., Nakakuki, T., 2014. Rheological decoupling at the Moho and implication to Venusian tectonics. *Scientific Reports* 4, 4403. <https://doi.org/10.1038/srep04403>
- Burg, J.-P., Moulas, E., 2022. Cooling-rate constraints from metapelites across two inverted metamorphic sequences of the Alpine-Himalayan belt; evidence for viscous heating. *Journal of Structural Geology* 156, 104536. <https://doi.org/10.1016/j.jsg.2022.104536>
- Cloos, M., 1993. Lithospheric buoyancy and collisional orogenesis: Subduction of oceanic plateaus, continental margins, island arcs, spreading ridges, and seamounts. *GSA Bulletin* 105, 715–737. [https://doi.org/10.1130/0016-7606\(1993\)105<0715:LBACOS>2.3.CO;2](https://doi.org/10.1130/0016-7606(1993)105<0715:LBACOS>2.3.CO;2)
- Dewey, J.F., 1976. Ophiolite obduction. *Tectonophysics* 31, 93–120. [https://doi.org/10.1016/0040-1951\(76\)90169-4](https://doi.org/10.1016/0040-1951(76)90169-4)

- Dilek, Y., Furnes, H., Shallo, M., 2007. Suprasubduction zone ophiolite formation along the periphery of Mesozoic Gondwana. *Gondwana Research* 11, 453–475. <https://doi.org/10.1016/j.gr.2007.01.005>
- Duprat-Oualid, S., Yamato, P., Schmalholz, S.M., 2015. A dimensional analysis to quantify the thermal budget around lithospheric-scale shear zones. *Terra Nova* 27, 163–168. <https://doi.org/10.1111/ter.12144>
- Duretz, T., Agard, P., Yamato, P., Ducassou, C., Burov, E.B., Gerya, T.V., 2016. Thermo-mechanical modeling of the obduction process based on the Oman Ophiolite case. *Gondwana Research* 32, 1–10. <https://doi.org/10.1016/j.gr.2015.02.002>
- El-Shazly, A.K., Coleman, R.G., 1990. Metamorphism in the Oman Mountains in relation to the Semail ophiolite emplacement. Geological Society, London, Special Publications 49, 473–493. <https://doi.org/10.1144/GSL.SP.1992.049.01.30>
- England, P., Molnar, P., 1993. The interpretation of inverted metamorphic isograds using simple physical calculations. *Tectonics* 12, 145–157. <https://doi.org/10.1029/92TC00850>
- Evans, B., Goetze, C., 1979. The temperature variation of hardness of olivine and its implication for polycrystalline yield stress. *Journal of Geophysical Research: Solid Earth* 84, 5505–5524. <https://doi.org/10.1029/JB084iB10p05505>
- Fleitout, L., Froidevaux, C., 1980. Thermal and mechanical evolution of shear zones. *Journal of Structural Geology* 2, 159–164. [https://doi.org/10.1016/0191-8141\(80\)90046-2](https://doi.org/10.1016/0191-8141(80)90046-2)
- Forsyth, D., Uyeda, S., 1975. On the Relative Importance of the Driving Forces of Plate Motion\*. *Geophysical Journal of the Royal Astronomical Society* 43, 163–200. <https://doi.org/10.1111/j.1365-246X.1975.tb00631.x>
- Frisch, W., Meschede, M., Blakey, R., 2011. *Plate Tectonics: Continental Drift and Mountain Building*. Springer.
- Garber, J.M., Rioux, M., Kylander-Clark, A.R.C., Hacker, B.R., Vervoort, J.D., Searle, M.P., 2020. Petrochronology of Wadi Tayin Metamorphic Sole Metasediment, With Implications for the Thermal and Tectonic Evolution of the Semail Ophiolite (Oman/UAE). *Tectonics* 39, e2020TC006135. <https://doi.org/10.1029/2020TC006135>
- Garfunkel, Z., 2006. Neotethyan ophiolites: formation and obduction within the life cycle of the host basins. Geological Society, London, Special Publications 260, 301–326. <https://doi.org/10.1144/GSL.SP.2006.260.01.13>
- Guilmette, C., Smit, M.A., van Hinsbergen, D.J.J., Gürer, D., Corfu, F., Charette, B., Maffione, M., Rabeau, O., Savard, D., 2018. Forced subduction initiation recorded in the sole

and crust of the Semail Ophiolite of Oman. *Nature Geoscience* 11, 688–695. <https://doi.org/10.1038/s41561-018-0209-2>

Hacker, B.R., 1990. Simulation of the metamorphic and deformational history of the metamorphic sole of the Oman Ophiolite. *Journal of Geophysical Research: Solid Earth* 95, 4895–4907. <https://doi.org/10.1029/JB095iB04p04895>

Hacker, B.R., Mosenfelder, J.L., Gnos, E., 1996. Rapid emplacement of the Oman ophiolite: Thermal and geochronologic constraints. *Tectonics* 15, 1230–1247. <https://doi.org/10.1029/96TC01973>

Ibragimov, I., Moulas, E., 2023. The role of continental-margin architecture on models of ophiolite emplacement. *Journal of the Geological Society* jgs2023-063. <https://doi.org/10.1144/jgs2023-063>

Jamieson, R.A., 1980. Formation of metamorphic aureoles beneath ophiolites— Evidence from the St. Anthony Complex, Newfoundland. *Geology* 8, 150–154. [https://doi.org/10.1130/0091-7613\(1980\)8<150:FORABO>2.0.CO;2](https://doi.org/10.1130/0091-7613(1980)8<150:FORABO>2.0.CO;2)

Kiss, D., Podladchikov, Y., Duretz, T., Schmalholz, S.M., 2019. Spontaneous generation of ductile shear zones by thermal softening: Localization criterion, 1D to 3D modelling and application to the lithosphere. *Earth and Planetary Science Letters* 519, 284–296. <https://doi.org/10.1016/j.epsl.2019.05.026>

Liati, A., Gebauer, D., Fanning, C.M., 2004. The age of ophiolitic rocks of the Hellenides (Vourinos, Pindos, Crete): first U–Pb ion microprobe (SHRIMP) zircon ages. *Chemical Geology* 207, 171–188. <https://doi.org/10.1016/j.chemgeo.2004.02.010>

Malpas, J., 1979. The dynamothermal aureole of the Bay of Islands ophiolite suite. *Canadian Journal of Earth Sciences* 16, 2086–2101. <https://doi.org/10.1139/e79-198>

Moores, E.M., 1982. Origin and emplacement of ophiolites. *Reviews of Geophysics* 20, 735–760. <https://doi.org/10.1029/RG020i004p00735>

Moulas, E., Burg, J.-P., Podladchikov, Y., 2014. Stress field associated with elliptical inclusions in a deforming matrix: Mathematical model and implications for tectonic overpressure in the lithosphere. *Tectonophysics* 631, 37–49. <https://doi.org/10.1016/j.tecto.2014.05.004>

Moulas, E., Kaus, B., Jamtveit, B., 2022. Dynamic pressure variations in the lower crust caused by localized fluid-induced weakening. *Communications Earth & Environment* 3, 157. <https://doi.org/10.1038/s43247-022-00478-7>



Myhill, R., 2011. Constraints on the evolution of the Mesohellenic Ophiolite from subophiolitic metamorphic rocks. *Geological Society of America Special Papers* 480, 75–94. [https://doi.org/10.1130/2011.2480\(03\)](https://doi.org/10.1130/2011.2480(03))

Parlak, O., Dunkl, I., Karaođlan, F., Kusky, T.M., Zhang, C., Wang, L., Koepke, J., Billor, Z., Hames, W.E., ŐimŐek, E., ŐimŐek, G., ŐimŐek, T., Öztürk, S.E., 2019. Rapid cooling history of a Neotethyan ophiolite: Evidence for contemporaneous subduction initiation and metamorphic sole formation. *GSA Bulletin* 131, 2011–2038. <https://doi.org/10.1130/B35040.1>

Pomonis, P., Tsikouras, B., Hatzipanagiotou, K., 2002. Origin, evolution and radiometric dating of subophiolitic metamorphic rocks from the Koziakas ophiolite (W. Thessaly, Greece). *Neues Jahrbuch Für Mineralogie, Abhandlungen* 177, 255–276. <https://doi.org/10.1127/0077-7757/2002/0177-0255>

Ranalli, G., 1995. *Rheology of the Earth*, 2nd ed. Chapman and Hall.

Renshaw, C.E., Schulson, E.M., 2017. Strength-limiting mechanisms in high-confinement brittle-like failure: Adiabatic transformational faulting. *Journal of Geophysical Research: Solid Earth* 122, 2016JB013407. <https://doi.org/10.1002/2016JB013407>

Rioux, M., Garber, J., Bauer, A., Bowring, S., Searle, M., Kelemen, P., Hacker, B., 2016. Synchronous formation of the metamorphic sole and igneous crust of the Semail ophiolite: New constraints on the tectonic evolution during ophiolite formation from high-precision U–Pb zircon geochronology. *Earth and Planetary Science Letters* 451, 185–195. <https://doi.org/10.1016/j.epsl.2016.06.051>

Rybacki, E., Dresen, G., 2004. Deformation mechanism maps for feldspar rocks. *Tectonophysics* 382, 173–187. <https://doi.org/10.1016/j.tecto.2004.01.006>

Spray, J.G., 1984. Possible causes and consequences of upper mantle decoupling and ophiolite displacement. *Geological Society, London, Special Publications* 13, 255. <https://doi.org/10.1144/GSL.SP.1984.013.01.21>

Spray, J.G., Roddick, J.C., 1980. Petrology and  $^{40}\text{Ar}/^{39}\text{Ar}$  geochronology of some hellenic sub-ophiolite metamorphic rocks. *Contributions to Mineralogy and Petrology* 72, 43–55. <https://doi.org/10.1007/BF00375567>

Stüwe, K., 2007. *Geodynamics of the Lithosphere*, 2nd ed. Springer-Verlag Berlin Heidelberg.

Stüwe, K., Ehlers, K., 1998. Distinguishing Cooling Histories using Thermometry. Interpretations of Cooling Curves with some Examples from the Glein-Koralp Region and the Central Swiss Alps. *Mitteilungen Der Österreichischen Geologischen Gesellschaft* 89, 201–212.

Tsenn, M.C., Carter, N.L., 1987. Upper limits of power law creep of rocks. *Tectonophysics* 136, 1–26. [https://doi.org/10.1016/0040-1951\(87\)90332-5](https://doi.org/10.1016/0040-1951(87)90332-5)

Wakabayashi, J., Dilek, Y., 2003. What constitutes ‘emplacement’ of an ophiolite?: Mechanisms and relationship to subduction initiation and formation of metamorphic soles. *Geological Society, London, Special Publications* 218, 427–447. <https://doi.org/10.1144/GSL.SP.2003.218.01.22>

Whitechurch, H., Parrot, J., 1978. Ecailles métamorphiques infrapéridotiques dans le Pinde septentrional (Grèce): croûte océanique, métamorphisme et subduction. *Comptes Rendus de l’Académie Des Sciences Paris* 286, 1491–1494.

Whitechurch, H., Parrot, J.F., 1974. Les écailles métamorphiques infrapéridotitiques du Baër-Bassit (nord-ouest de la Syrie). *Cah. ORSTOM, Sér. Géol.* VI, 173–184.

Williams, H., Smyth, W.R., 1973. Metamorphic aureoles beneath ophiolite suites and alpine peridotites; tectonic implications with west Newfoundland examples. *American Journal of Science* 273, 594–621. <https://doi.org/10.2475/ajs.273.7.594>

Woodcock, N.H., Robertson, A.H.F., 1977. Origins of some ophiolite-related metamorphic rocks of the “Tethyan” belt. *Geology* 5, 373–376. [https://doi.org/10.1130/0091-7613\(1977\)5<373:OOSOMR>2.0.CO;2](https://doi.org/10.1130/0091-7613(1977)5<373:OOSOMR>2.0.CO;2)

Yuen, D.A., Fleitout, L., Schubert, G., Froidevaux, C., 1978. Shear deformation zones along major transform faults and subducting slabs. *Geophysical Journal of the Royal Astronomical Society* 54, 93–119. <https://doi.org/10.1111/j.1365-246X.1978.tb06758.x>

---

## Chapter 4

# Geochronological constraints for ophiolite obduction

## 4.1 Introduction

Ophiolites are rock complexes that are originally formed in oceanic environments (Condie and Stern, 2023; Dilek and Furnes, 2014). More specifically, ophiolites that are currently found on continental regions are thought to represent unique evidence of orogenic processes such as subduction and collision (Dewey, 1976; Moores, 1982). Ideally, ophiolite complexes are composed by (from top to bottom): i) oceanic sediments, ii) mafic dykes and lavas, iii) crustal cumulates, and iv) peridotites, all of which are found tectonically emplaced upon lithologies of continental affinities (Anonymous, 1972). Of course this ideal pseudostratigraphy of ophiolites is not always found as expected, and different localities can present various characteristics (Rassios and Dilek, 2009). Despite such differences, it is clear that understanding the processes of ophiolite emplacement or “obduction” (Dewey, 1976; Moores, 1982; Wakabayashi and Dilek, 2003) can provide us with unique information regarding planetary scale processes such as orogenesis.

A fundamental difficulty in investigating ophiolite rocks is the fact that, due to their density, and negative buoyancy, rocks of the oceanic lithosphere are commonly expected to subduct and disappear in subduction zones (Cloos, 1993). In fact, the subduction process is expected to eliminate most of the surface evidence for the former presence of ophiolites in the geological record (Dewey, 1976). Thus, the study of the scarce ophiolite rocks and their associations is critical for the understanding of emplacement processes.

For the past decades many researchers have focused on the structural relationships, the petrologic characteristics and the age relationships of ophiolite complexes (Wakabayashi and Dilek, 2003). Such data can be used to deduce the geological histories of rock and regions given their final state. An important constrain in many geodynamic studies is the thermal history of

rocks. The thermal history of metamorphic rocks associated to ophiolites provides important information about time relationships and the related metamorphic processes.

The importance of thermal history is important for several reasons. Temperature is a crucial parameter on rock rheology (Brace and Kohlstedt, 1980; Tsenn and Carter, 1987) and therefore, understanding the temperature distribution and evolution is crucial for the mechanical evolution of rocks. Additionally, temperature is a critical factor in diffusion of chemical species in minerals since it depends on the absolute temperature (T) on non-linear (Arrhenius) manner. A typical temperature dependence of diffusivity is given by the following form

$$D = D_0 \exp\left(-\frac{Q}{RT}\right) \quad (\text{Chapter 4: . 1})$$

where D is the diffusivity of a chemical species in m<sup>2</sup>/sec, D<sub>0</sub> is the pre-exponent factor (also in m<sup>2</sup>/sec), Q is the activation energy (in J/mol), and R is the universal gas constant (in J/K/mol). Equation Chapter 4:1 indicates that with increased temperature, diffusivity is increasing dramatically.

An important consequence of the diffusivity increase with temperature is the apparent age reset of some geochronological systems. This is because some isotopes such as <sup>40</sup>K produce isotopes of noble gases (such as <sup>40</sup>Ar) that are difficult to be retained in the mineral lattice. This is because during the accumulation of radiogenic <sup>40</sup>Ar, concentration gradients develop that can drive solid-state diffusion (McDougall and Harrison, 1999). As a result, radiogenic <sup>40</sup>Ar can reach the outer surface of a mineral and be released to the environment. The consequence of the previous process is that any geochronology method that is based on the <sup>40</sup>K -<sup>40</sup>Ar decay (such as the Ar-Ar method) will yield different apparent ages depending on the thermal history of the rocks (Lister and Baldwin, 1996; McDougall and Harrison, 1999; Wheeler, 1996). This fact was recognised by Dodson in the 1970s who developed on the concept of closure temperature, i.e. a temperature below which, diffusion is negligible and minerals retain all the accumulated radiogenic isotope (Dodson, 1973).

The sensitivity of apparent age to the thermal history of rocks has been for long a matter of detailed investigation (Braun et al., 2006; Reiners and Brandon, 2006). In these early studies, the thermal evolution of rocks was modelled using thermo-kinematic models and the resulting apparent ages were calculated for various geochronology systems (Batt et al., 2001; Batt and Brandon, 2002). However, most such studies focused in simplified scenarios where the temperature and the velocity field were assumed to be in steady state and therefore, such model prediction cannot be generalized to cases where the steady-state assumption is not valid.

The aim of this work is to study the distribution of apparent isotopic ages in an evolving orogen. We focus on an orogen that is characterised by the obduction of a small, and young oceanic crust on the continental margin. We utilize the geodynamic models performed in Chapter 2 and we calculate the apparent  $^{40}\text{Ar}$ - $^{39}\text{Ar}$  ages for different crustal minerals. Our results show that erosion leads to the formation of specific patterns of apparent mineral age at the surface of the orogen. In particular, our results show regions where the apparent age of rocks becomes younger. These regions are within and around domains of large plastic strain. This is explained because it is in those regions that we have the juxtaposition of rocks with various thermal histories. Furthermore, we have also investigated the influence of different grain sizes used to calculate the apparent  $^{40}\text{Ar}$ - $^{39}\text{Ar}$  age. Smaller grain sizes tend to provide younger apparent ages, however the age trends observed are very similar.

## 4.2 Methods

As a reference geodynamic model, we used the model with erosion and reduced convergence shown in Chapter 2 (Figure 2.8 e-h). More specifically, it is a model where the convergence rate slows down to 1 cm/year after 5 myrs and also has a prescribed erosion rate (0.1 cm/year) at the surface. A detail of the initial configuration of this model is shown in Figure

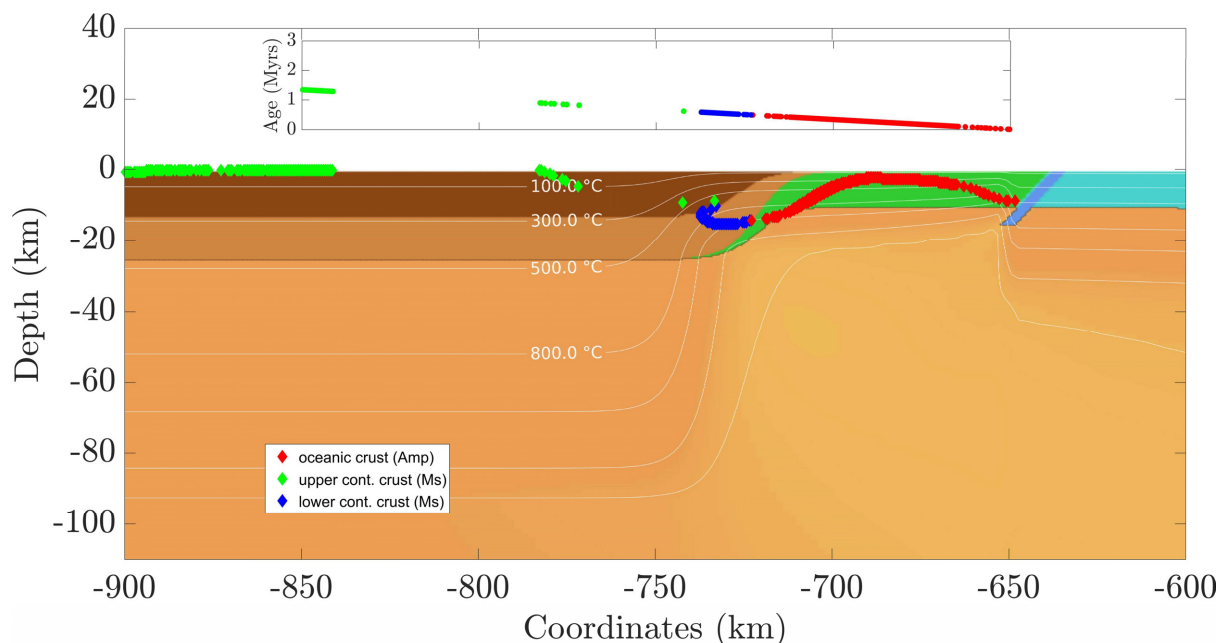


*Figure 4.1 Detail of the initial configuration of geodynamic model used in this study. The dotted symbols in green, blue and red colours indicate the location of the 305 markers for which the thermal evolution is monitored. An initial age of the different markers is assumed at the beginning of the model. The initial age is shown in the inlet above. For the purpose of this study, muscovite was chosen to represent the minerals in the continental crust, while amphibole was selected for the oceanic crust.*

4.1. In this model, we have chosen a set of representative markers (passive tracers) to track their thermal evolution closely.

Each passive marker follows a particular point in the lithosphere and records the history of pressure and temperature of that point throughout the model run. The markers were selected based on their surface exposure at the end of the model run (after 10 Myr). The end of the model run is shown in Figure 4.2. Apart from the final distribution of rocks, and the temperature distribution, one can see the distribution of apparent radiogenic age at the surface of the orogenic region (inlet on top of figure).

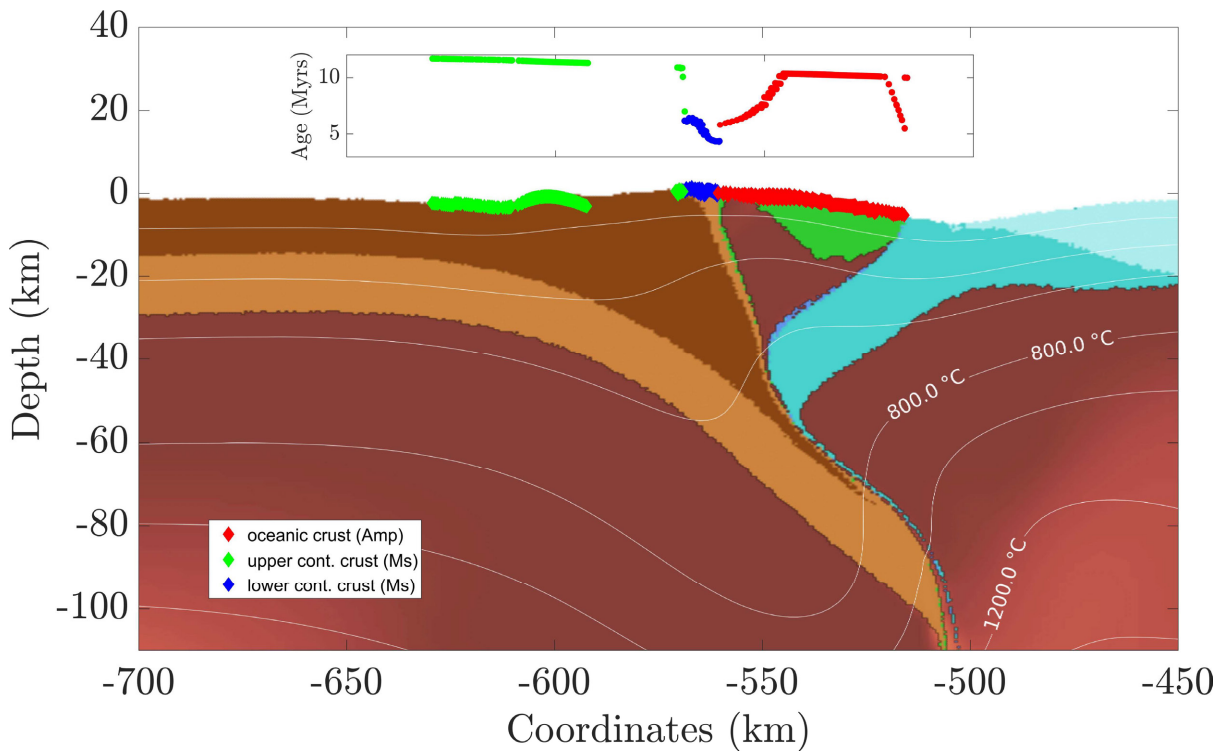


Figure 4.2 Detail of the final configuration of geodynamic model used in this study. The dotted symbols in green, blue and red colours indicate the location of the 305 markers for which the thermal evolution is monitored (same points as in Figure 4.1). For the purpose of this study, muscovite was chosen to represent the minerals in the continental crust, while amphibole was selected for the oceanic crust. The inlet above shows the apparent Ar-Ar ages at the surface of the model domain.

The apparent  $^{40}\text{Ar}$ - $^{39}\text{Ar}$  ages were calculated using the routines of KADMOS (Moula and Brandon 2022b). The resulting  $^{40}\text{Ar}$ - $^{39}\text{Ar}$  ages are calculated based on the amount of the  $^{40}\text{Ar}$  produced during the decay of  $^{40}\text{K}$ . KADMOS is a MATLAB/Octave-based software that is used to calculate the apparent  $^{40}\text{Ar}$ - $^{39}\text{Ar}$  ages of minerals based on their temperature history. It uses the finite element method (FEM) to solve the following equation in 1 dimension (in planar, cylindrical or spherical coordinates):

$$\frac{\partial}{\partial t} \left( \frac{Ar}{K_0} \right) = D \nabla^2 \left( \frac{Ar}{K_0} \right) + \lambda_{Ar} e^{-\lambda_T t} \quad (\text{Chapter 4: .2})$$

where  $A_r$  is the amount of  $^{40}\text{Ar}$ ,  $K_0$  is the initial amount of  $^{40}\text{K}$  in the mineral (assumed homogeneous),  $\lambda_{Ar}$  is the decay constant of  $^{40}\text{K}$  to  $^{40}\text{Ar}$  ( $0.581 \cdot 10^{-10}$  yrs) and  $\lambda_T$  is the total decay constant of  $^{40}\text{K}$  to  $^{40}\text{Ar}$  and  $^{40}\text{Ca}$  ( $5.543 \cdot 10^{-10}$  yrs). The decay parameters come from McDougall and Harrison, (1999). To perform calculations with KADMOS, one needs to specify the geometry of the crystal domain (planar, cylindrical or spherical), the mineral system (muscovite, biotite, K-feldspar or amphibole) and the thermal history. In our case, we consider the  $^{40}\text{Ar}$  diffusion values from Grove and Harrison, (1996), Harrison, (1982), and Harrison et al., (2009). In addition, we consider spherical crystal geometries and a grain size of 100 microns.

In order to have a more realistic age distribution, we considered that, initially, the apparent ages of the different rock units were not identical (Figure 4.1). This is justified because the rocks of the oceanic crust are not expected to form simultaneously, and younger rocks are expected to be present near the mid-ocean ridges. Thus, the initial age of rocks increases as a function of distance from the centre of the mid-ocean ridge (Figure 4.2). We choose one of our previous models to be the reference model for this study. The rest of the material parameters and boundary conditions are identical to the model shown in Figure 2.8 of Chapter 2 (Ibragimov and Moulas, 2023).

## 4.3 Results

Figure 4.1 shows the initial structure of the lithosphere at the onset of convergence. It is important to note the initial age distribution in the inlet of Figure 4.1. The markers which are closest to the mid-ocean ridge of the oceanic crust have an initial apparent age of 0 Myrs and those furthest from the ridge point have an initial apparent age of 0.48 Myrs. Figure 4.2 shows the distribution of markers and their apparent ages (inset) at the end of the simulation. It can be seen that markers initially located deep in the lower continental crust (blue) and oceanic crust (leftmost red dots) in Figure 4.1 have been brought to the surface by uplift and erosion during ophiolite obduction. The inlet of Figure 4.2 shows the apparent age distribution for the rocks that reached the surface after 10 Myr. It is clear from this figure that the age distribution is not homogeneous and there are observable differences in the apparent ages of the surface rocks.

The comparison of the relative positions of the markers in Figure 4.1 and Figure 4.2 shows the extent of deformation and erosion that this zone has undergone. In particular, the markers in the middle-to-lower continental crust were initially located at a depth of 14 km and surfaced in less than 10 Myrs. It is evident from comparing the previous figures that this model's

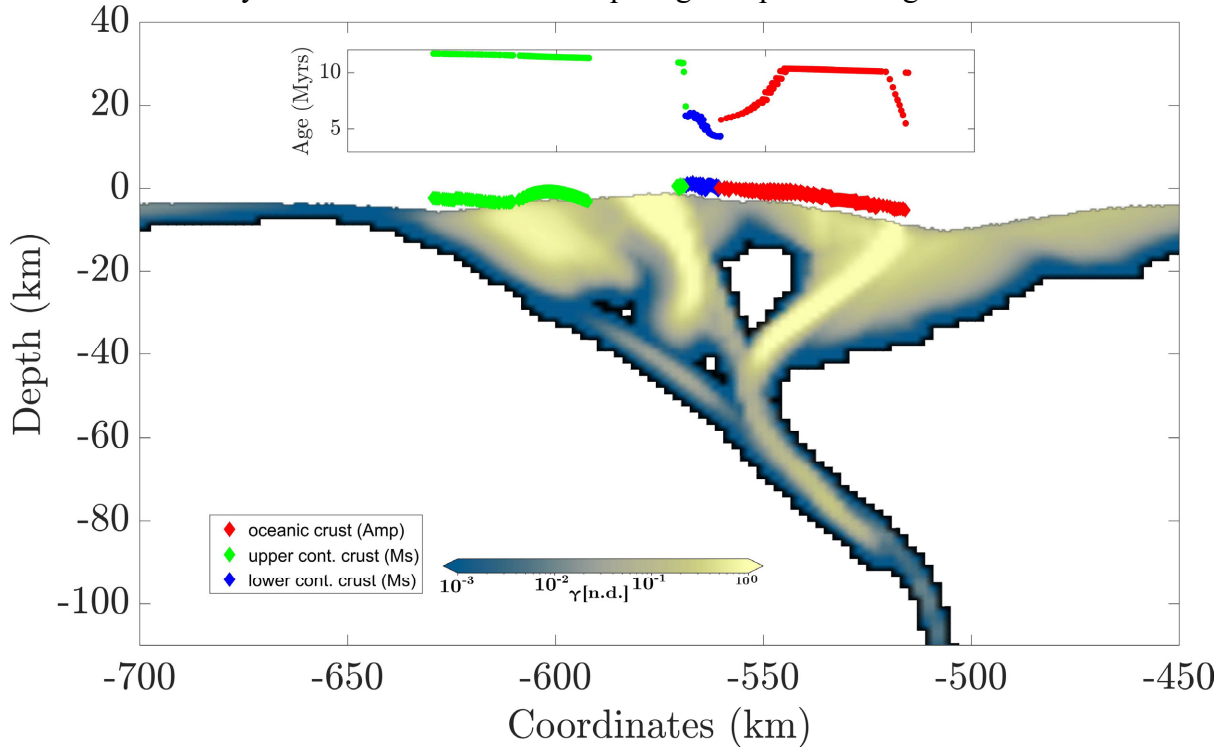


Figure 4.3 Plastic deformation for the region shown in Figure 4.2. The inset shows the distribution of the apparent ages at the surface of the model.

evolution does not lead to a steady-state distribution of velocities or temperatures within the specified time frame. However, this model shows the emplacement and further exhumation of the ophiolite complex in a double-vergent zone, similar to the ones described in Chapter 2. More specifically, the ophiolite is bounded by two high-strain shear zones (Figure 4.3) where plastic deformation is increased. By being bounded by the two conjugate shear zones, the obducted block is uplifted and exhumed even though the whole system undergoes continuous convergence. This process results in the formation of a new subduction zone in place of the initial retro shear zone. The accretionary process causes the left part of the obducting block to move upwards and to the right in the model domain, resulting in significant erosion on the left side of the ophiolite complex. In contrast, the right-side of the ophiolite complex experiences less intense uplift and erosion.



Apart from the exhumed modelled ophiolite complex shown in Figure 4.1 – 4.3, what is important to note is the distribution of the apparent ages. These ages are shown in detail Figure 4.4. As a reference, we used muscovite and amphibole crystals of 100 $\mu$ m in diameter. The markers that were initially in the lower crust (blue points) at the left of the model domain and the adjacent parts of the oceanic crust (red points) exhibit a significantly younger apparent age than all other points. This is because these points have experienced higher-temperature conditions. The initially deeper initial location of these rocks is consistent with the higher temperatures experienced during the geodynamic evolution. This resulted in the constant resetting of their K-Ar 'clocks' at the initial stages of their evolution. Consequently, their apparent age is 5-6 million years younger (Figure 4.4) than what it should have been if the K-Ar system was undisturbed by diffusion.

The markers for oceanic crust (red) exhibit a pattern in which the middle cluster of points is distributed along a line that is very similar in slope to the initial age distribution (Figure 4.4). The same pattern can be observed for most of the upper-crustal rocks (green). During the emplacement of the modelled ophiolite, these parts remained at the surface and did not undergo P-T conditions where diffusion would be significant to affect their K-Ar dates. The rightmost

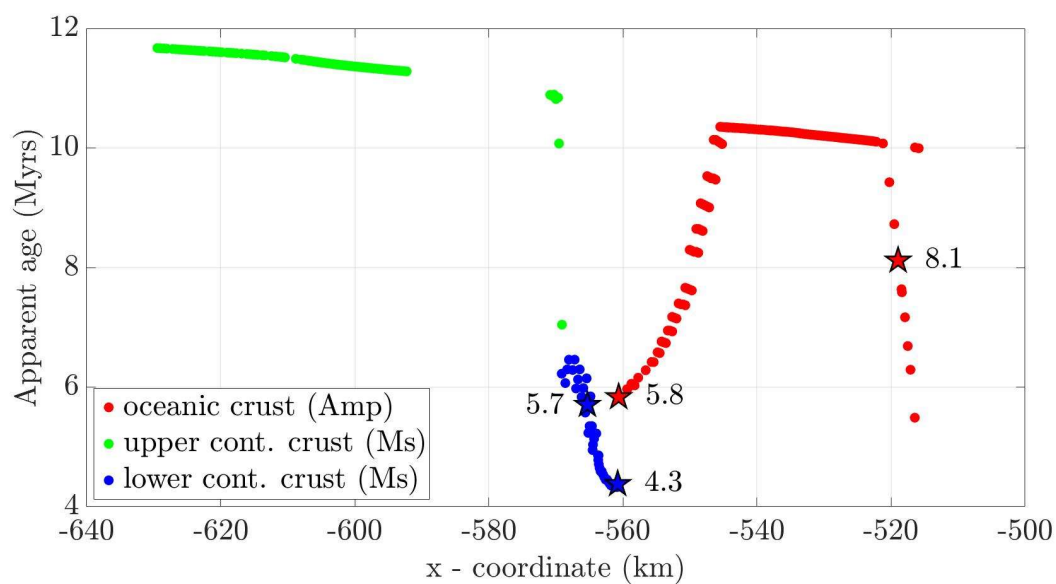


Figure 4.4 Apparent ages of markers that reached the surface in our geodynamic model (Figure 4.1 – 4.3). Two different minerals have been used to represent the two different crustal compositional groups, muscovite (for continental rocks) and amphibole (for oceanic rocks). The stars indicate specific markers for which, the P-T evolution is given in Figure 4.5.

part of the oceanic crust, located near the ridge axis, experienced rejuvenation due to exposure to high temperatures, which reset its thermochronological clock.

Markers shown as stars have been selected to show their P-T evolution in Figure 4.5. The numbers next to each graph correspond to their apparent age at the final time step in millions

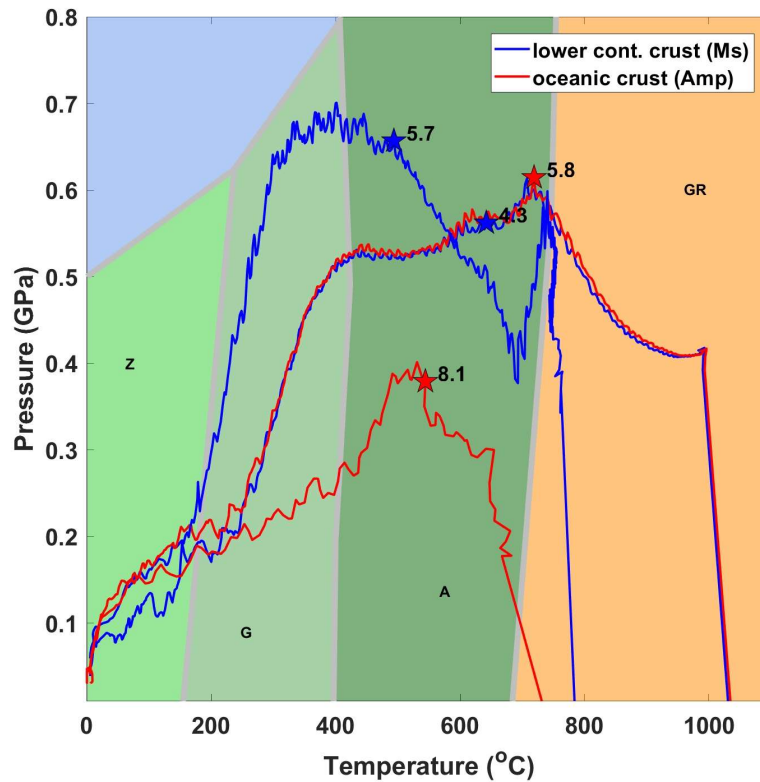


Figure 4.5 .P-T evolution of selected markers that reached the surface. The different colours indicate the extend of the different metamorphic facies (see Chapter 2 Figure 2.10 for details)

of years. The lines with ages of 5.8 Myrs and 4.3 Myrs are nearly identical despite having different ages. This fact will be explained in the discussion section. The graphs for all points show a steady decline in temperature, indicating that all markers eventually ended up at the surface. However, the blue marker with an age of 5.7 Myrs experienced a large pressure build-up before a rapid decline at some point. This observation can also be applied to markers with ages of 5.8 Myrs and 4.3 Myrs. The marker point with an age of 8.1 Myrs experienced lower values of pressure and temperature, consistent with its old apparent age (Figure 4.5).

Apart from the muscovite and amphibole with a fixed grain size, we also considered the investigation of various grain sizes for minerals that can be found in association with both continental and oceanic crustal rocks. Figure 4.6 presents the results of a systematic investigation of the effect of different grain sizes and minerals on the apparent ages of rocks with the same P-T history as the markers exposed at the surface (Figure 4.1 – 4.3). The general observation is that there is no age discontinuity between the lower continental crust (blue) and the oceanic crust as in Figure 4.4, since in this figure all points in each column have the same diffusion properties. However, the distribution of the apparent ages still shows younger apparent ages near the regions of high plastic strain (Figure 4.3). In general larger grain size results in older apparent ages. For instance, in the first column of a model with a grain size of

25 micrometers, the youngest rocks on the rightmost part of the oceanic crust indicate an age of 4.96 million years. However, the same rocks with a grain size of 100 micrometers will give an apparent age of 5.48 million years (Figure 4.6).

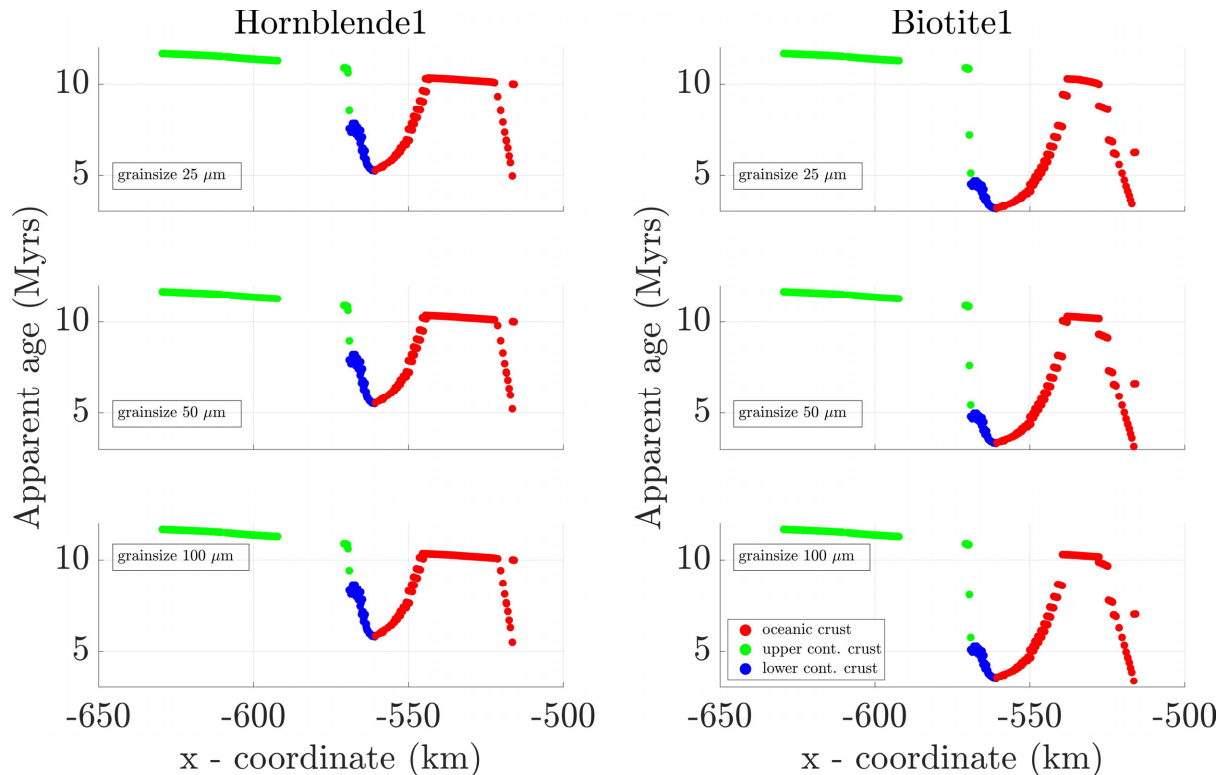


Figure 4.6 Apparent age distribution for the surface markers assuming different grainsizes and different minerals. The different markers are identical to those shown in Figure 4.1 – 4.4.

As expected, a more pronounced difference in apparent age was observed in this investigation when different minerals were used. In figure 6, the first column used diffusion constants corresponding to measurements made for hornblende (Harrison, 1982), while the second column assumed diffusion coefficients of biotite (Grove and Harrison, 1996). It is worth noting that diffusion calculations involving biotite will result in much younger rock ages. For instance, taking the youngest rock for hornblende with a grain size of 25 micrometers gives an age of only 5.24 million years (Figure 4.6). However, for the same grain size but for biotite, the age is only 3.14 million years (Figure 4.6). Additionally, the 'flat' part of the oceanic crust has fewer data points, and more markers have experienced some reset in their apparent ages (Figure 4.6).

## 4.4 Discussion

Our results show that it is possible to combine different kinds of forward models (geodynamic and thermochronology models) in an attempt to consider test geodynamic scenarios and their consequences in the rock record. The aim of this work was to study the geochronological constraints of ophiolite rocks. We utilised markers from a geodynamical model of ophiolite obduction to track the evolution of the rocks' P-T path, which can be observed on the surface at the end of the simulation. The results indicate that uneven erosion exposes at the surface rocks that have a range of apparent ages (Figure 4.2– 4.4). However, the uneven distribution of erosion is caused by a combination of uneven vertical and lateral movements. Our study confirmed the findings of previous authors who supported that lateral movements is as important as vertical movements, such as uplift and erosion, when studying geochronological constraints in orogenic systems (Batt et al., 2001; Batt and Brandon, 2002). Lateral movements provide a kinematic context for the thermal evolution of rocks by generating more complex P-T paths and accounting for high pressures in the shallow parts of the lithosphere.

In general, and consistently with previous thermo-kinematic studies, rocks that experience deeper (and hotter) conditions for longer times yield younger apparent ages (Batt et

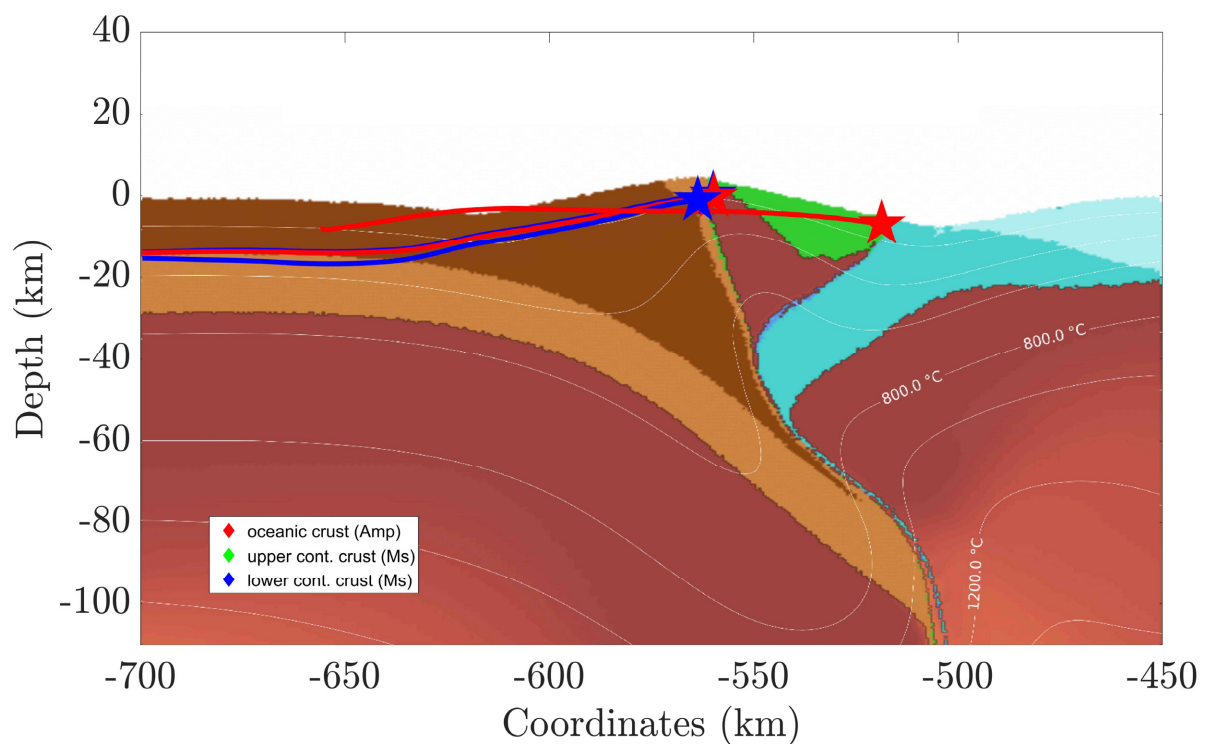


Figure 4.7 Trajectories for selected exhumed markers. Note that the markers with the youngest apparent ages are the ones that experienced higher temperature conditions at deeper levels of the crust.

al., 2001). However, in our case the velocity field was constantly updated using a thermo-mechanic model. Figure 4.7 shows the movement trajectory of selected markers. Although the front part of the modelled ophiolite complex did not experience significant vertical movement, the left side of the complex travelled a longer path, resembling the underplating in the accretionary wedge described in Batt et al. (2001). In general, the obducted ophiolite block has undergone a rotating movement during its emplacement. This would not have been possible if only vertical movement was considered. This also supports the idea that the obducted ophiolites in this scenario were formed as one continuous tectonic event. Matching modeled apparent ages with ages measured in a laboratory in the same area can constrain the convergence velocity and erosion rates of the region. The comparison of geodynamic models with measurable quantities offers unique advantages in the constraining of the ill-posed models of geodynamic evolution.

The complex trajectory shown in Figure 4.7 is a result of movement along two conjugate shear zones that alternate during the obduction process. According to Batt et al. (2001), retro-shear zones are often observed as low-seismic zones in orogenic systems. These zones may be influenced by local heat sources, such as shear heating, which was explored in Chapter 3. In such areas, the increased dissipative heating will contribute to the reset of isotopic ages in the vicinity of the shear zone. However, the range of influence of the age-reset is expected to be much wider than the width of the plastic zone (Kiss et al., 2019; Schmalholz and Duretz, 2015). In any case, our results clearly show gradients in the apparent age of exhumed rocks in the vicinity of high-strain zones (Figures 4.2– 4.4). In this case, our younger ages observed in (Figures 4.2– 4.4 may not be strongly influence by dissipative heating, however, it is along these shear zones where the deepest parts of the orogen exhume. Thus, it is very important to be able to see the resulting apparent-age gradients at the end of orogenesis.

Our systematic investigation has shown that it is crucial to select diffusion parameters that closely match the characteristics of the rock, even when fixed kinematic constraints are in place. Our cases have demonstrated that changes in the diffusion properties of different rocks have a greater influence on the change of apparent age than variations in grain size. However, further investigation may be necessary to expand the range of grain sizes studied.

Finally, it is interesting to note that our method shows, to our knowledge, for the first time the coupling of fully-consistent geodynamic codes with model results from isotope thermochronology. This method can be easily implemented in any geodynamic model that considers the P-T and time evolution of exhumed markers. In this way, it will be possible to come up with geodynamic scenarios that will have testable consequences.

## 4.5 Acknowledgements

Author thanks Prof. Evangelos Moulas for supervising the ideas of this chapter and giving a support on how to use KADMOS.

## 4.6 References

- Anonymous, 1972. Penrose Field Conference on ophiolites. *Geotimes* 17, 24–25.
- Batt, G.E., Brandon, M.T., 2002. Lateral thinking: 2-D interpretation of thermochronology in convergent orogenic settings. *Low Temp. Thermochronology Tecton. Landsc. Evol.* 349, 185–201. [https://doi.org/10.1016/S0040-1951\(02\)00053-7](https://doi.org/10.1016/S0040-1951(02)00053-7)
- Batt, G.E., Brandon, M.T., Farley, K.A., Roden-Tice, M., 2001. Tectonic synthesis of the Olympic Mountains segment of the Cascadia wedge, using two-dimensional thermal and kinematic modeling of thermochronological ages. *J. Geophys. Res. Solid Earth* 106, 26731–26746. <https://doi.org/10.1029/2001JB000288>
- Brace, W.F., Kohlstedt, D.L., 1980. Limits on lithospheric stress imposed by laboratory experiments. *J. Geophys. Res. Solid Earth* 85, 6248–6252. <https://doi.org/10.1029/JB085iB11p06248>
- Braun, J., Beek, P. van der, Batt, G., 2006. *Quantitative Thermochronology: Numerical Methods for the Interpretation of Thermochronological Data*. Cambridge University Press, Cambridge. <https://doi.org/10.1017/CBO9780511616433>
- Cloos, M., 1993. Lithospheric buoyancy and collisional orogenesis: Subduction of oceanic plateaus, continental margins, island arcs, spreading ridges, and seamounts. *GSA Bull.* 105, 715–737. [https://doi.org/10.1130/0016-7606\(1993\)105<0715:LBACOS>2.3.CO;2](https://doi.org/10.1130/0016-7606(1993)105<0715:LBACOS>2.3.CO;2)
- Condie, K.C., Stern, R.J., 2023. Ophiolites: Identification and tectonic significance in space and time. *Geosci. Front.* 14, 101680. <https://doi.org/10.1016/j.gsf.2023.101680>
- Dewey, J.F., 1976. Ophiolite obduction. *Tectonophysics* 31, 93–120. [https://doi.org/10.1016/0040-1951\(76\)90169-4](https://doi.org/10.1016/0040-1951(76)90169-4)
- Dilek, Y., Furnes, H., 2014. Ophiolites and Their Origins. *Elements* 10, 93–100. <https://doi.org/10.2113/gselements.10.2.93>
- Dodson, M.H., 1973. Closure temperature in cooling geochronological and petrological systems. *Contrib. Mineral. Petrol.* 40, 259–274. <https://doi.org/10.1007/BF00373790>
- Grove, M., Harrison, T.M., 1996.  $^{40}\text{Ar}^*$  diffusion in Fe-rich biotite. *Am. Mineral.* 81, 940–951. <https://doi.org/10.2138/am-1996-7-816>

- Harrison, T.M., 1982. Diffusion of  $^{40}\text{Ar}$  in hornblende. *Contrib. Mineral. Petrol.* 78, 324–331. <https://doi.org/10.1007/BF00398927>
- Harrison, T.M., C  lerier, J., Aikman, A.B., Hermann, J., Heizler, M.T., 2009. Diffusion of  $^{40}\text{Ar}$  in muscovite. *Geochim. Cosmochim. Acta* 73, 1039–1051. <https://doi.org/10.1016/j.gca.2008.09.038>
- Ibragimov, I., Moulas, E., 2023. Role of continental-margin architecture on models of ophiolite emplacement. *J. Geol. Soc.* jgs2023-063. <https://doi.org/10.1144/jgs2023-063>
- Kiss, D., Podladchikov, Y., Duretz, T., Schmalholz, S.M., 2019. Spontaneous generation of ductile shear zones by thermal softening: Localization criterion, 1D to 3D modelling and application to the lithosphere. *Earth Planet. Sci. Lett.* 519, 284–296. <https://doi.org/10.1016/j.epsl.2019.05.026>
- Lister, G.S., Baldwin, S.L., 1996. Modelling the effect of arbitrary P-T-t histories on argon diffusion in minerals using the MacArgon program for the Apple Macintosh. *Tectonophysics* 253, 83–109. [https://doi.org/10.1016/0040-1951\(95\)00059-3](https://doi.org/10.1016/0040-1951(95)00059-3)
- McDougall, I., Harrison, T.M., 1999. *Geochronology and Thermochronology by the  $^{40}\text{Ar}/^{39}\text{Ar}$  Method*, 2nd ed. Oxford University Press.
- Moores, E.M., 1982. Origin and emplacement of ophiolites. *Rev. Geophys.* 20, 735–760. <https://doi.org/10.1029/RG020i004p00735>
- Moulas, E., Brandon, M.T., 2022. KADMOS: a Finite Element code for the calculation of apparent K-Ar ages in minerals. Zenodo. <https://doi.org/10.5281/zenodo.7358136>
- Rassios, A.E., Dilek, Y., 2009. Rotational deformation in the Jurassic Mesohellenic ophiolites, Greece, and its tectonic significance. *Lithos* 108, 207–223. <https://doi.org/10.1016/j.lithos.2008.09.005>
- Reiners, P.W., Brandon, M.T., 2006. Using thermochronology to understand orogenic erosion. *Annu. Rev. Earth Planet. Sci.* 34, 419–466. <https://doi.org/10.1146/annurev.earth.34.031405.125202>
- Schmalholz, S.M., Duretz, T., 2015. Shear zone and nappe formation by thermal softening, related stress and temperature evolution, and application to the Alps. *J. Metamorph. Geol.* 33, 887–908. <https://doi.org/10.1111/jmg.12137>
- Tsenn, M.C., Carter, N.L., 1987. Upper limits of power law creep of rocks. *Tectonophysics* 136, 1–26. [https://doi.org/10.1016/0040-1951\(87\)90332-5](https://doi.org/10.1016/0040-1951(87)90332-5)
- Wakabayashi, J., Dilek, Y., 2003. What constitutes ‘emplacement’ of an ophiolite?: Mechanisms and relationship to subduction initiation and formation of metamorphic soles. *Geol. Soc. Lond. Spec. Publ.* 218, 427–447. <https://doi.org/10.1144/GSL.SP.2003.218.01.22>

Wheeler, J., 1996. Diffarg: A program for simulating argon diffusion profiles in minerals. *Comput. Geosci.* 22, 919–929. [https://doi.org/10.1016/S0098-3004\(96\)00061-1](https://doi.org/10.1016/S0098-3004(96)00061-1)



---

## Chapter 5

# Summary & Conclusion

### 5.1 Summary

The main results of this thesis are summarized in this chapter. The main goals of this thesis were to understand the crucial factors that were involved in the obduction of small oceanic basins atop continental regions. This was largely investigated in chapter 2. In chapter 3 a high-resolution 1-d mathematical model was developed for the physical conditions, particularly temperature, that prevail in the main thrust zone during ophiolite obduction. Finally, chapter 4 links the dynamics of ophiolite obduction to the apparent  $^{40}\text{K}$ - $^{40}\text{Ar}$  (and  $^{40}\text{Ar}$ - $^{39}\text{Ar}$ ) ages obtained in orogenic regions. More detailed summaries of each chapter are provided below.

#### **Chapter 2: The role of continental-margin architecture on models of ophiolite emplacement.**

Chapter 2 covers the process of ophiolite emplacement resulting from compressional movement during the closing Neotethys ocean after the initiation of intra-oceanic subduction. The location at the hinge suggests that the ocean basin would be relatively small, and transform faulting may occur due to the oblique relative closing movement to the spreading axis.

A 2-D numerical thermomechanical model is employed to demonstrate the obduction of ophiolites under continuous compression of a relatively small ocean basin between two continental margins. The model includes realistic buoyancy forces as the density field is dependent on the phase equilibrium diagram. The systematic investigation confirmed that ophiolites from small oceanic basins must be young and hot to be overthrust onto the continental margin while adhering to other constraints, such as convergence velocity. Additionally, for the obduction process to initiate correctly, it is necessary to consider the asymmetric structure of the oceanic plate in the position of the initial breaking. This corresponds to the existence of transform faults near the mid-ocean ridge, as it was already suggested by previous studies. The analysis of P-T paths for the markers associated with metamorphic rocks indicates that they

reached amphibolite facies conditions during obduction. These conditions can be correlated with those observed in some natural ophiolites, such as the Pindos and Mirdita ophiolites.

### **Chapter 3: A thermo-mechanical model of the thermal evolution and incorporation of the metamorphic sole in the Oman ophiolite.**

In Chapter 3, we utilized a 1-D thermomechanical model to investigate shear heating during the emplacement of a young and hot oceanic plate over relatively colder oceanic crustal rock, which is expected during the ophiolite obduction process described in Chapter 2. The initial temperature distribution is characterized by a specific sawtooth shape, as the overthrusting oceanic plate remains hot during the initial stages of stacking. The initial point for the shear zone is naturally the point with the highest temperature at the bottom of the upper plate. This is related to the lower viscosity, and higher temperature, that this point has. With continuing heating of the footwall, the shear zone migrates to the upper part of the lower plate. This process can explain the migration of the thermally-softened zone and the incorporation of metamorphosed crustal rocks (metamorphic sole) into the ophiolitic complex. For this study, we chose a strong crustal rheology to achieve the apparent metamorphic gradients reported in Oman ophiolites while maintaining a relatively low convergence velocity as a constraint. The high-stress limit of this rheology has been modified using a hyperbolic-sine flow law that approximates exponential creep at high stresses. The cooling rates obtained in the model after the shearing phase for the first time correspond to the measured cooling rates in Oman. After interpretation of the systematic investigation, an analytical approximation revealed an almost linear relationship between the expected temperature in the shear zone and the convergence velocity.

### **Chapter 4: Geochronological constraints of ophiolites.**

In chapter 4, we conducted thermochronological calculations for rocks that ended up on the surface of one of the 2-D models presented in chapter 2. For this study, we used a model that included erosion and variable convergence velocity. The velocity slowed down towards the end of the simulation as it is expected during continental collision/subduction. The variation of apparent ages on the surface is a result of uneven erosion, dictated by the complex trajectory during the emplacement process. The uneven erosion, combined with the differential exhumation due to localized plastic deformation, leads to the formation of apparent-isotopic-age gradients in the exhumed rocks. Our results may not directly confirm the influence of dissipative heating, but we definitely observe that rocks from a deeper part of the lithosphere are carried up along shear zones. Since the rocks within such shear zones come from deeper crustal levels, their isotopic clocks are partially reset during their high-temperature stage. Our

systematic study demonstrated the influence of grain size and rock type on the apparent age estimate and showed that different rock selection can change the estimate by more than 1 Myrs. The methods presented in this chapter enable the integration of isotope geochronology findings with geodynamic codes that are fully consistent. This approach is suitable for validating geodynamic models as both methods typically focus on studying orogenic zones.

## 5.2 Conclusion

This work aims to address the challenges posed by the ophiolite emplacement process. We confirm the obduction mechanics proposed in previous works, which had not been validated with fully consistent numerical models before. Our suggestions on timescales, rates of obduction, mechanisms of incorporation of metamorphic sole, and cooling rates closely match observations in nature. By utilizing a variety of numerical methods, ranging from 2D thermomechanical models to geochronological age calculations, we have incorporated currently known information on ophiolites as constraints to provide a vision of the ophiolite emplacement process using all current knowledge and achievements in geology and computational geosciences. Although most of the data was validated for Tethyan-type ophiolites, it can still provide insight into ophiolite evolution.

# Eidesstattliche Erklärung

Ich versichere hiermit gemäß §10 Abs. 3d der Promotionsordnung des Fachbereichs 09 (Chemie, Pharmazie und Geowissenschaften) der Johannes Gutenberg-Universität Mainz vom 24.07.2007, die als Dissertation vorgelegte Arbeit selbständig und nur unter Verwendung der in der Arbeit angegebenen Hilfsmittel verfasst zu haben. Ich habe oder hatte die hier als Dissertation vorgelegte Arbeit nicht als Prüfungsarbeit für eine staatliche oder andere wissenschaftliche Prüfung eingereicht. Ich hatte weder die jetzt als Dissertation vorgelegte Arbeit noch Teile davon bei einer anderen Fakultät bzw. einem anderen Fachbereich als Dissertation eingereicht.

---

Iskander Ibragimov

Mainz, 2024

## Curriculum Vitae

Name	Iskander Ibragimov
Birth date	6 Jan 1995
Birth place	Al'metevsk, Tatarstan, Russia
Marital status	no
2002-2013	School/ High School in Lyceum No.2, Almetevsk, Russia
2013-2017	Bachelor in Geology, Institute of Geology and Fossil fuels, Kazan Federal University, Kazan, Russia
2017-2019	Master in Petroleum Engineering, Skolkovo Institute of Science and Technology, Moscow, Russia
2020-2024	Doctoral Thesis, Geosciences, Johannes Gutenberg University, Mainz, Germany